Design of an Intensified Reactor for the Synthetic Natural Gas Production through Methanation in the Carbon Capture and Utilization Context

Santiago Ortiz Laverde
Chemical Engineer

Submitted in the fulfilment of the requirements for the degree of Master in Process Design and Management

Advisor:
Manuel Alfredo Figueredo Medina, M.Sc.

Co-advisors:
Camilo Rengifo Gutiérrez, Ph.D.
Martha Isabel Cobo Ángel, Ph.D.

Universidad de
La Sabana

Maestría en Diseño y Gestión de Procesos
Faculty of Engineering
Universidad de La Sabana
Chía, Colombia
2020

DEDICATION

To my parents and brother,
to whom I owe everything in my life.

ACKNOWLEDGMENTS

First of all, I am grateful to Universidad de La Sabana, an institution that has immensely funded my education as a professional, magister, and human being.

Further, many people have contributed to my formation in these past two years. Nevertheless, some of them are worth mentioning here.

I would first like to acknowledge my advisor, Professor Manuel Figueredo, mostly because he has always believed in me from the beginning and despite all the obstacles along the way. Second to Professor Camilo Rengifo, not only because of his lectures in applied mathematics but also because he has motivated me until the end. Third, to Professor Martha Cobo, for encouraging my involvement in this project and whom I am simply honoured to have as co-advisor. Fourth, to Professors William Oquendo and Mario Noriega, who have set a precedent in my academic formation and whom I deeply admire. Fifth, to Dr Néstor Sánchez, whose true friendship has accompanied me during this journey.

Finally, I want to thank Universidad Nacional de Colombia for opening its doors to me in the master's program, showing me the genuine rigour required to be qualified as a chemical engineer.

ABSTRACT

The idea of a sustainable future has led to the exclusion of fossil fuels from development policies and the inclusion of low-carbon alternatives instead. The strategy must be holistic, as proposed by the carbon capture and utilization technologies alongside renewable energies. An example is converting CO_2 into value-added products, such as CH_4 or Synthetic Natural Gas (SNG), using surplus power of renewable alternatives, in a low-carbon footprint process. The chemical route for the synthesis of SNG from CO_2 and H_2 is a catalytic reaction known as CO_2 methanation or Sabatier reaction.

The methanation is an example of CO_2 capture and utilization technologies' industrial application within the so-called Power-to-Methane (PtM) context. In this scenario, fixed bed reactors have been the reaction technology employed by default. However, their deficiency in handling the heat released from the highly exothermic Sabatier reaction or responding to the process' intermittency appropriately has been demonstrated. These drawbacks have aroused scientific interest in developing reactors better adapted to the PtM context demands. One approach is by intensifying the methanation process to increase the mass- and energy-transfer and improve its transient response.

In this project, the phenomenological hot spots formation in fixed bed reactors used for the methanation industrial process was investigated through a parametric sensitivity analysis, simulating the reactor start-up. On the other hand, it was proposed a CFD simulation-aided conceptual design of a wall-coated reactor for the SNG production using an intensification strategy. The design was based on a reactor formed by single-pass and heat-exchanger stacked-plates. The reacting channel dimensions were defined, including the catalytic layer thickness, fulfilling a minimum quality threshold given by the CO_2 conversion ($\geq 95\%$). The proposed design was also intended to maximize the volume of processed gas while meeting the quality requirement, resulting in a throughput per reaction channel of ~12 ml/min. Likewise, the plates manifold geometry and dimensions that best promoted a flow rate uniform distribution were established as a function of the number of reacting channels. Finally, a preliminary dynamic analysis of the operation start-up and shutdown was performed, establishing that the designed reactor does not present a hysteresis behaviour, an ideal condition for intermittent environments.

Keywords: Carbon Capture and Utilization, CFD-aided Design, Fixed-bed Reactor, Hot spots Formation, Power-to-Methane, Process Intensification.

RESUMEN

La idea de un futuro sostenible ha conllevado a suprimir el uso de combustibles de origen fósil de los planes de desarrollo y por el contrario incluir alternativas con baja huella de carbono. La estrategia debe ser holística, como lo proponen las tecnologías de captura y utilización de CO_2 junto con las energías renovables. Un ejemplo es la conversión del CO_2 en productos con valor agregado, como el CH_4 o Gas Natural Sintético (GNS), utilizando la energía sobrante de las alternativas renovables, en un proceso con baja huella de carbono. La ruta química para síntesis de GNS a partir de CO_2 e H_2 es una reacción catalítica que se conoce como metanación de CO_2 o reacción de Sabatier.

La metanación es un ejemplo de aplicación industrial de las tecnologías de captura y utilización de CO_2 en lo que también se conoce como el contexto *Power-to-Methane* (PtM). En ese ámbito, los reactores de lecho fijo han sido la tecnología de reacción utilizada por defecto. Sin embargo, se ha demostrado su incapacidad para manejar el calor liberado producto de la reacción de Sabatier (altamente exotérmica), o de responder apropiadamente a la intermitencia del proceso. Estas dificultades han despertado el interés científico por desarrollar reactores que se adapten mejor a las exigencias del contexto PtM. Una propuesta yace en intensificar el proceso de metanación, incrementando la transferencia de masa y energía además de mejorar su respuesta transitoria.

En este proyecto se estudió, por un lado, la formación fenomenológica de puntos calientes en reactores de lecho fijo utilizados industrialmente para el proceso de metanación a través de un análisis de sensibilidad paramétrico, simulando el arranque del reactor. Por el otro lado, se propuso un diseño conceptual asistido por simulación CFD de un reactor de pared recubierta para la producción de GNS a través de una estrategia de intensificación. El diseño partió de un reactor formado por platos apilados de intercambio de calor de un solo paso. Se definieron las dimensiones del canal de reacción, incluyendo el grosor de la capa catalítica, que cumplían con el umbral mínimo de calidad dado por la conversión de CO_2 ($\geq 95\%$). El diseño propuesto también tuvo por objeto maximizar el volumen de gas procesado, cumpliendo a la vez con el requisito de calidad, lo que resultó en un rendimiento por canal de reacción de ~12 ml/min. Así mismo se estableció la geometría y dimensiones del colector del plato que mejor favorecían una distribución uniforme de la velocidad del flujo en función del número de canales de reacción. Por último, se realizó un análisis dinámico preliminar del arranque y apagado de la operación, estableciendo que el reactor diseñado no presenta un comportamiento de histéresis, ideal para un entorno con alta intermitencia.

Palabras clave: Captura y Utilización de Carbono, Diseño asistido por CFD, Formación de Puntos calientes, Intensificación de Procesos, Power-to-Methane, Reactor de Lecho Fijo.

CONTENT

List of Figures

List of Tables

DOCUMENT STRUCTURE

This document is divided in three chapters:

Chapter 1 provides a synopsis of the project and the studied subject. This section presents a general overview and a short theoretical framework of the finite element method addressing a case study in the nuclear engineering field as a proof-of-concept. The 1st Chapter is also expected to guide the reader in justifying the work, the main objectives, and the project scope.

Chapter 2 discusses the hot-spot formation typical of fixed-bed reactors employed in the CO_2 methanation process. The results are supported on several parametric sensitivity analysis under relevant industrial operating conditions. Nevertheless, this discussion is not presented as the main topic of Chapter 2 but as a case study forming part of a wider investigation. The 2nd Chapter is entitled "*Proposal of an open-source computational toolbox for solving PDEs in the context of chemical reaction engineering using FEniCS and complementary components*" and describes a novel open-source computational toolbox, demonstrating its feasibility in the chemical engineering field through two case studies. The first is introduced as a validation case and addresses the well-known selective oxidation of o-xylene to phthalic anhydride. The second case deals with the CO_2 methanation in the Power-to-Methane (PtM) context, serving as an example of the toolbox applicability within a state-of-the-art research topic. In both, the results are discussed and contrasted with another reliable software or the reported in prior research, concluding consistency across them.

Chapter 3 provides a Computational Fluid Dynamics (CFD) simulation-aided design for an intensified methanation device. The design is evaluated under relevant operating conditions in PtM applications, intending to avoid the formation of hot spots and the existence of mass- and heat-transfer resistances. The reactor structural evaluation covers a wide range from the micrometric to the millimetre scale and involves the individual wall-coated reaction channel as well as the stacked plate design. In the last one, the geometry that better favours a uniform distribution of the flow is analysed, critical for an eventual scale-up of the intensified process. Finally, the proposed layout is subjected to an on/off disturbance characteristic of power-to-gas industrial conditions. This Chapter is titled "*CFD-aided conceptual design of an intensified reactor for the production of synthetic natural gas within the power-to-methane context*". To the best of the authors' knowledge, a computer-aided design of this kind has not been considered so far as a PtM reaction technology.

The results of this manuscript (Chapters 2 and 3) are presented as Papers. The former is already published in the Journal *Heliyon*, section *Heliyon Engineering*. Journal classified as Scopus Q2. The latter is about to be submitted to a high-impact Q1 journal. References, nomenclature and abbreviations are given at the end of each Chapter. The project's overall conclusions and corresponding appendixes are presented at the end of the manuscript.

RESEARCH CONTRIBUTIONS AND DISTINCTIONS

The development of this project has led to some contributions to the scientific community. These inputs are listed below, along with a couple of recognitions worthy of mention.

Papers

- Santiago Ortiz-Laverde, Camilo Rengifo, Martha Cobo, Manuel Figueredo⸸. "CFD-Aided Design of an Intensified Reactor for the Production of Synthetic Natural Gas within the Power-to-Methane Context". Scientific paper in final preparation.
- Santiago Ortiz-Laverde, Camilo Rengifo, Martha Cobo, Manuel Figueredo⸸. "Proposal of an open-source computational toolbox for solving PDEs in the context of chemical reaction engineering using FEniCS and complementary components". Published in Heliyon, section Heliyon Engineering. Journal classified as Scopus Q2.
- Santiago Ortiz, Camilo Rengifo, Martha Cobo, Manuel Figueredo⸸. "Packed-bed and Microchannel Reactors for the Reactive Capture of CO2 within Power-to-Methane (P2M) Context: A Comparison". Published in Computer Aided Chemical Engineering. September 2020. Book Series classified as Scopus Q3.

Participation in academic events

- Santiago Ortiz, Camilo Rengifo, Martha Cobo, Manuel Figueredo⸸. "Modelling and simulation of a fixed–bed reactor for CO2 capture through methanation". Poster. Segundo encuentro "Alianza para la Sostenibilidad Energética de Colombia" – SÉNECA. Mayo 7 y 8, 2020. Encuentro virtual.
- Santiago Ortiz, Camilo Rengifo, Martha Cobo, Manuel Figueredo⸸. "Packed-bed and Microchannel Reactors for the Reactive Capture of CO2 within Power-to-Methane (P2M) Context: A Comparison". Poster. ESCAPE30 - The 30th European Symposium on Computer Aided Process Engineering. Milano, September 3, 2020. Virtual meeting.

Distinctions

- Recognition for best poster in nation-wide scientific meeting. Segundo encuentro "Alianza para la Sostenibilidad Energética de Colombia" – SÉNECA. Mayo 7 y 8, 2020. Encuentro virtual.
- Scholarship to pursue the Master in Process Design and Management. Universidad de La Sabana. Chía, Colombia (2018 – 2020).

CHAPTER 1: Overview

The purpose of this chapter is to introduce the Project's main topic as a way of justification and to present some relevant mathematical concepts about the finite element method as the backbone of the computational methodology employed throughout the manuscript. The last goal is attained by solving an interdisciplinary engineering problem that serves as a proof-of-concept.

1.1 Introduction and State of the Art

Economic growth detached from the concept of sustainable development has brought severe consequences. Due to the Emission of Greenhouse Gases (GHGE), the global warming phenomenon is a clear environmental example. The latter has proven the non-sustainability of the economic model based on fossil fuels [1], [2].

Accordingly, different actions have been taken to deal with global warming. In 1992, the United Nations Framework Convention on Climate Change (UNFCCC) was created as an international treaty to combat climate change in a cooperative way. By 1997 the UNFCCC was extended through the Kyoto Protocol in which some emission reduction targets and two commitment periods were established (2008-2012 & 2013-2020). Besides, the so-called Conferences of the Parties have served as yearly plenaries of the UNFCCC to assess progress in dealing with climate change. In 2015, it took place at Paris the Conference of the Parties (COP21), resulting in the Paris Agreement. This resolution has sought to accelerate and intensify the actions, and investment lacked for a sustainable low carbon future, as long as to deal with the on-going repercussions of global warming [3].

As a result, lower carbon-footprint technologies have started to make their way into the industrial sector as the foremost approach of new economic models for future societies. Fossil-based conventional energy sources are currently being replaced by renewable ones such as wind, photovoltaic, hydroelectric, and geothermal power. However, one of the main obstacles encountered by these technologies within the energy market is their inability to provide a baseload electric power. This intermittent nature has limited their integration with the power grid. Despite those difficulties, penetration of renewable sources is expected to expand further, and storage strategies to save energy during low-demand/high-supply periods have become crucial [4]–[7].

An emerging storage strategy that has gained traction is the storage of surplus renewable energy in the form of chemical fuels [8]. The logical pathway is converting electrical power into hydrogen (H_2) by water (H_2O) electrolysis through the so-called power-to-hydrogen (P2H) approach. Renewable hydrogen can be used as a zero-emission fuel or as a feedstock in various chemical processes. However, the available infrastructure concerning hydrogen transport and storage is scarce and expensive to acquire, restraining the P2H concept. Instead, hydrogen can be transformed into valuable products with broader applications [5].

The above has brought opportunity gaps to novel carbon-efficient alternatives using H_2 of renewable origin as an energetic precursor. The leading example is the Carbon Sequestration and Utilization (CSU) technologies, by which the carbon dioxide (CO_2) is captured and transformed into value-added products in the so-called power-to-X context [9]. In that sense, H_2 can be transformed into chemical fuels with wider supply chains, such as methane (CH_4), using the

extensive Natural Gas (NG) grid, plus contributing to the reduction of GHGE through the consumption of CO_2 from contaminant emissions. Besides, NG, in which CH_4 is often the largest component (up to 80 vol%), is one of the cleanest hydrocarbon fuels, showing good efficiency in internal-combustion engines [10], [11], and the third current energy source of global consumption with 24% of participation worldwide below petroleum (33%) and carbon (28%) [12], [13].

The chemical pathway proposed to synthesize CH_4 from H_2 and CO_2, namely Synthetic Natural Gas (SNG) in the power-to-methane (P2M) context, is a catalytic process known as methanation (or Sabatier reaction) [14], [15]. This reaction is distinguished by its highly exothermic nature, making heat removal from the reactor a mandatory task. Otherwise, leading to catalytic deactivation paths or the shift of thermodynamic equilibrium originated at elevated temperatures [8], [16].

Fixed-bed reactors have been the most employed reaction technologies for the Sabatier process in P2M applications. However, they have proven to be incapable of allowing appropriate temperature management, to the extent of avoiding the formation of hot spots, under undiluted conditions [17], [18]. As a result, several other reactors have been adapted for the CO_2 methanation regardless of the implemented catalyst. Some of them are fluidized-bed, monolith, foam, microchannel, membrane, sorption enhanced, slurry, and non-thermal plasma. These reactors are still in the development stage and have been studied as a function of several parameters to select the most suitable technology [17]–[26].

In terms of heat removal and temperature management, microchannel reactors have proven to be superior. Microreaction technologies are part of the Process Intensification (PI) paradigm that has gained significance in the last two decades [27]–[29]. This strategy consists of the miniaturization of operating units and ultimately of the entire plant. The PI implies the miniaturization of at least one of the equipment dimensions, which translates into augmented surface/volume ratio and small diffusion paths [30]. Accordingly, the mass- and heat-transfer coefficients are several times larger than conventional equipment, whereas the resistances of transport phenomena become negligible. Moreover, other benefits are also highlighted about PI; fast response times, higher catalyst performance, fewer operation costs (energy expenditure, reagent consumption), environmentally friendly and process safety are some of them [27], [30].

Therefore, PI is an approach worth applying in the P2M context. Typical features of intensified reactors are promising to overcome technical challenges encountered by conventional reactors such as fixed-bed Sabatier reactors. The primary enhancements entail an increased production efficiency due to lower mass transport resistances, the mitigation of hot spots at average conditions extending the operating limits, and improved flexibility to deal with intermittency due to faster response times. Nonetheless, a lack of PI applications has been reported for P2M and solely on the

micrometric scale [22], [31]. The PI concept can be employed to decouple SNG production at high CO_2 conversion rates (>95%) and under undiluted conditions from a runaway behaviour and the consequences derived from it.

This research project was aimed first to comprehend the formation of hot spots in fixed bed reactors within an industrial scenario of the P2M context. This target was accomplished via investigating different operating windows of typical conditions in a parametric sensitivity fashion. This topic was covered in Chapter 2 and presented as a case study of a scientific paper. Furthermore, once the major pitfall of fixed-bed reactors in P2M applications related to thermal management was addressed, a conceptual design of an intensified reactor was proposed and evaluated under relevant industrial conditions. This design involved the simulation of reacting flows as a function of several structural parameters. Hence, the question of "up to what degree of miniaturization should the intensification be conducted (?)" was addressed in compliance with process productivity and SNG quality. The latter was likewise presented as a scientific paper and constitutes Chapter 3 of the manuscript.

In the project's development, no experiments were conducted; instead, the study was entirely computer-aided. The objectives were met through the solution of phenomenological models describing well-known conservation laws and expressed by sets of partial differential equations (PDEs) for space- and time-dependent problems. Therefore, a numerical approximation was required owing to the mathematical complexity of the systems. Accordingly, the Finite Element Method (FEM) was adopted through both open-source and commercial software. The open-source computational platform named FEniCS plus distinct Python modules were employed in Chapter 2, whereas the software COMSOL Multiphysics® was used in Chapter 3 to meet the research goals and perform the corresponding modelling and simulation tasks. It was deemed that the best way to provide a conceptual framework for the numerical-computational approach was through a case study that could serve as a proof-of-concept, as presented in the following section.

1.2 Baseline Theoretical Framework

The case study consists of a system widely investigated in the nuclear engineering field, but which ultimately leads to a mathematical and phenomenological problem commonly employed interdisciplinarity. In broad terms, the power produced in a nuclear reactor has its origin from a nuclear fuel, where water vapor is used as an intermediary within the thermoelectric power generation cycle. This process often occurs in a Pressurized Water Reactor (PWR), where the reactor vessels are formed by a fuel rod covered by the so-called cladding rod [32]. The former is generally made of uranium dioxide (UO_2), constituting the source of nuclear energy. The latter is usually made of a corrosion-resistant zirconium alloy, whose primary function is to prevent radioactive material leakage resulting from nuclear fission. The nomenclature used in Chapter 1 is listed at the end of the Chapter for ease of reading (refer to Section 1.3).

The case study layout, including power generation value and geometric data, were taken from [33]. The task was to reproduce the heat transport phenomena along the solid body (fuel and cladding rods), given some geometrical parameters, transport properties (i.e., conductivity), and a constant volumetric heat generation value. The problem is, therefore, to solve the general heat transport equation by conduction, defined as:

$$\rho C_p \frac{\partial T}{\partial t} = \nabla \cdot (k \nabla T) + f \, . \tag{1.1}$$

Eq. (1.1) is a conservative governing equation derived from Fourier's law that describes the temperature field's distribution along a given body over time. Herein f accounts for a source term or, in this case, the volumetric power generation caused by nuclear fission (q_v, W/m^3). The problem is solved in steady-state and without considering axial variations along the fuel and cladding rods for simplicity. Therefore, after neglecting the axial coordinate, the domain is limited to a circular area, as shown in Figure 1-1.

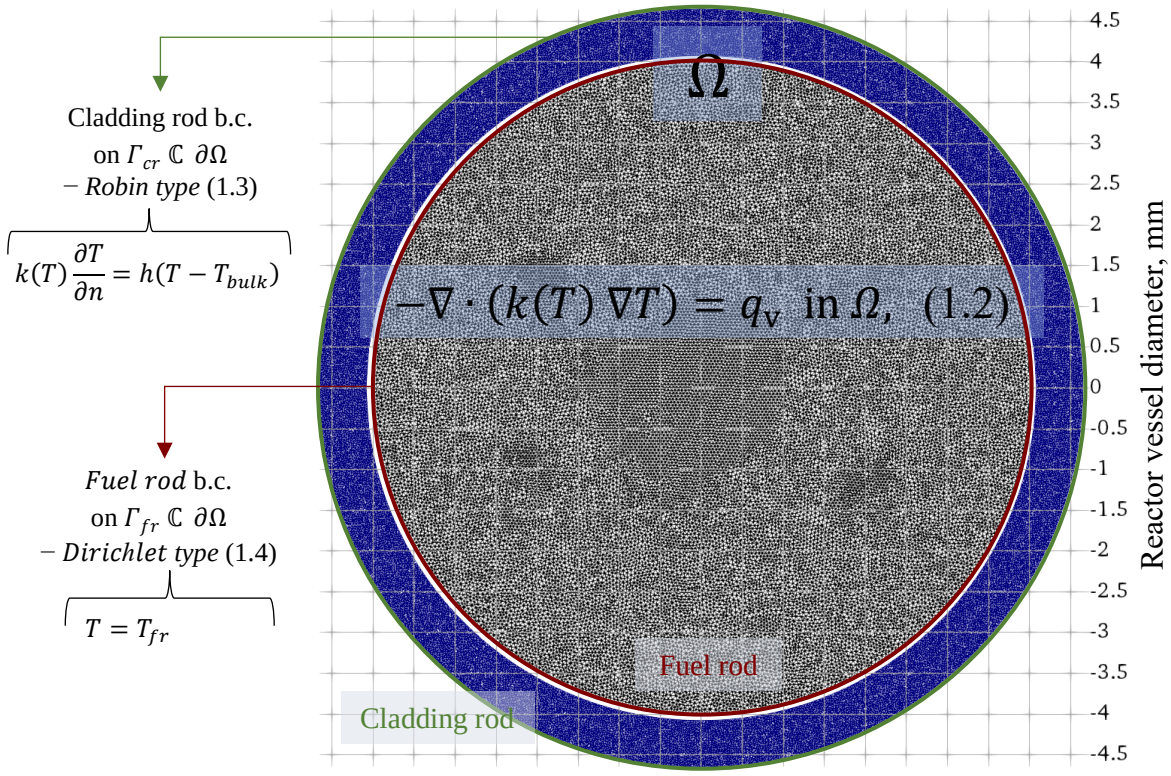

Figure 1-1. Mathematical scheme of reactor vessel (fuel and cladding rods).

Note that the Eqs. (1.2)-(1.4) are displayed schematically in Figure 1-1. Eq. (1.2) accounts for the heat-transfer PDE to be solved over the domain Ω, whereas Eqs. (1.3)-(1.4) describe the boundary conditions (b.c.) for the cladding and fuel rods, respectively.

1.2.1 Numerical approach

The numerical method applied to solve any of the emerging phenomenological models throughout the document was the finite element method. The following explanation grants a brief description of this method through its application to the aforementioned case study. More comprehensive reviews on the FEM can be found elsewhere [34]–[36].

The elementary principle lies in the approximation of the function T, as the dependent variable in Eq. (1.2), by a linear combination of known so-called basis or trial functions, according to the following expression:

$$T \cong T_h = \sum_{j=1}^{N} T_j \phi_j \, . \tag{1.5}$$

Herein, ϕ_j denotes the trial functions, T_j the coefficients of the linear combination of trial functions, and T_h the approximation of T. Thus, the issue is to find the coefficients that yield the best estimate of T.

Notwithstanding, before applying Eq. (1.5) to approximate the function T by finite elements, the mathematical set must be rewritten as a variational problem (also known as the weak formulation). To formulate the variational problem, each PDE is multiplied by a so-called test function v and integrated over its particular domain. The weak formulation for Eq. (1.2) can be derived as follows:

$$\int_{\Omega} v \left[-\nabla \cdot (k(T)\, \nabla T) - q_{\mathrm{v}} \right] dx = 0 \tag{1.6}$$

$$-\int_{\Omega} v \left[\nabla \cdot (k(T)\, \nabla T) \right] dx = \int_{\Omega} (k(T) \nabla T \cdot \nabla v)\, dx - \int_{\partial\Omega} \left(k(T) \frac{\partial T}{\partial n} \cdot v \right) ds \, , \tag{1.7}$$

$$\int_{\Omega} (k(T) \nabla T \cdot \nabla v)\, dx - \int_{\partial\Omega} \left(k(T) \frac{\partial T}{\partial n}\, v \right) ds - \int_{\Omega} (q_{\mathrm{v}}\, v)\, dx = 0 \, , \tag{1.8}$$

$$\mathrm{F}(T, v) = -\int_{\Omega} (k(T) \nabla T \cdot \nabla v)\, dx + \int_{\Omega} (q_{\mathrm{v}}\, v)\, dx + \int_{\partial\Omega} \left(k(T) \frac{\partial T}{\partial n}\, v \right) ds = 0 \, . \tag{1.9}$$

All the second-order terms are integrated by parts as expressed in Eq. (1.7). Recall from Figure 1-1 that the heat equation is tied to a Robin-type boundary condition (b.c.) at the outer boundary (cladding rod) and a Dirichlet-type at the edge of the fuel rod. Note that only the Robin-type is incorporated in the path-integral, whereas the Dirichlet b.c. vanishes.

The major reason for the variational formulation to be derived is its lesser requirements relative to the original PDE (i.e., no 2nd-order derivatives are involved). Thus, the set of equations is said to be relaxed or weakened in an integral sense, yet the problem's mathematical definition is still

exact. After turning the original PDE into a variational problem, the discretization can proceed using the *Galerkin method* as one of the various FEM formulations. The latter implies that test and trial functions (v and ϕ_j) belong to the same function space (i.e., the *Hilbert* space H), which is often expressed in the following fashion,

$$\{\phi_j\}_{j=1}^{N} \text{ for } T_h \in H(\Omega) \quad and \quad \{\hat{\phi}_i\}_{i=1}^{N} \text{for } v \in H(\Omega)\,. \tag{1.10}$$

Inserting Eqs. (1.5) and (1.10) into the weak formulation given by Eq. (1.9) yields a discrete form of the original PDE, as shown below,

$$\mathrm{F}(T_h, v) = -\int_{\Omega} (k\,\nabla T_h \cdot \nabla v)\,dx + \int_{\Omega} (q_{\mathrm{v}}\,v)\,dx + \int_{\partial\Omega} \left(k\frac{\partial T_h}{\partial n}\,v\right) ds = 0\,, \tag{1.11}$$

$$\mathrm{F}(T_h, v) = \sum_{j=1}^{N} T_j \int_{\Omega} -\left(k\,\nabla\phi_j \cdot \nabla\hat{\phi}_i\right) dx + \int_{\Omega} \left(q_{\mathrm{v}}\,\hat{\phi}_i\right) dx + \int_{\partial\Omega} \left(k\frac{\partial\phi_j}{\partial n}\,\hat{\phi}_i\right) ds = 0\,. \tag{1.12}$$

Accordingly, Eq. (1.12) is applied to every finite element over the discretized domain Ω giving place to a square system of equations. Herein, the vector of unknowns comprises the coefficients T_j that accompany the discrete trial-space's basis functions that approximate T. The mathematical set resulting from the discrete variational formulations is then rearranged in a matrix fashion to be assembled before computation. The solution strategy depends on whether the system is linear or not. For instance, a *Gauss-Seidel* based-solver may be employed for linear problems, whereas *Newton* method will work for the opposite. In this case, since conductivity is a temperature-dependent variable, it constitutes a nonlinear problem.

1.2.2 Computational implementation

The mathematical scheme shown in Figure 1-1 was solved via FEM by employing an open-source computing platform known as FEniCS. With high-level Python and C++ interfaces, the FEniCS Project is a collection of open-source software components directed at the automated solution of PDEs using the finite element method [37]–[40]. The minimum requirement of FEniCS to be able to solve a set of PDEs consists of providing the non-discrete variational form for each equation. Furthermore, the basis and test functions must also be declared, indicating the polynomial family to which these belong, the geometry of the domain, and the type of finite elements discretizing it (mesh resolution).

Accordingly, the expression $\mathrm{F}(T, v)$ from Eq. (1.9) was written as a Python program and solved using FEniCS abstractions. As a data availability statement, the source codes for this case study were uploaded to a public repository on GitHub and can be employed for academic purposes. The link to clone the repository is GitHub/mafigueredom/HeatConduction_PDE. The mesh used to discretize the domain shown in Figure 1-1 was build using the Python packages *pygmsh* and

meshio as detailed later on in Chapter 2 (below). This mesh was made up of 54629 cells (finite elements) with 27567 nodes for the fuel rod region on the one hand, and 45875 cells with 23852 nodes for the cladding rod on the other hand. Moreover, Table 1-1 summarizes the parameters used in the case study with their respective values. The correlations for the temperature-dependent properties in the case of UO_2 (fuel rod) and ZrO_2 (cladding rod) can be found elsewhere [41], [42].

Table 1-1. Summary of parameters

Parameter	Value
Γ_{fr}	4 [mm]
Γ_{cr}	4.65 [mm]
T_{fr}	400 [°C]
T_{bulk}	300 [°C]
h	41 [kW m^{-2} K^{-1}]
q_v	0.5968 [W mm^{-3}]

Figure 1-2 presents the finite-element numerical solution for the temperature distribution over the nuclear reactor vessel. As shown in Figure 1-2, the reactor vessel has a maximum temperature of about 1300 K at the centre of the fuel rod and a minimum of about 580 K at the outer boundary in the cladding rod. The energy-transfer from the core to the water vapor depends on the boundary temperature. Hence the importance of decreasing the temperature gradient through a high conductive across the solid body.

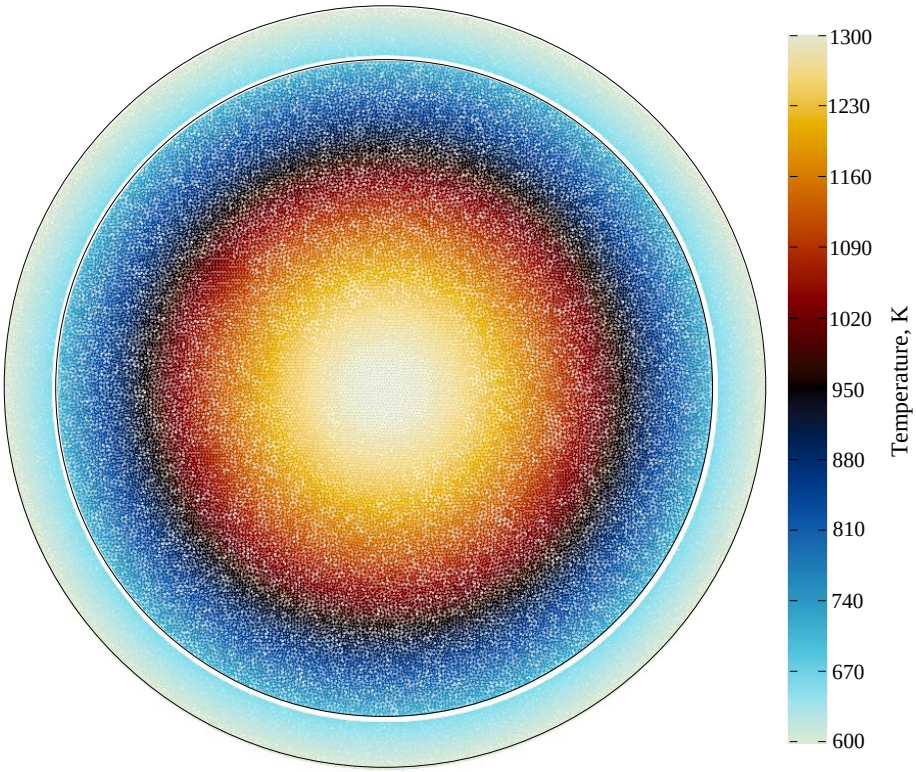

Figure 1-2. Temperature field over the fuel-cladding rod solid body.

1.2.3 Analytical approach

As a reference point for the results obtained numerically, a simplified variant of the problem was stated and solved analytically. The Eq. (1.2) was reduced to an ordinary differential form in cylindrical coordinates, neglecting any angular and axial variation and assuming symmetry at the domain centre point [0, 0]. The streamlined problem, its boundary conditions and analytical solution are given in Table 1-2. Two Ordinary Differential Equations (ODEs) expressed by Eqs. (1.13)-(1.14) were formulated for the fuel and cladding rod, respectively.

Table 1-2. Summary of the mathematical scheme for the analytical approach.

Description	Fuel rod		Cladding rod	
Differential form	$\frac{1}{r}\frac{d}{dr}\left(r\frac{dT}{dr}\right)+\frac{q_v}{k}=0$	(1.13)	$\frac{1}{r}\frac{d}{dr}\left(k\,r\frac{dT}{dr}\right)=0$	(1.14)
Boundary conditions	$\frac{dT}{dr}=0\Big\vert_{r=0}$, $T(r)=T_{fr}\vert_{\Gamma_{fr}}$	(1.15)	$T(r)=T_{fr}\vert_{\Gamma_{fr}}$, $-k\frac{\partial T}{\partial r}=h(T(r)-T_{bulk})\Big\vert_{\Gamma_{cr}}$	(1.16)
Analytical solution	$T(r)=\frac{q_v}{4\,k}\left({\Gamma_{fr}}^2-r^2\right)+T_{fr}$	(1.17)	$T(r)=\frac{T_{bulk}-T_{fr}}{\ln\left(\Gamma_{cr}/\Gamma_{fr}\right)}\ln\left(\frac{r}{\Gamma_{cr}}\right)+T_{bulk}$	(1.18)

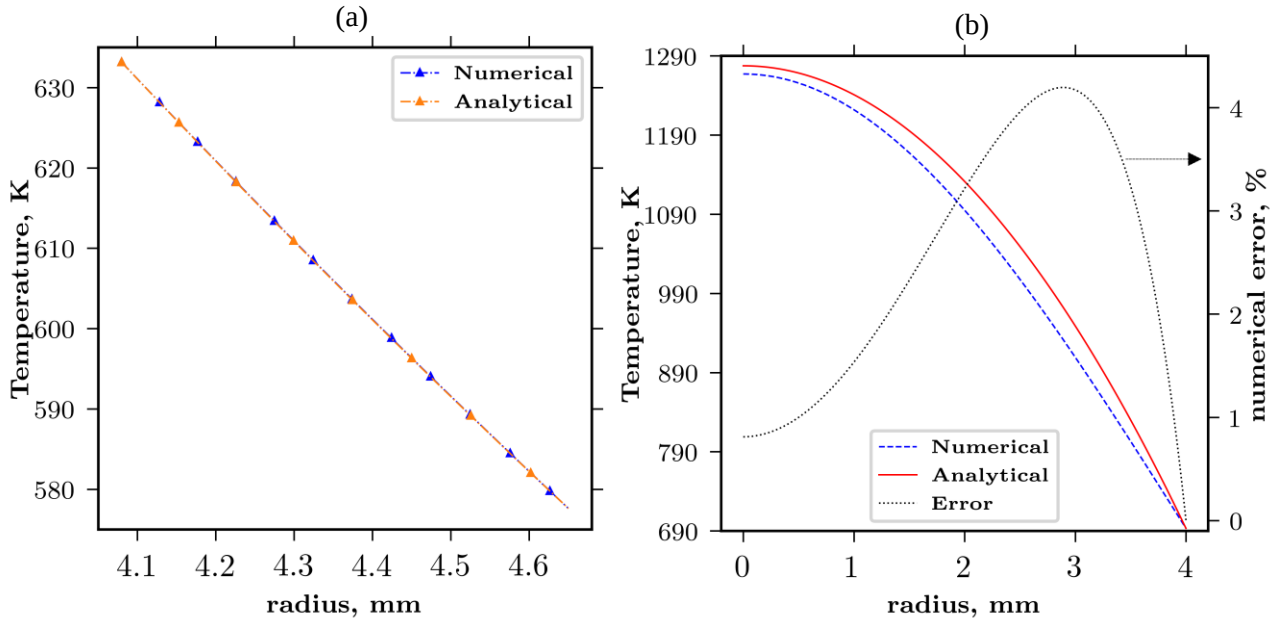

Figure 1-3. Numerical and analytical solutions for the temperature profiles along the cladding rod (a), and fuel rod (b) radius.

As shown in Figure 1-3, the numerical and analytical results are practically equivalent over the cladding rod domain, while the opposite is true for the fuel rod, with an error of up to 4.5 %. This discrepancy arises due to the ODE-based model's relative simplicity, in which the conductivity was assumed to be at an average UO_2 temperature. Although the latter argument equally applies to the cladding rod, the ZrO_2 conductivity (unlike UO_2) is almost temperature-independent in the operating range. Nevertheless, the numerical and analytical approaches are consistent with each other, reinforcing the reliability of the former. Indeed, it could even be argued that the numerical method results are more accurate given the reduced number of assumptions.

1.3 Nomenclature and abbreviations

Greek letters

Ω	Mathematical domain, [−]
$\partial\Omega$	Domain boundaries, [−]
Γ	Mathematical boundary, [−]
ϕ	Basis functions
ρ	Material density, [kg/mm^3]

Latin letters

F	Variational formulation, [−]
v	Test function, [−]
H	Hilbert space
n	Normal vector, [−]
f	Source term, [−]
t	Time, [s]
r	Radial coordinate, [mm]
T	Temperature, [K]
C_p	Specific heat capacity, [J kg^{-1} K^{-1}]
k	Material conductivity, [W mm^{-1} K^{-1}]
h	Convection heat transfer coefficient, [W mm^{-2} K^{-1}]
q_v	Nuclear volumetric power source, [W/mm^3]

Subscripts

i, j	Mesh element, node index
cr	Cladding rod
fr	Fuel rod

Abbreviations

GHGE	Green House Gases Emission
UNFCCC	United Nations Framework Convention on Climate Change
COP21	21st Conferences of the Parties
CSU	Carbon Sequestration and Utilization
NG	Natural Gas
SNG	Synthetic Natural Gas
P2M	Power-to-Methane
PI	Process Intensification
PDEs	Partial Differential Equation(s)
PWR	Pressurized Water Reactor
FEM	Finite Element Method
ODEs	Ordinary Differential Equation(s)

[−] refers to without units.

1.4 Objectives

1.4.1 General objective:

To design an intensified reactor for the Synthetic Natural Gas (SNG) production through methanation, using phenomenological and dynamic models, and considering fixed-bed reactors' performance as a starting point.

1.4.2 Specific objectives:

- To define and solve a phenomenological and start-up model of a fixed-bed reactor for the CO_2 methanation process to study the hotspot formation inside it.
- To propose a computational toolbox for solving advection-diffusion problems in the chemical reactions engineering field using the CO_2 methanation as a study case.
- To define and solve a phenomenological model on an intensified reactor for the methanation in both steady and transient state for the reactor conceptual design.
- To determine the suitable structural geometry and dimensions of an intensified reactor for CO_2 methanation in terms of flow distribution uniformity, CO_2 conversion, and SNG throughput.

1.5 Research question

- To what scale should the intensification process be extended to overcome the typical shortcomings of conventional reactors (namely fixed-bed) employed in the SNG production of power-to-methane applications?

1.6 References − Chapter 1

[1] Earth Science Communications Team at NASA's Jet Propulsion Laboratory, "A blanket around the Earth." [Online]. Available: https://climate.nasa.gov/causes/. [Accessed: 08-Sep-2018].

[2] T. Stocker, *Climate change 2013: the physical science basis: Working Group I contribution to the Fifth assessment report of the Intergovernmental Panel on Climate Change*. Cambridge university press, 2014.

[3] United Nations Framework Convention on Climate Change, "History of the Convention." [Online]. Available: https://unfccc.int/process/the-convention/history-of-the-convention#eq-1. [Accessed: 08-Sep-2018].

[4] C. Breyer, S. Rieke, M. Sterner, and J. Schmid, "Hybrid PV-Wind-Renewable Methane Power Plants--A Potential Cornerstone of Global Energy Supply," in *Proceedings of the 26th European Photovoltaic Solar Energy Conference, Hamburg, Germany*, 2011, vol. 59.

[5] T. Schaaf, J. Grünig, M. R. Schuster, T. Rothenfluh, and A. Orth, "Methanation of CO2 - storage of renewable energy in a gas distribution system," *Energy. Sustain. Soc.*, vol. 4, no. 1, pp. 1–14, 2014.

[6] X. Zhang, C. Bauer, C. L. Mutel, and K. Volkart, "Life Cycle Assessment of Power-to-Gas: Approaches, system variations and their environmental implications," *Appl. Energy*, vol. 190, pp. 326–338, 2017.

[7] M. Götz *et al.*, "Renewable Power-to-Gas: A technological and economic review," *Renew. Energy*, vol. 85, pp. 1371–1390, Jan. 2016.

[8] S. Rönsch *et al.*, "Review on methanation - From fundamentals to current projects," *Fuel*, vol. 166, pp. 276–296, 2016.

[9] A. Zimmermann and M. Kant, "CO2 Utilisation Today," p. 48, 2017.

[10] S. Faramawy, T. Zaki, and A. A.-E. Sakr, "Natural gas origin, composition, and processing: A review," *J. Nat. Gas Sci. Eng.*, vol. 34, pp. 34–54, Aug. 2016.

[11] J. P. Stempien, M. Ni, Q. Sun, and S. H. Chan, "Production of sustainable methane from renewable energy and captured carbon dioxide with the use of Solid Oxide Electrolyzer: A thermodynamic assessment," *Energy*, vol. 82, pp. 714–721, Mar. 2015.

[12] British Petroleum Company, "BP Statistical Review of World Energy June 2017," London, UK, 2017.

[13] Promigas, "Informe del sector gas natural 2017," 2017.

[14] K. Ghaib, K. Nitz, and F.-Z. Ben-Fares, "Chemical Methanation of CO 2 : A Review," *ChemBioEng Rev.*, vol. 3, no. 6, pp. 266–275, Dec. 2016.

[15] K. Ghaib and F.-Z. Ben-Fares, "Power-to-Methane: A state-of-the-art review," *Renew. Sustain. Energy Rev.*, vol. 81, no. June 2017, pp. 433–446, Jan. 2018.

[16] M. Götz, J. Lefebvre, D. Schollenberger, S. Bajohr, R. Reimert, and T. Kolb, "Novel methanation concepts for the production of substitute natural gas," *Int. Gas Res. Conf. Proc.*, vol. 3, no. January, pp. 2313–2320, 2014.

[17] J. Bremer and K. Sundmacher, "Operation range extension via hot-spot control for catalytic CO 2 methanation reactors," *React. Chem. Eng.*, vol. 4, no. 6, pp. 1019–1037, 2019.

[18] D. Schlereth and O. Hinrichsen, "A fixed-bed reactor modeling study on the methanation of CO2," *Chem. Eng. Res. Des.*, vol. 92, no. 4, pp. 702–712, Apr. 2014.

[19] K. H. G. Rätze, J. Bremer, L. T. Biegler, and K. Sundmacher, *Physics-Based Surrogate Models for Optimal Control of a CO2 Methanation Reactor*, vol. 40. Elsevier Masson SAS, 2017.

[20] J. Bremer, K. H. G. Rätze, and K. Sundmacher, "CO 2 methanation: Optimal start-up control of a fixed-bed reactor for power-to-gas applications," *AIChE J.*, vol. 63, no. 1, pp. 23–31, Jan. 2017.

[21] Y. Liu and O. Hinrichsen, "CFD Simulation of Hydrodynamics and Methanation Reactions in a Fluidized-Bed Reactor for the Production of Synthetic Natural Gas," *Ind. Eng. Chem. Res.*, vol. 53, no. 22, pp. 9348–9356, Jun. 2014.

[22] B. Kreitz, G. D. Wehinger, and T. Turek, "Dynamic simulation of the CO2 methanation in a micro-structured fixed-bed reactor," *Chem. Eng. Sci.*, vol. 195, pp. 541–552, Feb. 2019.
[23] J. Ducamp, A. Bengaouer, and P. Baurens, "Modelling and experimental validation of a CO 2 methanation annular cooled fixed-bed reactor exchanger," *Can. J. Chem. Eng.*, vol. 95, no. 2, pp. 241–252, Feb. 2017.
[24] R. Y. Chein, W. Y. Chen, and C. T. Yu, "Numerical simulation of carbon dioxide methanation reaction for synthetic natural gas production in fixed-bed reactors," *J. Nat. Gas Sci. Eng.*, vol. 29, pp. 243–251, Feb. 2016.
[25] M. Gruber *et al.*, "Modeling and Design of a Catalytic Wall Reactor for the Methanation of Carbon Dioxide," *Chemie-Ingenieur-Technik*, vol. 90, no. 5, pp. 615–624, 2018.
[26] D. Sun and D. S. A. Simakov, "Thermal management of a Sabatier reactor for CO2 conversion into CH4: Simulation-based analysis," *J. CO2 Util.*, vol. 21, no. June, pp. 368–382, Oct. 2017.
[27] W. Ehrfeld, V. Hessel, and H. Löwe, *Microreactors*. Wiley, 2000.
[28] P. L. Suryawanshi, S. P. Gumfekar, B. A. Bhanvase, S. H. Sonawane, and M. S. Pimplapure, "A review on microreactors: Reactor fabrication, design, and cutting-edge applications," *Chem. Eng. Sci.*, vol. 189, pp. 431–448, Nov. 2018.
[29] J. Némethné-Sóvágó and M. Benke, "Microreactors: a new concept for chemical synthesis and technological feasibility," *Mater. Sci. Eng.*, vol. 39, no. 2, pp. 89–101, 2014.
[30] H. Freund and K. Sundmacher, "Process Intensification, 3. Process Unit Level," in *Ullmann's Encyclopedia of Industrial Chemistry*, Weinheim, Germany: Wiley-VCH Verlag GmbH & Co. KGaA, 2011, pp. 1–24.
[31] N. Engelbrecht, S. Chiuta, R. C. Everson, H. W. J. P. Neomagus, and D. G. Bessarabov, "Experimentation and CFD modelling of a microchannel reactor for carbon dioxide methanation," *Chem. Eng. J.*, vol. 313, pp. 847–857, Apr. 2017.
[32] P. Breeze, "Nuclear Power," in *Power Generation Technologies*, Third Edit., P. Breeze, Ed. Elsevier, 2019, pp. 399–429.
[33] S. v. Nuclear Power, "Heat Equation – Heat Conduction Equation." [Online]. Available: https://www.nuclear-power.net/nuclear-power/reactor-physics/reactor-operation/shutdown-margin-sdm/. [Accessed: 10-Nov-2020].
[34] F. Jacob and B. Ted, *A first course in finite elements*. Wiley, 2007.
[35] T. J. R. Hughes, *The Finite Element Method: Linear Static and Dynamic Finite Element Analysis*. Dover Publications, 2000.
[36] T. R. Chandrupatla, A. D. Belegundu, T. Ramesh, and C. Ray, *Introduction to finite elements in engineering*, vol. 10. Prentice Hall Upper Saddle River, NJ, 2002.
[37] A. Logg, K.-A. Mardal, G. N. Wells, and others, *Automated Solution of Differential Equations by the Finite Element Method*. Springer, 2012.
[38] M. S. Alnæs *et al.*, "The FEniCS Project Version 1.5," *Arch. Numer. Softw.*, vol. 3, no. 100, 2015.
[39] A. Logg and G. N. Wells, "DOLFIN: Automated Finite Element Computing," *ACM Trans. Math. Softw.*, vol. 37, no. 2, 2010.
[40] H. Petter Langtangen and A. Logg, *Solving PDEs in Python-The FEniCS Tutorial Volume I*, vol. I. Springer, 2017.
[41] W. G. Luscher and K. J. Geelhood, "Material property correlations: comparisons between FRAPCON-3.5, FRAPTRAN 1.5, and MATPRO," Richland, WA (United States), 2014.
[42] S. G. Popov, V. K. Ivanov, J. J. Carbajo, and G. L. Yoder, "Thermophysical Properties of MOX and UO2 Fuels Including the Effects of Irradiation," Oak Ridge, United States, 2000.

CHAPTER 2: Proposal of an open-source computational toolbox for solving PDEs in the context of chemical reaction engineering using FEniCS and complementary components

This chapter's main purpose within the manuscript is to discuss the downsides faced by fixed bed reactors employed in PtM applications for SNG production. To meet this purpose, a parametric sensitivity analysis of the most relevant PtM industrial conditions is performed. Besides, it is worth noting that the above is presented as a case study in a published paper, in which the main goal is to propose a computational toolbox based on the FEniCS Project and some Python modules mentioned in Chapter 1 (above).

Proposal of an open-source computational toolbox for solving PDEs in the context of chemical reaction engineering using FEniCS and complementary components

Santiago Ortiz-Laverde[a], Camilo Rengifo [b], Martha Cobo [a], Manuel Figueredo [a, *]

[a] Energy, Materials and Environment Laboratory, Department of Chemical Engineering, Universidad de La Sabana, Campus Universitario Puente del Común, Km. 7 Autopista Norte, Bogotá, Colombia

[b] Department of Mathematics, Physics and Statistics, Universidad de La Sabana, Campus Universitario Puente del Común, Km. 7 Autopista Norte, Bogotá, Colombia.

* Corresponding author. Email: manuel.figueredo@unisabana.edu.co

2.1 Abstract

In this contribution, an open-source computational toolbox composed of FEniCS and complementary packages is introduced to the chemical and process engineering field by addressing two case studies. First, the oxidation of o-xylene to phthalic anhydride is modelled and used as a FEniCS' proof-of-concept based on a comparison with the software Aspen Custom Modeler (ACM). The results show a maximum absolute error of 2% and thus a good FEniCS/ACM agreement. Second, synthetic natural gas (SNG) production through CO_2 methanation is covered in further detail. In this instance, a parametric study is performed for a tube bundle fixed-bed reactor employing a two-dimensional and transient pseudo-homogeneous model. An operating window for critical variables is evaluated, discussed, and successfully contrasted with the literature. Therefore, the computational toolbox methodology and the consistency of the results are validated, strengthening FEniCS and complements as an interesting alternative to solve mathematical models concerning chemical reaction engineering.

Keywords: Aspen Custom Modeler; Chemical engineering; FEniCS; Open-source computational toolbox; o-xylene oxidation; Power-to-methane.

2.2 Introduction

Computational tools have been evolving considerably, allowing engineers to support their designs not only based on heuristics, but also on increasingly complex calculations. Thus, many software and computing environments have been developed to address distinct engineering problems for industrial applications and research purposes. Mathematical modelling, in which both space and time are described based on conservation laws, is expected to improve prediction accuracy since it provides detailed information about the system behaviour and helps engineers in the prototyping process during the early development stages [1], [2]. Thus, software with solvers capable of computing partial differential equations (PDEs) is required. Nonetheless, most are expensive and hardly accessible to the industry or academic community, leading to an increasing interest in out-of-the-box open-source computational tools.

In this research, FEniCS, Gmsh, ParaView and some Python libraries (e.g., pygmsh, meshio, NumPy, matplotlib and vedo) are employed to perform the computing, mesh generation and data post-processing tasks. The FEniCS Project is a novel open-source computing platform for the automated solution of PDE sets using the finite element method (FEM). It offers high-level scripting by employing Python as the programming language, which enables not only flexibility but also an efficient, streamlined FEM implementation [3]–[5]. Gmsh is an actively maintained finite element meshing framework with a built-in CAD engine and a user interface with advanced visualization capabilities [6]. ParaView is a well-known software in computer science for post-processing and visualization applications. It provides cutting edge tools to inspect and analyse data both qualitatively and quantitatively [7], [8].

The FEniCS Project has been used within a wide range of research fields, such as tidal energy, geoscience, fluid mechanics, theoretical biology, strain gradient elasticity, biophysics and metamodeling [9]–[18]. Abali (2017), for instance, demonstrated several modelling examples with different engineering applications through a continuum mechanics approach. However, there is currently no literature concerning its application in chemical and process engineering. This paper aims to introduce FEniCS and the complementary components as an open-source computational toolbox to solve standard chemical reaction engineering problems for research or educational purposes. To accomplish the latter, two case studies are proposed and solved.

The first case study consists of a fixed-bed reactor simulation for the selective oxidation of *o*-xylene to phthalic anhydride catalysed by V_2O_5/TiO_2. This has been a recognized heterogeneous catalytic process within the petrochemical industry [20] and the subject of several studies looking for enhanced catalyst and reaction technologies due to the existing risk of thermal runaways [21]–[27]. This case study became a landmark example for chemical reactor analysis and design in assessing hot spot formation, as first proposed by Froment et al. (1990). It has also been used to evaluate other process engineering software, as in the case of Oh and Pantelides (1996), who

adopted it to illustrate the capability of process modelling languages using the gPROMS framework. It is currently part of the Aspen Custom Modeler (ACM) software documentation as an example in the PDE modelling section [30].

In fact, ACM is software developed by AspenTech, a company with high recognition in academia and industry, given its background in engineering process modelling, simulation, and optimization. Therefore, unlike other open-source platforms/packages that, as well as FEniCS, are intended to solve PDEs, ACM not only provides an environment for computing custom-based PDEs with the desired level of flexibility and sophistication but is also the only one aimed at modelling and simulating engineering processes. Furthermore, ACM takes advantage of the Aspen properties databases, enabling the export of customized models as process equipment into other featured AspenTech products, such as Aspen Hysys and Aspen Plus. Accordingly, phthalic anhydride synthesis is a well-known and studied problem and serves as a proof-of-concept case study of FEniCS in the field of chemical and process engineering when comparing the results with the solution computed via ACM. Then, the same reactor dimensions and conditions recorded by Oh and Pantelides (1996) and the ACM documentation were computed using FEniCS.

On the other hand, the second case study is intended to highlight the computational toolbox applicability in a topic of interest to today's scientific community and one of the Energy, Materials, and Environment Laboratory's leading research lines. This case is then the foremost approach of the paper and addresses the catalytic production of synthetic natural gas (SNG). A state-of-the-art research problem immersed in the power-to-methane (P2M) context that has begun to attract significant attention is proposed as a promising strategy to reduce global greenhouse gas (GHG) emissions while allowing low-carbon footprint power generation [31].

P2M implies the capture of carbon dioxide (CO_2) from distinct GHG sources and its subsequent catalytic transformation (chemically known as methanation) into SNG using water (H_2O) and surplus renewable electricity (e.g., wind, solar, hydro) [32], [33]. One of the major difficulties concerning CO_2 methanation is appropriate heat management due to its highly exothermic nature. This task becomes more challenging within P2M at the industrial level when intermittency is introduced to the operation, due to the fluctuations in the hydrogen supply chain (water electrolysis powered by renewable energies) [34], [35]. Some investigations have addressed these challenges in CO_2 methanation by paying attention to the reaction engineering aspects from a modelling and simulation perspective. Table 2-1 shows an overview of recent studies in reactor modelling in CO_2 methanation, reporting the simulated systems, model complexity, and software and numerical methods thus far employed.

Table 2-1. Overview of reactor modelling for CO_2 methanation.

Catalytic reactor type	Model nature	Software/Computing environment	Numerical method(s)	Reference
Fixed-bed	Dynamic – 1D (PDE)	CasADi [ʃ]	FVM	Zimmermann et al. (2020)
Micro packed-bed	Stationary – 1D (ODE)	MATLAB® ode15s	NDFs	Farsi et al. (2020)
Slurry bubble column	Dynamic – 1D (PDE)	MATLAB® ode15s	MOL/NDFs	Lefebvre et al. (2020)
Fluidized-bed	Stationary – 1D (ODE)	MATLAB® ode15s	NDFs	Jia et al. (2020)
Fixed-bed and intensified	Dynamic – 2D (PDE)	CasADi [ʃ]	FVM	Bremer and Sundmacher (2019)
Micro-structured fixed-bed	Dynamic – 1D (PDE)	gPROMS ModelBuilder	BFD1	Kreitz et al. (2019b)
Catalyst coated on heat exchanger	Stationary – 2D, 3D (PDE)	COMSOL Multyphysics®	FEM	Vidal Vázquez et al. (2018)
Plug flow	Stationary – 1D (ODE), 3D (PDE)	COMSOL Multyphysics® / Ansys®	FEM/FVM	Gruber et al. (2018)
Fixed-bed	Dynamic – 1D, 2D (PDE)	n.s./CasADi [ʃ]	n.s./FVM	Rätze et al. (2017)
Fixed-bed	Dynamic – 2D (PDE)	CasADi [ʃ]	FVM	Bremer et al. (2017)
Microchannel	Stationary – 3D (PDE)	COMSOL Multyphysics®	FEM	Engelbrecht et al. (2017)
Fixed-bed	Stationary – 2D (PDE)	COMSOL Multyphysics®	FEM	Ducamp et al. (2017)
Fixed -bed	Dynamic – 1D (PDE)	MATLAB® PDE solver/ode15s	FEM/NDFs	[48]
Fixed-bed	Dynamic – 1D (PDE)	MATLAB® PDE solver/ode15s	FEM/NDFs	[49]
Fixed-bed	Stationary – 2D (PDE)	COMSOL Multyphysics®	FEM	Chein et al. (2016)
Fixed-bed	Stationary – 1D (ODE), 2D (PDE)	MATLAB® ode15s and bvp4c-s/COMSOL Multyphysics®	NDFs/FEM	Schlereth and Hinrichsen (2014)
Fluidized-bed	Dynamic – 2D (PDE)	OpenFoam	FVM	Liu and Hinrichsen (2014)

Abbreviations at the end of the manuscript. [ʃ] CasADi framework in MATLAB® [53]. n.s. is not specified.

According to Table 2-1, seventeen studies have assessed the reaction engineering considerations in CO_2 methanation through modelling and simulation. In short, most of them (~88 %) relied on PDE systems, giving robustness to mathematical modelling. Almost half (~53 %) considered dynamic models with the notion that methanation reactors need to handle load intermittency and be started up and shut down frequently within the P2M context. Among those, four studies (~23 %) considered two/three-dimensional (2D/3D) spatial distributions aside from transitory effects; in such studies, the finite volume method (FVM) was used. Indeed, Schlereth and Hinrichsen (2014) and Rätze et al. (2017) argued the importance of a radial description of the temperature profile to have a quantitative evaluation rather than a qualitative trend, especially under dynamic reactor operations. Last, only 1 study adopted open-source software to develop the modelling calculations, and Liu and Hinrichsen (2014) performed CFD simulations in OpenFoam to analyse the hydrodynamics and methanation reactions in a fluidized-bed reactor, which shows the lack of employment of open-source tools in the numerical analysis of CO_2 methanation systems.

Therefore, in the second case study FEniCS and complementary open-source tools are employed to address a chemical engineering problem within the P2M context. More precisely, the effect of various operational variables on hot spot formation and CO_2 conversion is evaluated in an average tube bundle fixed-bed reactor through a 2D dynamic model. The obtained results are qualitatively and quantitatively contrasted with the recorded literature to ascertain their reliability, and the analysis contributes to creating the big picture of the parametric sensitivity of the CO_2 methanation process. Together with the first case study, this demonstrates the feasibility of the proposed computational toolbox within a research scenario in the chemical and process engineering fields.

The nomenclature and abbreviations used throughout the text are listed at the end of the Chapter 2 (Section 2.6) for ease of reading.

2.3 Computational toolbox and methodology

The two case studies are addressed through a series of sequential steps. The first is to identify the PDEs (PDE set) describing the modelled phenomena, the computational or discretized domain, and the corresponding boundary conditions. Once the former has been established, the second step consists of generating the FEM mesh according to the required accuracy. Then, the mathematical model is reformulated as a finite element variational problem (also known as the weak formulation), followed by a Python program in which the mathematical problem is computed over the discretized domain through FEniCS abstractions. The last step consists of storing the data for post-processing purposes (e.g., visualization). While Gmsh (in-line with pygmsh and meshio) and FEniCS combine the meshing and subsequent FEM application, ParaView (plus certain Python modules) is used for data post-processing. Accordingly, the proposed open-source toolbox and its interoperability are described in more detail in this section.

2.3.1 Mesh generation

To select an appropriate meshing tool, some of the most commonly used tools were identified without any prior attachment. The decision was based on a review article by Spencer Smith et al. (2016) and the information available within the FEniCS community. In the former, 27 Mesh Generation and Mesh Processing (MGMP) software programs were assessed. Their analysis criteria included software maintainability, usability, reusability, and performance. Although this research is not completely updated, it provides a general review of the available software in the field, their shortcomings, and strengths.

According to this review, the top 5 MGMP projects ranked by quality were CGAL [55], MeshLab [56], TetGen [57], snappyHexMesh [58] and Gmsh [6]. All of these methods are open-source and demonstrate surface robustness (appropriate error handling). Regarding operating system portability, CGAL, MeshLab, TetGen and Gmsh may be supported in Windows, Linux and OSX, while snappyHexMesh is only supported in Linux. However, MeshLab and TetGen solely support meshing of triangular and tetrahedral elements for 3D polyhedral-type domains, whereas snappyHexMesh is used mainly as a mesh generator tool for OpenFoam in 3D meshes containing hexahedra and split-hexahedra (where triangulated surface geometries are required as inputs).

On the other hand, both CGAL and Gmsh support 1, 2 and 3D meshes and have been employed as FEniCS external mesh generators. In addition, the user may build customized meshes through native scripting in each software, which is advantageous because it makes the creation of complex geometries more flexible. Notwithstanding, the implementation of Gmsh was found to be easier since there seems to be more information in the community forums concerning Gmsh format treatment and conversion according to feasible FEniCS inputs. Furthermore, the Python package pygmsh enables the creation of finite element meshes through the Python scripting language liaised with the Gmsh API [59]. The latter makes the creation of Gmsh meshes more versatile and automates the meshing process within the FEniCS computing environment itself. As a result, Gmsh (powered by pygmsh) was incorporated in the proposed computational toolbox as the mesh generation tool. In addition, Gmsh provided an appropriate refinement for triangular meshes over slimline geometries, such as the ones used herein with both case studies.

2.3.2 FEniCS and the FEM

With high-level Python and C++ as programming languages, FEniCS is a modern collection of open-source software components directed at the automated solution of PDEs via FEM [3]–[5]. One of the distinguishing features of FEM consists of rewriting the mathematical model as a variational problem (also known as weak formulation). To formulate the variational problem, each PDE is multiplied by a function v (called the test function) and integrated over its respective domain, where all the second-order terms are integrated by parts. Eqs. (2.1)-(2.3) briefly describe

this procedure with a Poisson-like problem, where f accounts for a source term (see Petter Langtangen and Logg (2017)).

$$-\nabla^2 u = f \qquad in\ \Omega. \tag{2.1}$$

$$\int_\Omega (\nabla^2 u) v\, dx = \oint_{\partial\Omega} v\, \nabla u\, \mathrm{ds} - \int_\Omega (\nabla v)\cdot(\nabla u)\, dx\,, \tag{2.2}$$

$$\mathrm{F}(u;\, v) = \int_\Omega vf\, dx + \oint_{\partial\Omega} v\, \nabla u\, \mathrm{ds} - \int_\Omega (\nabla v)\cdot(\nabla u)\, dx\,, \tag{2.3}$$

where Ω refers to the physical domain and $\partial\Omega$ refers to the system boundary. Note that the boundary conditions are incorporated in the path integral. In addition, both v and u (trial function to be approximated) are functions that belong to so-called settled function spaces. These spaces of functions consist of piecewise polynomial functions with particular properties in a way that guarantees the continuity of the solution across element boundaries. This research adopts first-order Lagrange polynomials (P1) to approximate the numerical solutions. Once the weak-formulation is stated (e.g., Eq. (2.1)), a Python program using the corresponding FEniCS abstractions is written. The called solver depends on the nature of the variational problem or whether or not the F statement is linear. The case studies discussed in this paper are nonlinear.

2.3.3 FEniCS and complements: Interoperability

Figure 2-1 provides a conceptual description of the proposed toolbox interoperability and the following procedure to solve the case studies outlined hereafter. Dotted boxes enclose the respective stages of the computational workflow, while the continuous boxes compose the intercommunication path.

By convention, Gmsh uses the .geo extension (ext.) to create geometric objects before being processed in the mesh refinement. The Python package pygmsh provides an alternative to Gmsh native scripting through a Python interface [59]. During the creation of geometries (using pygmsh), one may mark specific regions in the geometric object as "physical"; thus, they can be later interpreted as boundaries ($\partial\Omega$) or domains (Ω). The mesh object created by pygmsh (*.msh* ext.) employing the Gmsh in-house kernels can be converted into formats that support parallel processing. Thus, a preliminary conversion to the XDMF/HDF5 format is required (which is an efficient way to store files both in terms of speed and file sizes) [61]. It may be accomplished through the Python package meshio since it allows the conversion of *.msh* files (or other ext.) into several formats [62]. The meshio package splits apart the "physical" and "elementary" entities stored in the *.msh* file so that FEniCS may recognize them before discretization.

After that, test (v_i) and trial (u_i) function spaces are declared based on the type and degree of the

selected finite element (polynomial family and order). The latter is followed by the variational formulation statement and the solver setup. Next, the simulation is run, and the results computed by the FEniCS may be stored for visualization or reused later in Python-FEniCS computations. The results are stored in the HDF5 format, which is designed to support I/O parallel operations and is useful for high-performance computing (HPC) [60], [63], [64].

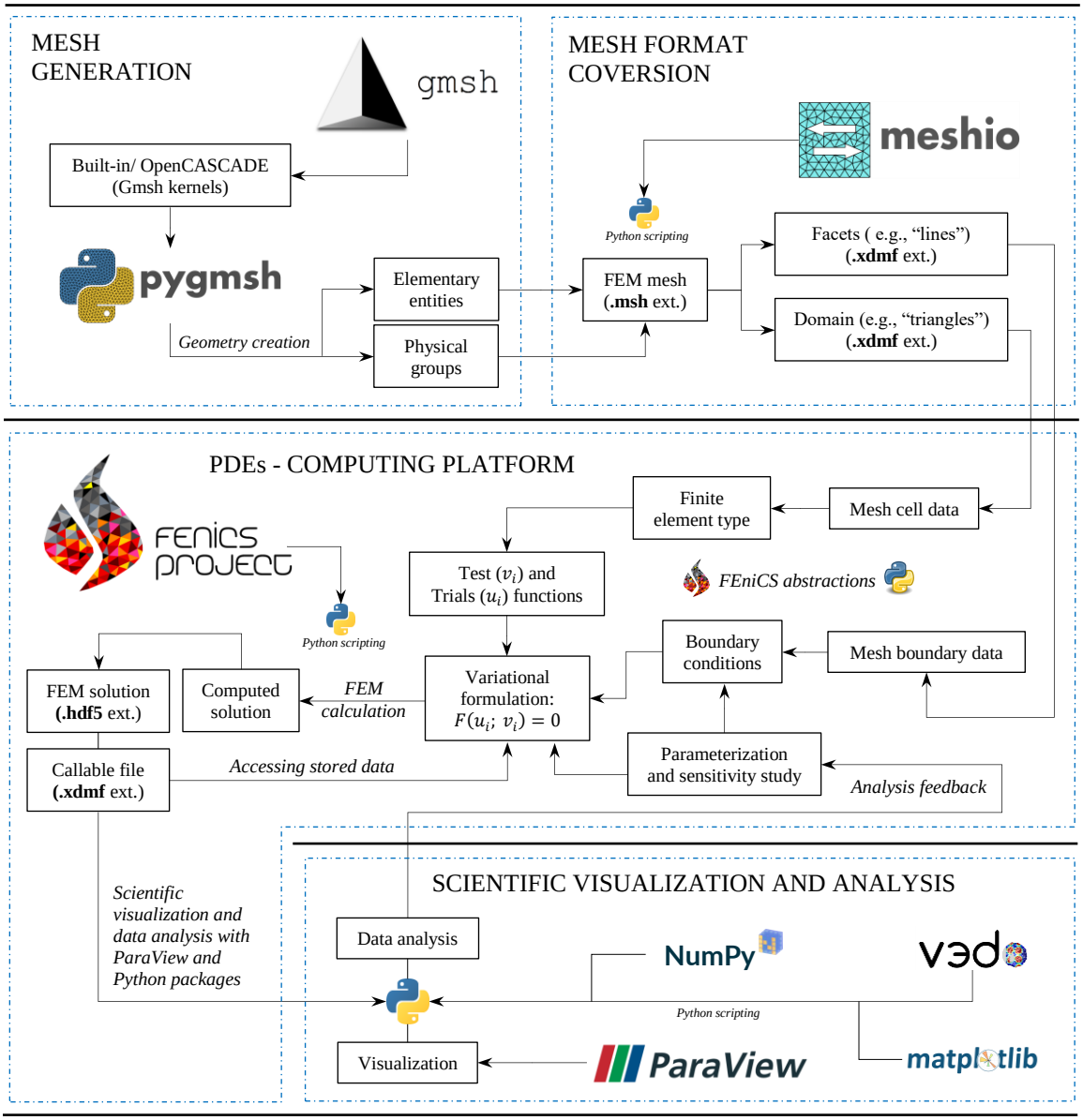

Figure 2-1. Open-source toolbox interoperability.

The next stage in the workflow is the post-processing of data. Since the entire process is performed through a Python interface, popular libraries for data manipulation and visualization, such as Numpy and matplotlib, or more specialized scientific modules for finite element visualization,

such as vedo (formerly known as vtkplotter; Musy et al., 2020, 2019), are available. Regarding external tools, ParaView excels as a proper open-source software for the visualization and analysis of numerical solutions. This tool includes the ability to handle different formats (e.g., VTK, XDMF/HDF5, PVD) and affords a 3D-object interaction environment once the datasets have been imported [7], [8]. Finally, a parametric sensitivity study is undertaken to obtain information about the mathematical model, with the possibility of being permanently fed back from the same analysed data after each simulation.

2.3.4 Case studies

2.3.4.1 Phthalic Anhydride synthesis

2.3.4.1.1 Reactor model description

At the industrial scale, the selective oxidation of *o*-xylene to phthalic anhydride has been mostly conducted in multi-tubular fixed-bed reactors, composed of approximately 2500 to 20000 parallel tubes (each 3 m long, with an internal diameter of 2.54 cm) and cooled through circulating molten salts [67]. Herein, only a single of those packed-bed tubes was considered. The resulting equations for a 2D pseudo-homogeneous model are presented in Table 2-2. The total heat exchanged with the cooling jacket is expressed as an integral over the entire tube length (see Eq. (2.6)). Danckwerts-type boundary conditions were applied at the entrance of the reactor, whereas the initial conditions for compositions and bed/coolant temperature were set to zero and 625 K, respectively. The catalytic rate model for V_2O_5 was assumed to be first-order with respect to each reagent, despite the presence of an excess of oxygen during the gas-phase air oxidation of o-xylene (Oh and Pantelides, 1996). The physical properties remained constant over the range of the process operating conditions and are given in the supplementary material.

Table 2-2. Model equations for the phthalic anhydride synthesis reactor.

Description	Mathematical expression	Eq.
Mass balance for component i	$\frac{\partial C_i}{\partial t} = -\boldsymbol{\vartheta}\cdot\vec{\nabla}C_i + \varepsilon D^{eff}\,(\nabla^2 C_i) + v_{i,\,oxy}\,\rho_b\,r_{oxy}$	(2.4)
Energy balance for packed-bed	$(\rho\,\mathrm{C_p})_{gas}\frac{\partial T}{\partial t} = -\boldsymbol{\vartheta}\cdot\vec{\nabla}T + \lambda^{eff}\,(\nabla^2 T) + \rho_b\left(\Delta_R H_{oxy}\right) r_{oxy}$	(2.5)
Energy balance for cooling jacket	$(\rho\,\mathrm{C_p})_{cool}\frac{\partial T_{cool}}{\partial t} = (F\,C_p)_{cool}(T_{cool,\,f} - T_{cool}) + (\mathrm{U\,A})_w\int_0^L [T_w(z,L) - T_{cool}]\,dz$	(2.6)
Boundary conditions for component i	$\varepsilon D_z\left.\frac{\partial C_i}{\partial z}\right\|_{z=0} = \vartheta_z(C_i - C_{i,f})$ $\qquad$ $\left.\frac{\partial C_i}{\partial x}\right\|_{r=0} = 0$	(2.7)

	$\left.\frac{\partial C_i}{\partial z}\right\|_{z=L} = 0$		$\left.\frac{\partial C_i}{\partial x}\right\|_{r=L} = 0$
Boundary conditions for the packed-bed Temperature	$\lambda_z \left.\frac{\partial T}{\partial z}\right\|_{z=0} = \left(\rho\, C_p\right)_{gas} \vartheta_z \left(T - T_f\right)$		$\lambda_x \left.\frac{\partial T}{\partial x}\right\|_{r=L} = U_w (T_{cool} - T)$
	$\left.\frac{\partial T}{\partial z}\right\|_{z=L} = 0$		$\left.\frac{\partial T}{\partial x}\right\|_{r=0} = 0$

(2.8)

2.3.4.1.2 ACM and FEniCS numerical procedure

This case study was solved in line with the solution methodology previously described. Gmsh (powered by pygmsh) was used to mesh the reactor domain, and the corresponding variational problem was formulated for Eqs. (2.4)-(2.5) and tied down to Eqs. (2.7)-(2.8). Additionally, the same mathematical model was implemented in ACM to validate the FEniCS computation. Two numerical methods discretized the spatial domain in the ACM: a 1st-order backward finite difference (BFD1) was applied to the axial coordinate, and a 3rd-order orthogonal collocation on finite elements (OCFE3) was settled along the radial distribution. Regarding the temporal dimension, a simple BFD1 discretization was acceptable in FEniCS while providing stability to the system. In contrast, ACM employs the Method of Lines (MOL) for dynamic- and spatial-distributed problems. As a result, the discretized domain in the ACM was formed by quadrilateral elements, unlike the triangular mesh used in FEniCS. This discrepancy hinders the numerical comparison of the results. Therefore, once the PDE set was solved in FEniCS, the triangular mesh was squared to a matrix of the same shape as the ACM quadrangular mesh (made of 12010 elements). Likewise, the pygmsh mesh was sufficiently refined with 101040 triangular elements to minimize additional errors due to the comparison process, so the nodes within each new square element could be averaged. Table 2-3 presents the aforementioned numerical information for both computing platforms.

Table 2-3. Information on numerical methods for case study 1 (using ACM and FEniCS).

Computing platform	Finite elements		Numerical discretization		
	Type	Number of nodes	Axial	Radial	Temporal
FEniCS	Triangular	101040	FEM		BFD1
ACM	Quadrilaterals	12010	BFD1	OCFE3	MOL

To facilitate the replication of results concerning this case study and an expanded understanding of the toolbox scheme shown in Figure 2-1, the detailed variational formulation is given in the Supplementary Material along with some results, and the FEniCS/ACM source codes are provided as Research Data, made available online for academic and non-commercial use at a public repository on GitHub (link: GitHub/mafigueredom/RxEngToolbox).

2.3.4.2 Catalytic production of Synthetic Natural Gas (SNG)

2.3.4.2.1 System description

The CO_2 methanation (Eq. (2.9)), also referred to as the Sabatier reaction, is a strongly exothermic reaction; therefore, the catalytic systems in which it is held have been designed to avoid excessive overheating. Cooled tube bundle systems are the most commonly used systems for the methanation process [31], [33], [35]. These reactors are composed of heat exchangers and reacting tubes of relatively small diameters (2 - 5 cm) placed in parallel, which favours heat dissipation and ease of temperature management [68], [69]. Accordingly, to analyse a reasonable case study at the industrial scale within the P2M context, this paper reproduces the same dimensions evaluated previously in [40], [45], as well as some other parameters (e.g., catalyst bed porosity (ε) and cooling jacket values). It is assumed that all tubes within the multi-tubular reactor present the same behaviour, and thus only one channel is modelled. The simulated system is shown in Figure 2-2, and some reactor and catalyst parameters are given in Appendix A (below).

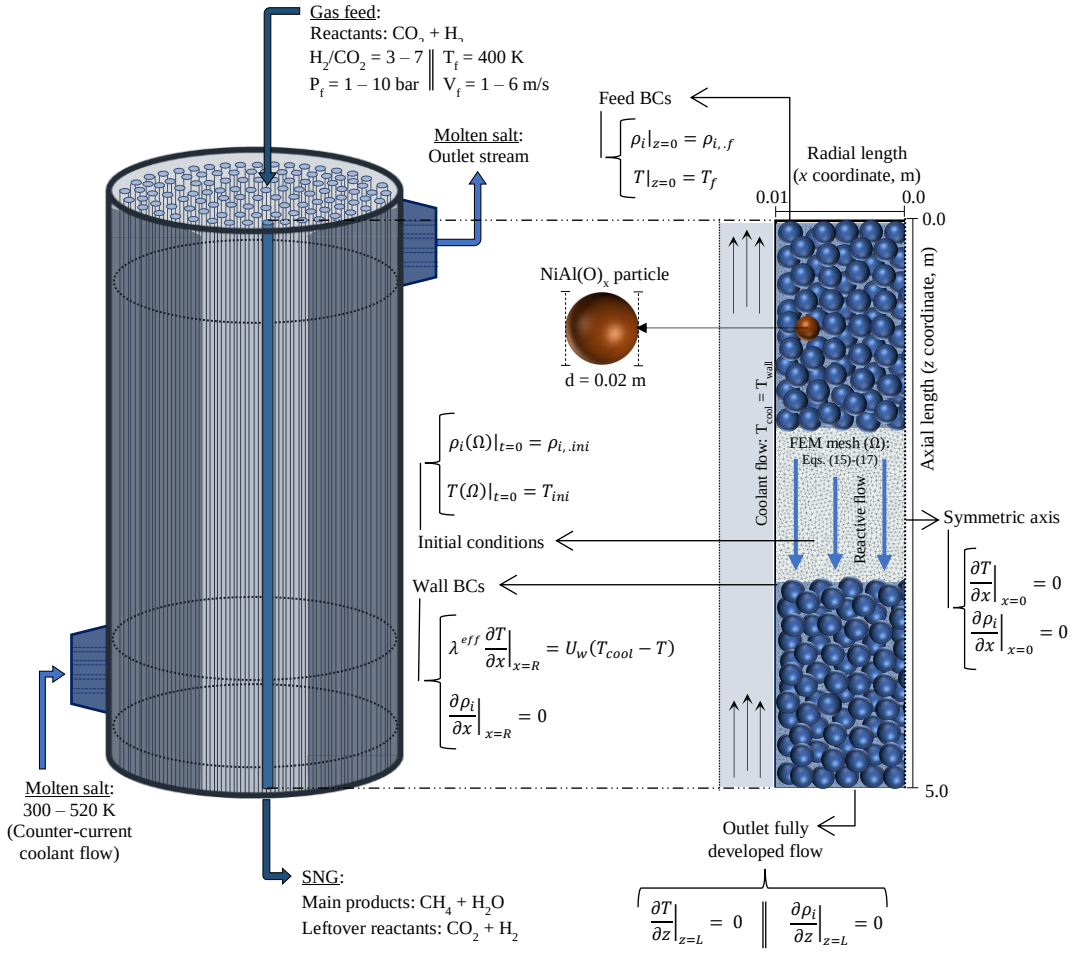

Figure 2-2. Schematic diagram of the tube bundle fixed-bed reactor packed with spherical NiAl(O)x for CO_2 methanation.

$$CO_2 + 4H_2 \Leftrightarrow CH_4 + 2H_2O, \quad \Delta H_R^{298K} = -164.9\ KJ\ mol^{-1}. \tag{2.9}$$

2.3.4.2.2 Governing equations and model assumptions

A transient, pseudo-homogeneous mathematical model was employed to simulate the reactor operation. The reacting flow modelling for the methanation process results from the coupling of governing mass, heat, and flow transport. Herein, the gradient operator $\vec{\nabla}$ accounts for the vector $\frac{\partial}{\partial x}\hat{\imath} + \frac{\partial}{\partial z}\hat{\jmath}$, which provides a 2D notation for the model spatial distribution (see Table 2-4).

Table 2-4. Summary of governing equations for the CO_2 methanation reactor (pseudo-homogeneous approach).

Description	Mathematical expression	Eq.
Species continuity equation	$\varepsilon \frac{\partial \rho_i}{\partial t} = -\boldsymbol{\vartheta} \cdot \vec{\nabla}\rho_i + D_i^{eff}(\nabla^2 \rho_i) + (1-\varepsilon) M_i \nu_{i,Sab} r_{Sab}^{eff}$	(2.10)
Energy equation	$(\rho C_p)_{gas}^{eff} \frac{\partial T}{\partial t} = -\sum_i \left(\rho_i C_{p_i}\right) \boldsymbol{\vartheta} \cdot \vec{\nabla} T + \lambda^{eff}(\nabla^2 T) - (1-\varepsilon)(\Delta_R H_{Sab}) r_{Sab}^{eff}$	(2.11)
Ergun equation	$\frac{dp}{dz} = -150 \frac{(1-\varepsilon)^2 \mu_{gas}}{{d_p}^2 \varepsilon^3} \vartheta_z - 1.75 \frac{(1-\varepsilon)\rho_{gas}}{d_p \varepsilon^3} {\vartheta_z}^2$	(2.12)
Boundary and initial conditions for component i	$\rho_i\|_{z=0} = \rho_{i,f}$ $\frac{\partial \rho_i}{\partial z}\Big\|_{z=L} = 0$ $\frac{\partial \rho_i}{\partial x}\Big\|_{x=R} = 0$ $\frac{\partial \rho_i}{\partial x}\Big\|_{x=0} = 0$ $\rho_i(\Omega)\|_{t=0} = \rho_{i,.ini}$	(2.13)
Boundary and initial conditions for the packed-bed Temperature	$T\|_{z=0} = T_f$ $\frac{\partial T}{\partial z}\Big\|_{z=L} = 0$ $\frac{\partial T}{\partial x}\Big\|_{x=0} = 0$ $\lambda^{eff} \frac{\partial T}{\partial x}\Big\|_{x=R} = U_w(T_{cool} - T)$ $T(\Omega)\|_{t=0} = T_{ini}$	(2.14)

Further details on the approaches used for the calculation of the mass $\left(D_i^{eff}\right)$ and heat $\left(\lambda^{eff}\right)$ dispersion effective coefficients can be found in the Supplementary Material. In addition, the

effective volumetric heat capacity and other thermo-physical properties are estimated, as shown in [45]. In any case, the temperature-dependent correlations for the heat capacity, thermal conductivity and dynamic viscosity were obtained by polynomial correlations from the VDI Heat Atlas [70]. The pressure drop along the axial reactor coordinate was incorporated through the Ergun equation (Eq. (2.12)), while the multicomponent gas mixture was assumed to follow ideal gas behaviour. Moreover, the governing equations were solved by subjecting to some boundary and initial conditions (BCs) given by Eqs. (2.13)-(2.14) in Table 2-4. No variations were accounted for at the reactor inlet leading to Dirichlet (or first-type) BCs. Likewise, the inlet values were also set as initial conditions, preventing numerical convergence issues during the simulation start-up. A constant wall temperature (justified by high coolant flows) was applied at the reactor wall, resulting in a Robin BC for the temperature distribution, while the effective heat transfer coefficient at the wall was assumed to be uniform and without thermal resistances along the interface. Zero normal gradients in the temperature and species concentration were assumed at the central axis and reactor outlet due to symmetry and full flow development, respectively. Last, the superficial gas velocity (in the z coordinate) was corrected based on the molar flow shift that occurs along the reactor, as described by Eq. (2.15):

$$\vartheta_z = \vartheta_{z,f} \, {C_{gas,f}}\Big/{C_{gas}} \tag{2.15}$$

2.3.4.2.3 CO_2 methanation kinetics

The CO_2 methanation (Eq. (2.9)) may take place together with the endothermic reverse water gas shift (RWGS) and exothermic CO methanation reactions. Nevertheless, it has been shown that the latter two might be negligible under typical CO_2 methanation conditions due to the low amount of CO produced [40], [71]–[73]. As a result, this case study relies on a state-of-the-art kinetic model proposed by Koschany et al. (2016) for the CO_2 methanation reaction catalysed by NiAl(O)x and evaluated under industrial conditions. The adopted rate model for the CO_2 methanation reaction is of the type LHHW, as shown in Eq. (2.16):

$$r_{Sab}^{intr}(T;p_i) = \frac{k(T)\, p_{H_2}^{0.5} p_{CO_2}^{0.5} \left(1 - \frac{p_{CH_4} p_{H_2O}^{2}}{p_{CO_2} p_{H_2}^{4} K_{eq}(T)}\right)}{1 + K_{OH}(T)\frac{p_{H_2O}}{p_{H_2}^{0.5}} + K_{H_2}(T) p_{H_2}^{0.5} + K_{mix}(T) p_{CO_2}^{0.5}} \, . \tag{2.16}$$

For further details about adsorption and equilibrium constants, as well as parametrization for the catalytic rate model, see the Supplementary Material.

Moreover, the intrinsic reaction rate (Eq. (2.16)) is constrained by transport limitations that should be considered to estimate the corresponding effective reaction rate. Some studies have shown that interphase (external) transport limitations can be neglected for the size of catalytic pellets (~3 mm)

[49], [74], in contrast to intraparticle (internal) diffusion resistances, which are not negligible. However, the calculation of an effectiveness factor accounting for internal mass-transport limitations brings considerable computational complexity. Hence, to avoid this additional computation time, an effectiveness factor (η) of 0.1 is used, as reported by Wesenberg and Svendsen (2007) and exemplified by Bremer et al. (2017). Eq. (2.17) relates the effective (computed with governing equations) and intrinsic reaction rates, where ς refers to a conversion factor.

$$r_{Sab}^{\ eff} = \eta\, \varsigma\, r_{Sab}^{\ intr} \ . \tag{2.17}$$

2.3.4.2.4 Variational formulation

The variational problem concept mentioned in Section 2.3.2 was applied to Eqs. (2.10)-(2.14), and the variational formulation for each governing equation is presented Table 2-5.

Table 2-5. Variational formulation for governing equations (see Table 2-4).

Description	Mathematical expression	Eq.
V.F. for species mass-transport Eq. 15	$\mathrm{F}_i^{\,n+1}(\rho_i;\, v_i) = \int_\Omega \varepsilon \left(\frac{{\rho_i}^{n+1} - {\rho_i}^{n}}{\Delta t}\right) v_i\, dx + \left(\boldsymbol{\vartheta}\cdot\vec{\nabla}\rho_i\right)^{n+1} v_i\, dx$ $- \int_\Omega (1-\varepsilon)\left(M_i\, \nu_{i,\,Sab}\, r_{Sab}^{\ eff}\right)^{n+1} v_i\, dx + \int_\Omega \left(D_i^{\ eff}\left(\vec{\nabla}\rho_i\cdot\vec{\nabla}v_i\right)\right)^{n+1} dx$	(2.18)
V.F. for the energy-transport Eq. 16	$\mathrm{F}_T^{\,n+1}(T;\, v_T) = \int_\Omega \left[\left(\rho \mathrm{C_p}\right)_{gas}^{eff}\right]^{n+1} \left(\frac{T^{n+1} - T^{n}}{\Delta t}\right) v_T\, dx$ $+ \int_\Omega \left[\sum_i \left(\rho_i \mathrm{C_{p_i}}\right)\boldsymbol{\vartheta}\cdot\vec{\nabla}T\right]^{n+1} v_T\, dx + \int_\Omega (1-\varepsilon)\left(\Delta_R H_{Sab}\, r_{Sab}^{\ eff}\right)^{n+1} v_T\, dx$ $+ \int_\Omega \left(\lambda^{eff}\left(\vec{\nabla}T\cdot\vec{\nabla}v_T\right)\right)^{n+1} dx - \oint_{\partial\Omega} U_w (T_{cool} - T)\, v_T\, ds_w$	(2.19)
V.F. for the Ergun equation Eq. 17	$\mathrm{F}_p^{\,n+1}(P;\, v_P) = \int_\Omega \left(\frac{dp}{dz}\right)^{n+1} v_P\, dx + \int_\Omega \left[150\frac{(1-\varepsilon)^2 \mu_{gas}}{{\mathrm{d_p}}^2\, \varepsilon^3}\vartheta_z\right]^{n+1} v_P\, dx$ $+ \int_\Omega \left[1.75\frac{(1-\varepsilon)\rho_{gas}}{\mathrm{d_p}\, \varepsilon^3}{\vartheta_z}^2\right]^{n+1} v_P\, dx$	(2.20)
Global V.F. statement	$\mathrm{F}^{n+1}(\rho_i;\, T;\, P;\, v) = \sum_i \mathrm{F}_i^{\,n+1}(\rho_i;\, v_i) + \mathrm{F}_T^{\,n+1}(T;\, v_T) + \mathrm{F}_P^{\,n+1}(P;\, v_P)\ in\ \Omega$	(2.21)

V.F. refers to Variational Formulation

Note that all the time-derivative terms can be approximated by a backward finite difference for simplicity and stability reasons. Additionally, only Robin-type and non-natural Neuman BCs appear in the variational formulation (e.g., Eq. (2.19)). The remainder (Dirichlet and natural Neuman) vanish but must be applied to the corresponding $\partial\Omega$ in the Python program through a few FEniCS abstractions, which also constrains the FEM solution to those BCs.

2.3.4.3 Computational aspects

Specifications regarding the computer equipment employed to perform the computations are summarized in Table 2-6, where no GPU was utilized. The first case study was solved via serial processing despite the fine mesh employed on it, contrary to the second case in which the simulations were run by parallel execution. The reason for this is the numerical complexity exhibited by the set of PDEs in the second case study (despite the coarser mesh used on it), for which grid independence was achieved on up to 8908 triangular elements. Indeed, FEniCS offers flexible parallel computing by partitioning the domain, while the solver computes the solution for each piece separately. This process is accomplished by harnessing the I/O parallel capabilities provided by the XDMF and HDF5 files.

Table 2-6. Computational resources.

Operating system	Windows Subsystem for Linux
Processor	Intel(R) Xeon(R) CPU E5-1620 v4 @ 3.50 GHz
CPU cores	4 Cores, 8 Logical Processors
Installed physical RAM	32.0 GB
Hard Disk Drive (HDD)	4TB Hard Drive SATA - 5400 RPM 3.5-inch

This architecture and FEM setup led to CPU times of less than 1 h and approximately 3 h per simulation for the first and second case studies, respectively. Furthermore, dynamic simulations used 500 steps over the total discrete time in both cases (5 s for the former and approximately 1000-1500 s for the latter). In general, 3D simulations were found to be extremely computationally expensive without further differences in the results from the 2D equivalent cases.

2.4 Results and discussion

2.4.1 Case study 1 – Phthalic anhydride synthesis

The presence of excess oxygen in the selective oxidation of *o*-xylene to phthalic anhydride causes the reaction rate model to be dependent only on kinetic terms rather than thermodynamics. Then, the oxidation reaction behaves irreversibly with complete conversion as the maximum possible, along with thermal effects within the system of the one-way direction. Moreover, while the conversion presents negligible radial gradients, the temperature profile shows a distinct radial

variation due to the formation of a hot spot. Thus, comparing the results from both FEniCS and ACM is acceptable to contrast the conversion profile along the reactor's mid-axis and the temperature over the entire domain. All the contrasting results were retrieved from the last step in the dynamic simulation (stationary state reached). Figure 2-3 shows the conversion profile in both platforms with a complete conversion near 0.2 (z/L) and a maximum absolute error of ~0.64 %, as defined in Eq. (2.22).

$$\delta = 100 \cdot \left| \left(n_j^{FEniCS} - n_j^{ACM} \right) \Big/ n_j^{ACM} \right| \tag{2.22}$$

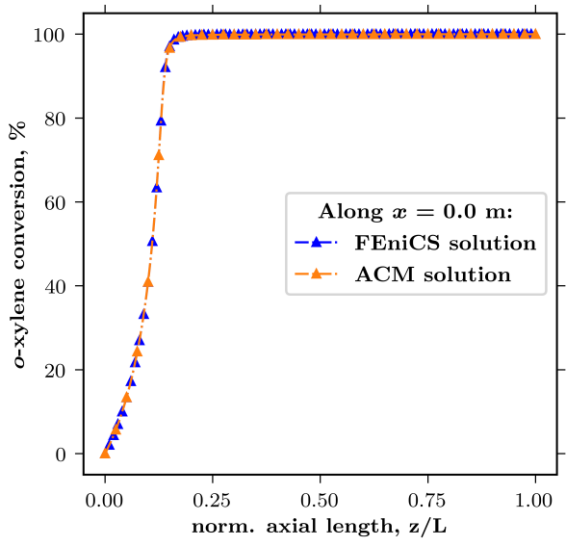

Figure 2-3. Profiles of o-xylene conversion obtained in both FEniCS and ACM.

On the other hand, the fine FEniCS mesh as described in Section 0 was adapted by averaging node values per quadrilateral element to enable a comparison between the 2D distributed profiles. This approach is considered fair enough, as the maximum coefficient of variation (CV) per element in the new quadrangular mesh was below 1% (see Supplementary Material). Figure 2-4 shows the absolute error between the thermal maps obtained from FEniCS and ACM. This error was calculated using Eq. (2.22) per equivalent node (n_j) over the 2D discretized domain. No error above ~2 % was found, and the most significant differences were contemplated over the hot spot region and particularly in the proximity of the cooling jacket.

The small differences in both the conversion and temperature profiles are due to the varied numerical methods employed in each platform (FEM in FEniCS and BFD1/OCFE3 in ACM). Notwithstanding, a solid consistency was found between the results. Regarding the CPU times, FEniCS performed faster than ACM by a factor of ~1.7, although the triangular mesh employed in FEniCS had ~8 times more finite elements than the ACM quadrangular mesh. It is worth noting

that the FEniCS simulations were not executed in parallel, which would undoubtedly further boost their performance in a future scenario.

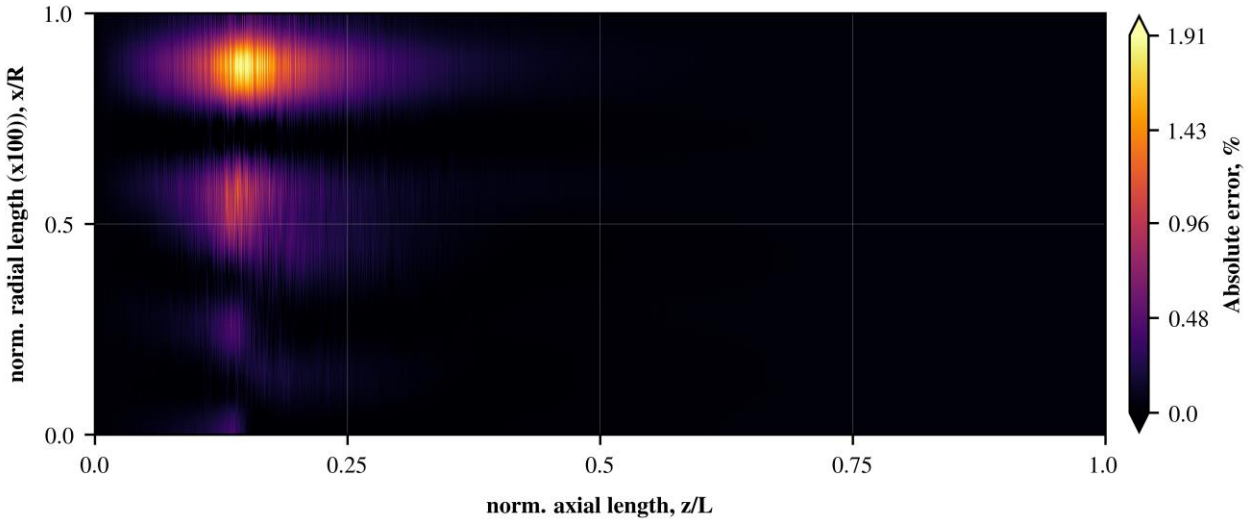

Figure 2-4. Absolute error for the FEniCS and ACM contrasted thermal maps.

2.4.2 Case study 2 – SNG synthesis

The aforementioned mathematical model in Section 2.3.4.2 was solved exclusively with the proposed computational toolbox due to the large number of equations involved. Therefore, the FEniCS results were solely compared with the literature, where most studies address thermal performance aspects as an inherent feature of CO_2 methanation. The subsequent sections present and discuss the results obtained on the formation of hot spots and overall CO_2 conversion as part of the last stage in the already described workflow (refer to Section 2.3.3).

2.4.2.1 CO_2 methanation and reactor hot spots

The heat generated by an exothermic reaction within a fixed-bed reactor operating at a constant wall temperature may eventually overcome the heat removal rate of the cooling jacket, inevitably increasing the temperature in a particular region on what is called a hot spot. The transient evolution of the temperature profile during hot spot formation in the reaction channel is used not only to explain the phenomenon itself, but also to illustrate a dynamic visualization example of the mentioned toolbox components (see Figure 2-1).

Figure 2-5 displays the typical thermal map evolution of the packed bed when precise conditions for the Sabatier reaction ignition are given (see caption), ending with hot spot formation. At the beginning, the reactor is heated due to the difference between the wall and the feed gas temperatures (~ t_1). This prior heating makes it easier for the reactants to overcome the kinetic limitations to initiate the methane production. In turn, the advance of the reaction produces

additional energy that ultimately leads the system to exceed the wall temperature, at which time the cooling jacket starts removing heat (~ t_2).

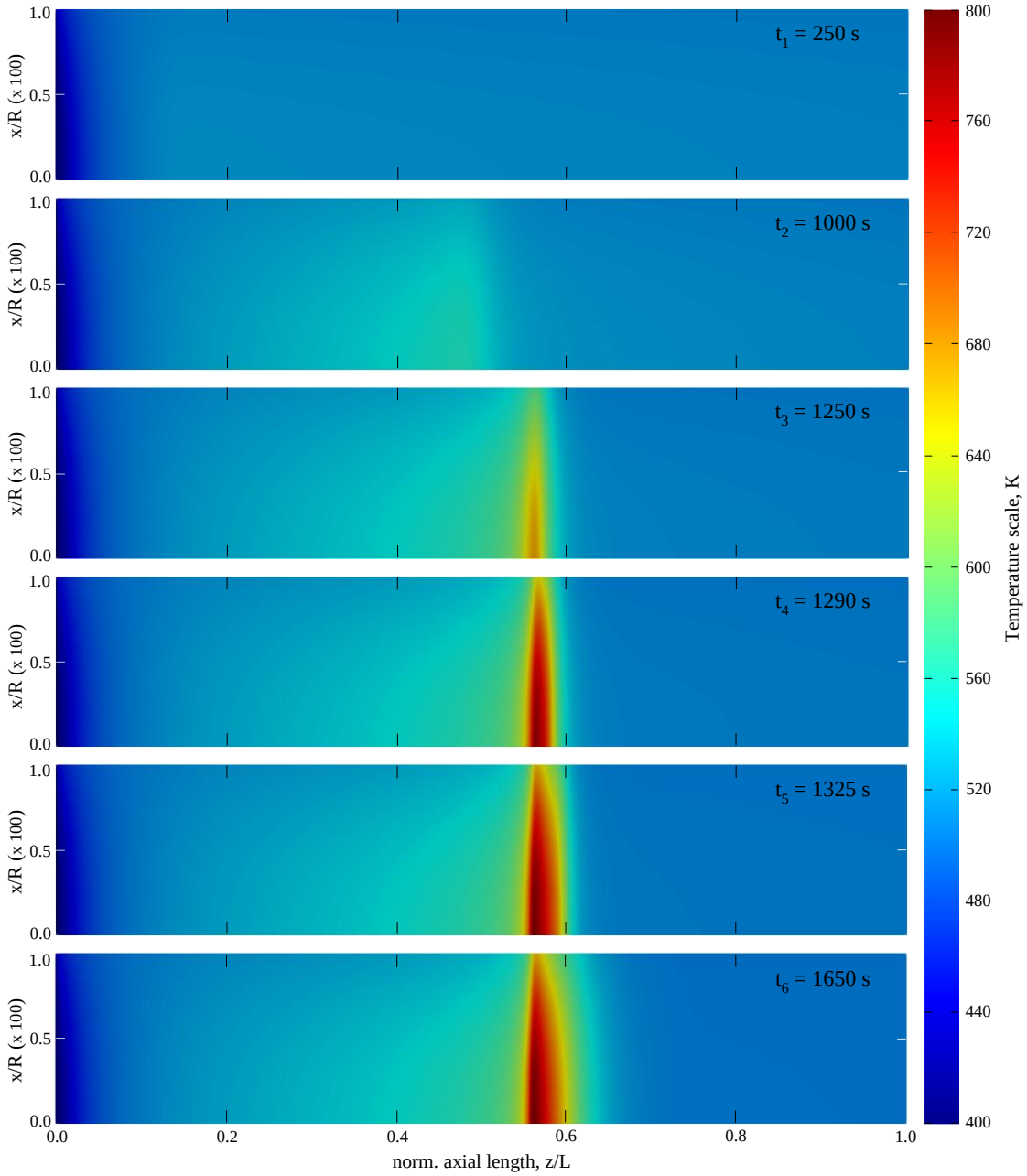

Figure 2-5. Bed temperature contours along the x-z plane in a single tube of the methanation tube bundle reactor (made with ParaView) from the reactor start-up (t_1=250 s) until the steady state (t_6=1650 s). This simulation took place with a reactor feed temperature, pressure, gas velocity, and H_2:CO_2 molar ratio of 400 K, 5 bar, 1 m/s, and 4.8, respectively. In addition, the coolant temperature settled at a constant temperature of 500 K.

However, the exponential reaction rate temperature dependence leads the reactants to an ignition state that makes cooling of the jacket insufficient, forming a hot spot up to a length of approximately 2.8 m ($z/L = 0.56$), for this example. The increase in the hot spot's max-temperature is only slowed down by the almost total consumption of the reagents or the emergence of thermodynamic limitations. This indissoluble relationship between temperature and conversion along the fixed-bed reactor is shown in Figure 2-6. Finally, after approximately 1650 s of operation (~ t_6), the system reaches a steady state.

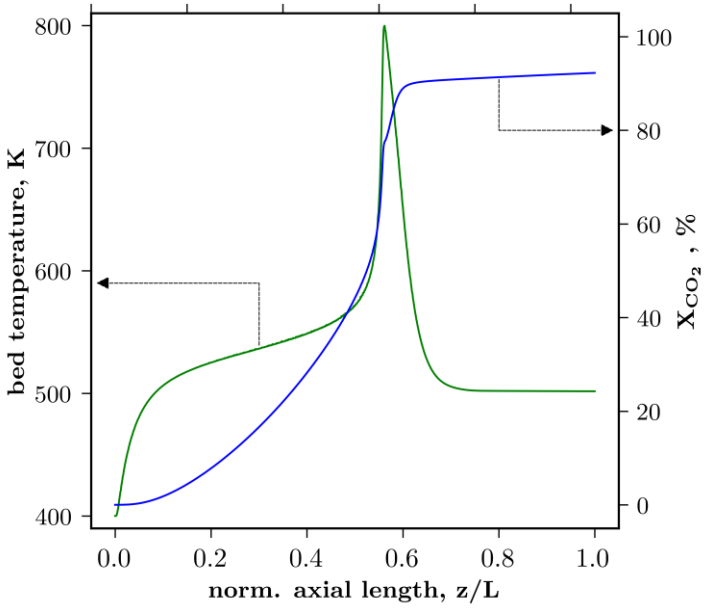

Figure 2-6. CO_2 conversion and packed-bed temperature profiles along the reactor length (r = 0) at a steady-state (t_6) for the simulation are displayed in Figure 2-5.

2.4.2.2 Parametric study variables

One way to validate the results computed by FEniCS and examine the modelled system is to conduct a parametric study. This analysis provides information on the system's sensitivity, whose consistency is discussed, and allows us to establish a correlation with that reported so far. In addition, data analysis from simulations in the parametric study provides feedback to restate the variational problem if reliable results are not entirely achieved and until they are, as indicated in Figure 2-1.

On this basis, variations in the coolant temperature, inlet gas velocity, feed reactant ratio, and inlet pressure are included. All of them stand as critical process variables that may be subject to unintended load changes or are otherwise operational adjustment variables. To choose the variation range for each critical variable, thermodynamic and kinetic aspects were considered, as well as literature on relevant industrial conditions. Accordingly, all the simulations were run by feeding

an undiluted gas mixture of H_2/CO_2 at 400 K as the inlet temperature, whereas the lower and upper range limits for the rest of the process variables are stated in Table 2-7. For each analysis, one parameter was exclusively ranged within the stipulated limits, while the others remained constant at their respective standard value. The simulations were executed until the system reached a quasi-stationary state (~1000 s depending on the settled conditions).

Table 2-7. Summary of critical variables and their operating limits within the CO_2 methanation reactor.

Process variable	Lower	Upper	Standard	Unit
Coolant temperature	300	530	500	K
Inlet gas velocity	0.5	2	1	m/s
H_2/CO_2 molar ratio	3:1	7:1	4:1	-
Inlet gas pressure	1	10	5	bar

In the parametric assessment, two key features were assessed: CO_2 conversion and temperature axial distribution. In the case of ignition, the hot spot location, maximum temperature and runaway temperature were discussed. Otherwise, the reaction is said to be either extinguished (overcooled) or just restrained for distinct reasons. Moreover, two targets were established for the bed temperature and CO_2 conversion: for the former, a maximum limit of 775 K, assuming catalyst deactivation [35], [36], and for the latter, a tentative minimum CO_2 conversion of 90 %, although it may vary depending on the regional energy quality policies. The conversion for any species was defined as stated in Eq. (2.23).

$$X_i = 100 \cdot \left[\left(F_i|_f - \lfloor \sum_j F_i \rfloor_{z/L=1} \right) \Big/ F_i|_f \right] \tag{2.23}$$

Although the conversion and bed temperature are generally evaluated as output characteristics, a strictly quantitative correlation with the reported characteristics is rather tricky due to the simultaneous convergence of multiple factors, such as the reactor/cooling system design, the catalytic model employed, and the operating conditions. Notwithstanding, typical patterns derived from the Sabatier reaction thermodynamics were identified and contrasted with the detailed study on methanation thermodynamics developed by Gao et al., (2012). Further quantitative correlations could be established with the analysis conducted by Bremer and Sundmacher (2019) and Zimmermann et al. (2020), given the existence of shared parameters and conditions, whereas qualitative trends could be outlined looking at that recorded elsewhere (refer to Table 2-1). From here on, the results of the parametric study are presented with pertinent discussions and correlations.

2.4.2.2.1 Effect of the coolant temperature

First, the parametric sensitivity concerning the cooling temperature was investigated. Figure 2-7(a) shows that the increase in the cooling temperature favours the conversion of CO_2, where conversions close to equilibrium are reached at coolant temperatures above 500 K. This profile shows a fast ignition curve between 495-500 K caused by the exponential dependence of the reaction rate on the temperature. The results demonstrate how sensitive the reaction system is to the wall (coolant) temperature.

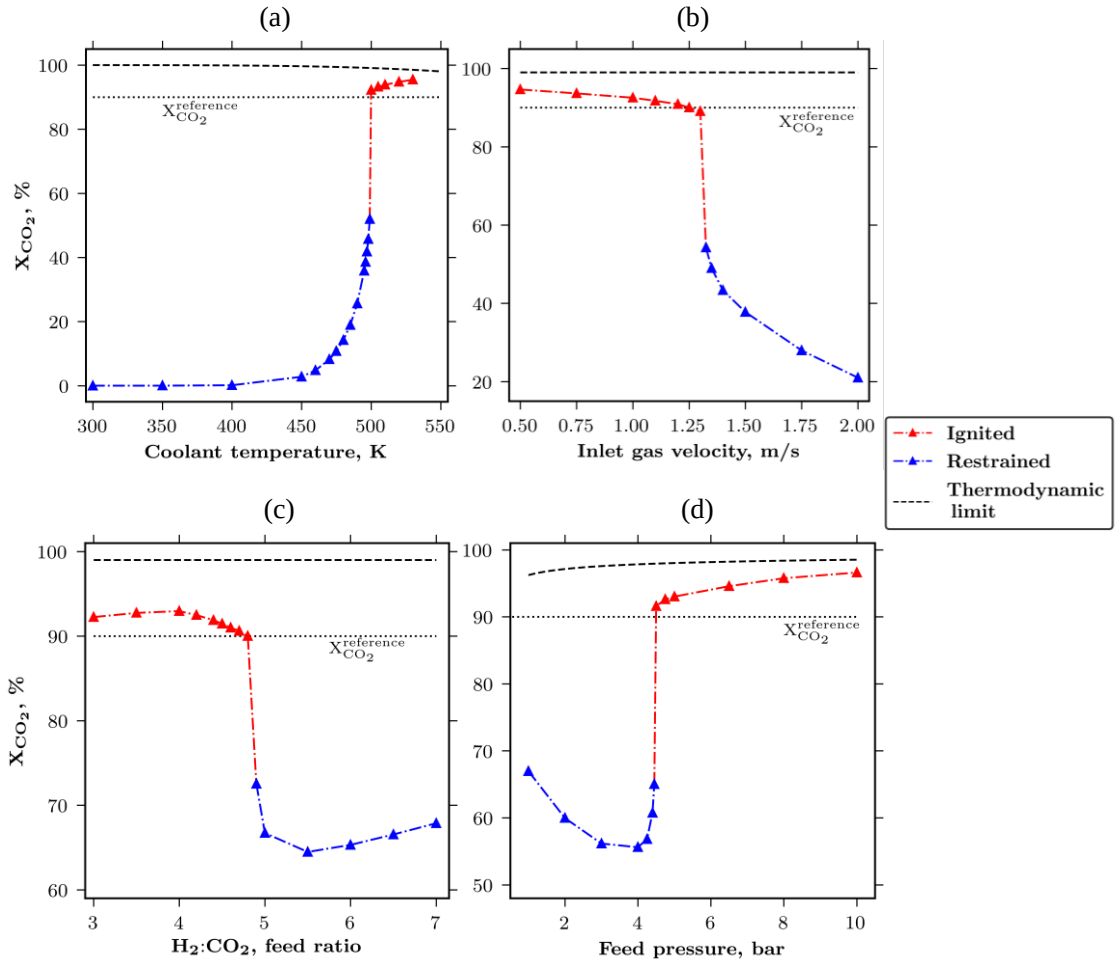

Figure 2-7. Parametric sensitivity analysis on CO_2 conversion. (a) Effect of the coolant temperature, (b) inlet gas velocity, (c) CO_2:H_2 molar ratio, and (d) feed pressure.

The observed parametric sensitivity is not only due to methanation exothermicity, but also to the high activity of the employed catalyst, as described in the kinetic expression of Koschany et al. (2016). Indeed, this characteristic has also been reported by other studies using the same model [36], [40], [41], [43]. Two of them were in fixed-bed reactors, while the remaining were in microstructured reactors. Regarding the former, Bremer and Sundmacher (2019) found an ignition

temperature of approximately 465 K, while Zimmermann et al. (2020) reported one up to 515 K. Regardless, it always resulted in CO_2 conversion near the equilibrium curve.

Furthermore, hot spot formation in terms of location and maximum temperature was also investigated. Figure 2-8(a) shows the bed temperature profile along the reactor normalized length for distinct coolant values. For coolant temperatures between 300 and 490 K (Figure 2-8(a-bottom)), the system is forced by heat transfer to reach the boundary (wall) temperature at some point, without any deviation. In contrast, for the range of 490 to 495 K, a slight bed temperature increment can be appreciated due to low heat accumulation.

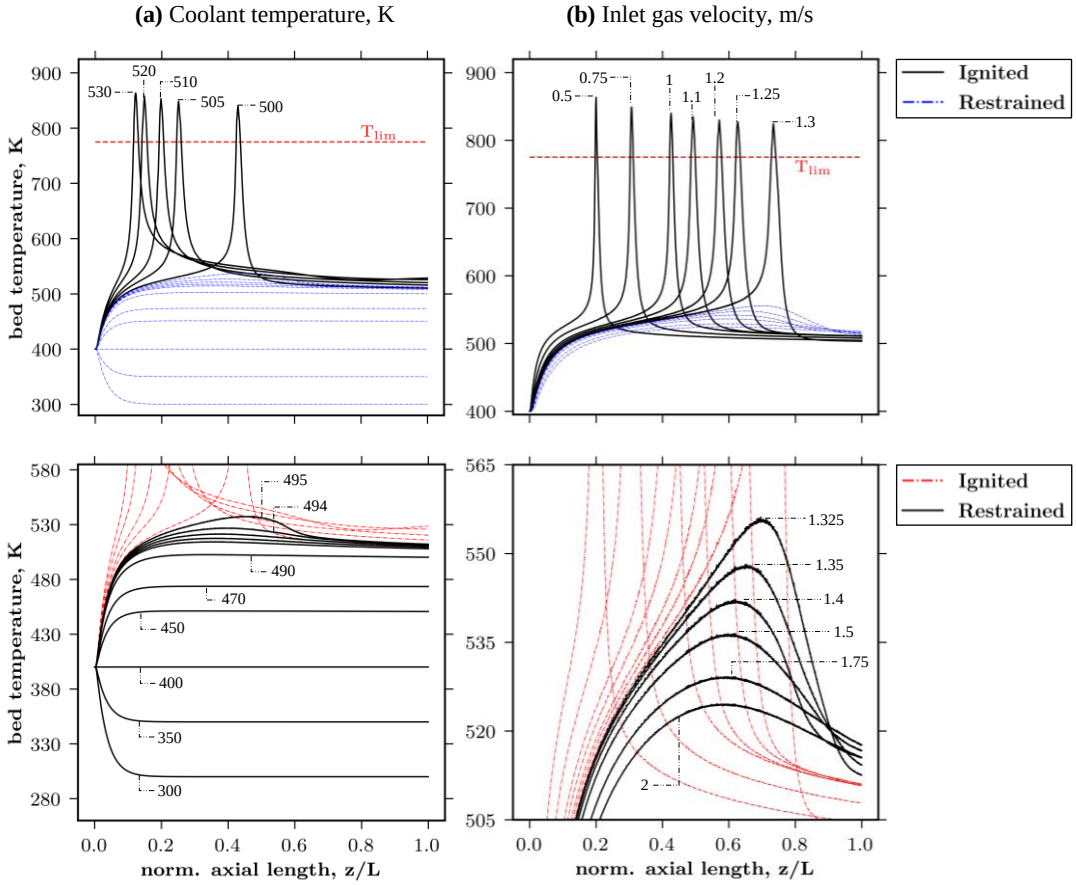

Figure 2-8. Parametric sensitivity analysis of (a) coolant temperature and (b) inlet gas velocity on the hot spot formation. Black and continuous sharp peaks (top) indicate the presence of hot spots due to ignition conditions, while zoomed continuous black curves (bottom) call for overcooling.

Last, values equal to or greater than 500 K generate sharp peaks (hot spots) above the established limit target of 775 K, as shown in Figure 2-8(a-top). For this range, the increase in the wall temperature not only produces a tiny increment in the hot spot maximum temperature but also shows a peak location shift towards the reactor inlet. The precise hot spot position is difficult to

validate, but its maximum temperature has been found in the range of 800 to 900 K when using the same catalytic model and reactor type [36], [40]. Moreover, using a different kinetic model, a parametric study by Schlereth and Hinrichsen (2014) showed a similar trend when evaluating coolant temperature, despite the maximum temperatures exceeding 900 K for that operating case.

2.4.2.2.2 Effect of the inlet gas velocity

Determining the reactor performance under distinct inlet gas velocities is crucial. This parameter might be subjected to load changes in the P2M context or purposely manipulated to adjust the reactor throughput and the process profitability. Figure 2-7(b) shows that inlet gas velocities below 1.3 m/s (GHSV = 1560 h^{-1}) result in CO_2 conversions of ~90 % or above, all of which are ignition points. However, slight gains from 1.3 m/s (e.g., 1.325 m/s - GHSV = 1590 h^{-1}) decrease the CO_2 conversions down to ~55 % and beyond to conversions of 20 % for velocities of 2 m/s (GHSV = 2400 h^{-1}).

With the same catalytic model, Zimmermann et al. (2020) reported an equivalent parametric sensitivity for values of ~1 m/s. Deviations shall be related to calculating the transport resistances. In that operating case, a heterogeneous modelling approach was used, rather than the simplified fixed effectiveness factor herein. In addition, using different kinetics, Sun and Simakov (2017) and Sun et al. (2017) exhibited a similar sensitivity for GHSV ranging from 1000-5000 h^{-1}.

Moreover, Figure 2-8(b) shows the temperature profile along the packed bed for different inlet gas velocities. For velocities ≥ 1.325 m/s, there is a small increase in the maximum bed temperature relative to the coolant temperature (500 K), although this delta remains below ~56 K. In contrast, for lower velocities the presence of steep peaks is evidence of the formation of hot spots. These peaks differ in location and height, which is ascribed to multiple residence times. Decreasing the inlet gas velocity augments the contact/residence time of the reacting flow with the catalyst and diminishes the convective heat transfer, leading to eventual hot spot formation, as would be expected. The observed maximum temperature under the runaway condition is in good agreement with that noticed by Zimmermann et al. (2020) at approximately 840 K.

2.4.2.2.3 Effect of the CO_2:H_2 molar ratio

In this case, the H_2:CO_2 feed molar ratio was ranged to investigate its effect on CO_2 conversion and hot spot formation from operation start-up. The reagent ratio at the reactor entrance is a critical variable that is likely to undergo fluctuations considering the supply chain in P2M (namely, renewable-powered electrolysis and biogas plants). One way to interpret this variable is to assume a change in the volumetric flow of the reactants supplied separately, maintaining the overall velocity once the mixture is formed.

Figure 2-7(c) shows a maximum CO_2 conversion (~ 93 %) for an H_2:CO_2 molar ratio of 4 and the highest parametric sensitivity for molar ratios of approximately 4.9 ± 0.01. The minimum conversion (~ 64 %) corresponds to a molar ratio of ~ 5.5, with an increase from that value onwards (up to ~ 67 %) until 7:1. In addition, the bed temperature in the centreline surpasses the wall temperature for all ratios, as shown in Figure 2-9(a). Values < 4.9 are ignition points for the reaction (top), and the opposite is true for molar ratios ≥ 4.9.

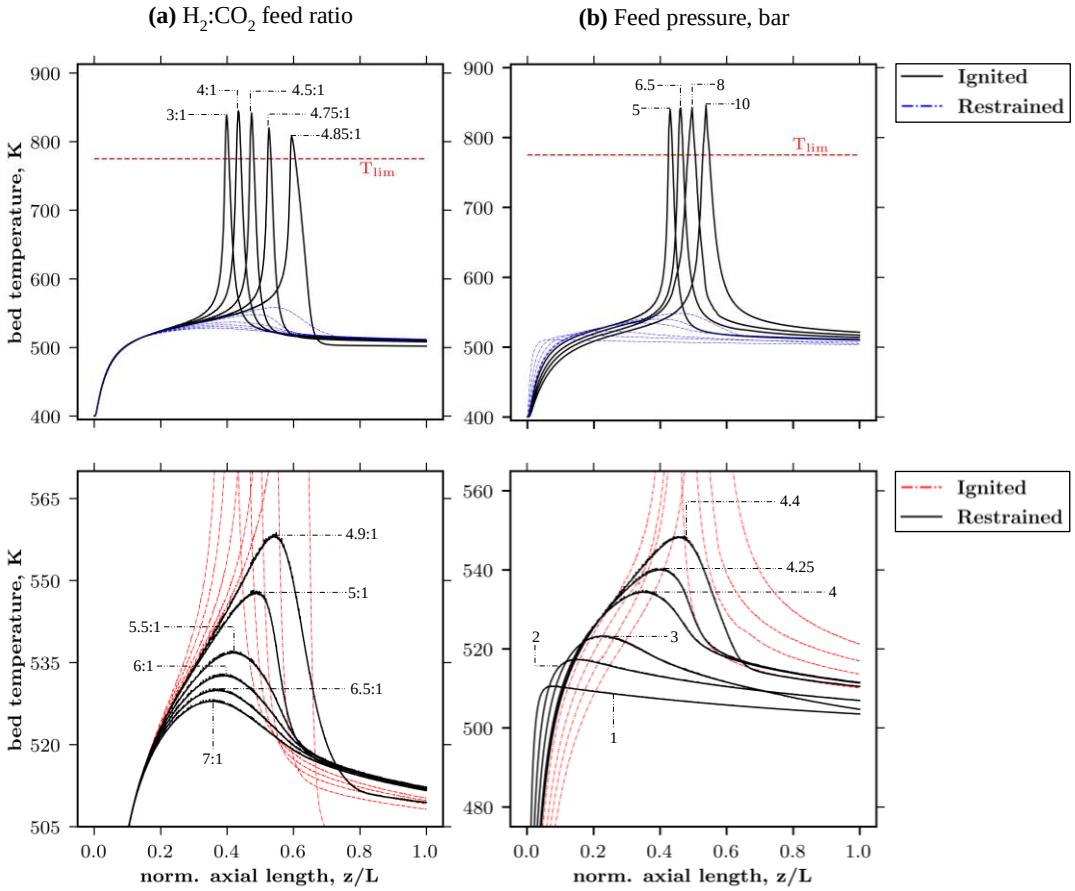

Figure 2-9. Parametric sensitivity analysis of (a) the feed reagent ratio and (b) pressure on hot spot formation. Black and continuous sharp peaks (top) indicate the presence of hot spots due to ignition conditions, while zoomed continuous black curves (bottom) call for overcooling.

The effect of the H_2:CO_2 molar ratio on the system is complicated due to the combined interaction of multiple variables, which depend on the gas composition. This effect is outlined for selected variables in the Supplementary Material. Herein, the effective reaction rate was singled as the main rate. The kinetic model by Koschany et al. (2016) shows a maximum rate near a ratio of 4, which may explain the highest conversion achieved under that condition shown in Figure 2-7(c). However, this is not consistent with the mere thermodynamic study performed by Gao et al. (2012), in which CO_2 conversions increase with the H_2:CO_2 molar ratio up to a value of 6:1. Nevertheless,

contrary to the thermodynamic arguments, Kreitz et al. (2019b) also evidenced an inverse relationship between the conversion-molar ratio.

Note that the effective reaction rate is susceptible to other factors outside the gas composition (e.g., temperature, pressure), which suffer multiple variations during dynamic operation and hinder the analysis. The available information about the effect of the molar ratio is fairly nil from a kinetic rather than a thermodynamic perspective. Therefore, additional parametric studies on this variable should be developed to further explore its dynamic effect on reactor performance at the industrial level, beyond the picture outlined here.

2.4.2.2.4 Effect of the feed pressure

Figure 2-7(d) shows a complex behaviour concerning the reactor feed pressure and its effect on CO_2 conversion. At low pressures (< ~4.4 bar), CO_2 is negatively affected. One reason is that the increase in pressure is associated with an extended injection of reactants, with insufficient conditions to heat the mixture towards an ignition level, and the residence time does not allow for conversions above 70%. Nevertheless, there is an inflection point at approximately 4.4 bar, at which the amount of heat released ignites the system long enough, thus triggering CO_2 conversion. This last circumstance is coupled with the thermodynamic nature of methanation, in which the reaction rate is promoted with absolute pressure. This trend is due to the CO_2 methanation volume reducing behaviour [73].

The favouring of pressure in the reaction rate is typical of methanation and has been broadly demonstrated elsewhere [46]–[48], [50], regardless of the operation case. Furthermore, a quantitative comparison can be established with the parametric analysis conducted by Zimmermann et al. (2020) with acceptable agreement; as observed in Figure 2-7(d), the same inflection point at 4 bar with conversions between 50-60% and an ignition pressure near 5 bar resulting in CO_2 conversions above 90% were reported therein.

On the other hand, Figure 2-9(b) shows that feed pressures of 5 bar or above result in ignition states. A slight increment in the maximum hot spot temperature is also observed as the runaway pressure increases. This tendency is ascribed to a higher heat generation relative to an enlarged volume of reagents, which triggers chemical kinetics and raises the bed temperature until the reagents are consumed. The maximum hot spot temperatures are approximately 800-850 K, reasserting the results reported by Zimmermann et al. (2020).

As final remarks, the formation of hot spots is highly susceptible to the investigated inlet process variables (namely, coolant temperature, gas velocity, reagent ratio, and pressure) and is a decisive factor in the attained overall CO_2 conversion. The kinetic component of the reaction rate was observed to prevail over its thermodynamic nature. In any case, for safety reasons an operation

should avoid conditions of pronounced parametric sensitivity. Last, the computational toolbox brings a smooth FEM implementation to numerically solve systems of PDEs commonly found in the mathematical modelling of chemical reactors and allows flexible post-simulation data manipulation, enabling, for example, the interpretation of the previously discussed parametric study.

2.5 Conclusions

In this contribution, a computational toolbox composed of open-source FEniCS and complementary components was employed for the first time in order to solve two case studies in the chemical and process engineering field. Phthalic anhydride production was used as a validation case study, in which the results of FEniCS were contrasted with ACM software. Indeed, an absolute error of up to 2% was recorded after comparing these computational tools. On the other hand, the computational toolbox was used to solve a mathematical model that describes CO_2 methanation in a multi-tubular fixed-bed reactor for industrial P2M applications. The simulations covered an operating window for critical process variables through a parametric study, in which hot spot formation and overall CO_2 conversion were chosen as the response variables. From the analysis, ignition/runaway conditions and the ranges of high parametric sensitivity that should be avoided during reactor operation were identified. The consistency of the results was discussed and compared both qualitatively and quantitatively to varying degrees with those reported so far. The results were reasonable and in harmony with the existing literature, which validates not only the model, but also the reliability of the computational toolbox within a research scenario.

Therefore, FEniCS does serve as a functional computational tool in the chemical and process engineering fields. This toolbox is open-source and gives accurate results, judging by the comparison made with trusted ACM software and the reports in prior research. Hence, it eases access to the scientific and industrial community to address engineering problems. Finally, the application extension of the computational tools exposed above in even more diverse and complex chemical engineering problems is encouraged and required to further test it.

2.6 Nomenclature and abbreviations.

Latin letters		**Subscripts**	
u	Trial function, [−]	i	Chemical species: {C_8H_{10}, O_2, $C_8H_4O_3$, H_2O, CO_2, H_2, CH_4}
v	Test function, [−]		
f	Source term, [−]	j	Mesh node index
F	Variational formulation, [−]	k	Summation index
n	Mesh node, [−]	z	In axial direction
x	Radial coordinate, [m]	ini	Initial in$t$
z	Axial coordinate, [m]	oxy	o-xylene oxidation reaction

t	Time, [s]
R	Reactor radius, [m]
L	Reactor length, [m]
V	Reactor volume, [m3]
A	Area, [m^2]
C	Concentration, [mol m^{-3}]
p	Pressure, [bar]
T	Temperature, [K]
X	Chemical conversion, [1]
$\vec{\vartheta}$	Fluid velocity vector, [m s^{-1}]
D	Diffusion coefficient, [m^2 s^{-1}]
C_p	Specific heat capacity, [J kg^{-1} K^{-1}]
F	Mass flow, [kg/s]
U	Heat transfer coefficient, [W m^{-2} K^{-1}]
d_p	Particle diameter, [m]
e	Emissivity Coefficient, [1]
M	Molar mass, [g mol^{-1}]
v	Stoichiometrically coefficient, [1]
r	Reaction rate, [various]
K_{eq}	Equilibrium constant, [bar^{-2}]
k	Reaction kinetic coefficient, [mol bar^{-1} s^{-1} $g_{cat}{}^{-1}$]
E_A	Activation energy, [kJ mol^{-1}]
$K_{.x}$	Adsorption rate coefficient, [$bar^{-0.5}$]
ΔH_X	Adsorption enthalpy change, [kJ mol^{-1}]
R	Universal gas constant, [various]

Greek letters

Ω	Mathematical domain, [−]
$\partial\Omega$	Domain boundaries, [−]
ρ	Density, [g m^{-3}] || [kg m^{-3}]
λ	Thermal conductivity, [W m^{-1} K^{-1}]
λ_{rs}	Parameter in the computation of λ, [W m^{-1} K^{-1}]
μ	Fluid dynamic viscosity, [Pa s]
ω	Special atomic diffusion volume, [1]
$\Delta_R H$	Reaction enthalpy, [J mol^{-1}]
ε	Catalyst bed porosity, [1]
η	Catalyst effectiveness factor, [1]

Sab	Sabatier reaction (CO_2 methanation)
$cool$	Coolant
gas	Gas phase (mixture)
cat	Catalyst phase
ref	Reference
Tref	Given at the ref temperature
f	Feed
w	Wall
b	Bulk
T	Formulation for T equation
p	Formulation for p equation

Superscripts

eff	Effective
$intr$	Intrinsic
m	Mixture
n/ n+1	Time index or counter
$FEniCS$	Solution computed by FEniCS
ACM	Solution computed by ACM

Abbreviations

GHG	Green House Gas
P2M	Power-to-Methane
SNG	Synthetic Natural Gas
LHHW	Langmuir-Hinshelwood-Hougen-Watson
GHSV	Gas Hourly Space Velocity
ACM	Aspen Custom Modeler
MGMP	Mesh Generation and Mesh Processing
HPC	High Performance Computing
API	Application Programming Interface
PDEs	Partial Differential Equation(s)
BCs	Boundary Condition(s)
P1	Lagrange polynomials family
FEM	Finite Element Method
FVM	Finite Volume Method
NDFs	Numerical Differential Function(s)
BFD1	1st-order Backward Finite Differences
MOL	Method of Lines

ς	Unit conversion factor, [various]	OCFE3	3rd-order Orthogonal Collocation on Finite Elements
δ	Percentage absolute error, [1]	CV	Coefficient of Variation
α,β	Kinetic parameters, [various]		

[−] refers to without units and [1] to dimensionless units.

2.7 Acknowledgements

The authors gratefully acknowledge Universidad de La Sabana for financial support through project ING-208-2018 and the Colombia Scientific Program's funding support within the *Ecosistema Científico* framework (Contract No. FP44842- 218e2018). Santiago Ortiz also acknowledges Universidad de La Sabana for the Teaching Assistant Scholarship for his master's studies. The authors are also grateful to the FEniCS community for the technical support provided during the learning curve covered for the proper management of the computational toolbox (this work has no official association with the FEniCS Project). Lastly, D.Sc. Nestor Sánchez is acknowledged for his assistance during the writing.

2.8 References − Chapter 2

[1] B. Gustafsson, *Fundamentals of Scientific Computing*, vol. 8. Berlin, Heidelberg: Springer Berlin Heidelberg, 2011.
[2] J. H. Ferziger and M. Perić, *Computational Methods for Fluid Dynamics*, vol. 3. Berlin, Heidelberg: Springer Berlin Heidelberg, 2002.
[3] A. Logg, K.-A. Mardal, G. N. Wells, and others, *Automated Solution of Differential Equations by the Finite Element Method*. Springer, 2012.
[4] M. S. Alnæs *et al.*, "The FEniCS Project Version 1.5," *Arch. Numer. Softw.*, vol. 3, no. 100, 2015.
[5] A. Logg and G. N. Wells, "DOLFIN: Automated Finite Element Computing," *ACM Trans. Math. Softw.*, vol. 37, no. 2, 2010.
[6] C. Geuzaine and J.-F. Remacle, "Gmsh: A 3-D finite element mesh generator with built-in pre- and post-processing facilities," *Int. J. Numer. Methods Eng.*, vol. 79, no. 11, pp. 1309–1331, Sep. 2009.
[7] U. Ayachit, *The ParaView Guide: A Parallel Visualization Application*. 2015.
[8] J. Ahrens, B. Geveci, and C. Law, *ParaView: An End-User Tool for Large Data Visualization*. Elsevier Inc., 2005.
[9] Q. Zhu and J. Yan, "A moving-domain CFD solver in FEniCS with applications to tidal turbine simulations in turbulent flows," *Comput. Math. with Appl.*, no. xxxx, Aug. 2019.
[10] R. Haagenson, H. Rajaram, and J. Allen, "A generalized poroelastic model using FEniCS with insights into the Noordbergum effect," *Comput. Geosci.*, vol. 135, no. July 2019, p. 104399, Feb. 2020.
[11] A. Janečka, J. Málek, V. Průša, and G. Tierra, "Numerical scheme for simulation of transient flows of non-Newtonian fluids characterised by a non-monotone relation between the symmetric part of the velocity gradient and the Cauchy stress tensor," *Acta Mech.*, vol. 230, no. 3, pp. 729–747, Mar. 2019.
[12] S. W. Funke, M. Nordaas, Ø. Evju, M. S. Alnæs, and K. A. Mardal, "Variational data assimilation for transient blood flow simulations: Cerebral aneurysms as an illustrative example," *Int. j. numer.*

method. biomed. eng., vol. 35, no. 1, p. e3152, 2019.
[13] R. Murray and G. Young, "Neutral competition in a deterministically changing environment: Revisiting continuum approaches," *J. Theor. Biol.*, vol. 486, p. 110104, Feb. 2020.
[14] B. E. Abali, "An Accurate Finite Element Method for the Numerical Solution of Isothermal and Incompressible Flow of Viscous Fluid," *Fluids*, vol. 4, no. 1, p. 5, Jan. 2019.
[15] V. Phunpeng and P. M. Baiz, "Mixed finite element formulations for strain-gradient elasticity problems using the FEniCS environment," *Finite Elem. Anal. Des.*, vol. 96, no. C, pp. 23–40, Apr. 2015.
[16] T. Epanchintsev, S. Pravdin, A. Sozykin, and V. Zverev, "Parallel Simulation of Scroll Wave Dynamics in the Human Heart Using the FEniCS Framework," *Procedia Comput. Sci.*, vol. 101, pp. 68–75, 2016.
[17] K. Goodwin *et al.*, "Smooth muscle differentiation shapes domain branches during mouse lung development," *Development*, vol. 146, no. 22, 2019.
[18] E. Lejeune, "Mechanical MNIST: A benchmark dataset for mechanical metamodels," *Extrem. Mech. Lett.*, vol. 36, p. 100659, Apr. 2020.
[19] B. E. Abali, *Computational Reality*, vol. 55. Singapore: Springer Singapore, 2017.
[20] H. Bünger, "Ullmann's Encyclopedia of Industrial Chemistry, Vol. A9: Dithio-carbamic Acid and Derivates to Ethanol. VCH Verlagsgesellschaft, Weinheim – Deerfield Beach – Basel 1987. XV, 653 S., Subskriptionspreis DM 375,–; endgült. Preis DM 465,–," *Chemie Ing. Tech.*, vol. 60, no. 8, p. 638, Aug. 1988.
[21] M. P. Gimeno, J. Gascón, C. Téllez, J. Herguido, and M. Menéndez, "Selective oxidation of o-xylene to phthalic anhydride over V2O5/TiO2: Kinetic study in a fluidized bed reactor," *Chem. Eng. Process. Process Intensif.*, vol. 47, no. 9–10, pp. 1844–1852, 2008.
[22] P. H. Calderbank, K. Chandrasekharan, and C. Fumagalli, "The prediction of the performance of packed-bed catalytic reactors in the air-oxidation of o-xylene," *Chem. Eng. Sci.*, vol. 32, no. 12, pp. 1435–1443, 1977.
[23] J. N. Papageorgiou, M. C. Abello, and G. F. Froment, "Kinetic modeling of the catalytic oxidation of o- xylene over an industrial V2O5-TiO2 (anatase) catalyst," *Appl. Catal. A, Gen.*, vol. 120, no. 1, pp. 17–43, 1994.
[24] D. Vanhove and M. Blanchard, "Catalytic oxidation of o-xylene," *J. Catal.*, vol. 36, no. 1, pp. 6–10, 1975.
[25] C. R. Dias, M. F. Portela, and G. C. Bond, "Oxidation of o-Xylene to Phthalic Anhydride over V2O5/TiO2 Catalysts," *J. Catal.*, vol. 157, no. 2, pp. 353–358, Dec. 1995.
[26] J. Herten and G. F. Froment, "Kinetics and product distribution in the oxidation of o-xylene on a vanadium pentoxide catalyst," *Ind. Eng. Chem. Process Des. Dev.*, vol. 7, no. 4, pp. 516–526, 1968.
[27] J. Skrzypek, M. Grzesik, M. Galantowicz, and J. Soliński, "Kinetics of the catalytic air oxidation of o-xylene over a commercial V2O5-TiO2 catalyst," *Chem. Eng. Sci.*, vol. 40, no. 4, pp. 611–620, 1985.
[28] G. F. Froment, K. B. Bischoff, and J. De Wilde, *Chemical reactor analysis and design*. New York: Wiley, 1990.
[29] M. Oh and C. C. Pantelides, "A modelling and simulation language for combined lumped and distributed parameter systems," *Comput. Chem. Eng.*, vol. 20, no. 6–7, pp. 611–633, Jun. 1996.
[30] Aspen Technology Inc., "Aspen Custom Modeler V9." 2016.
[31] K. Ghaib and F.-Z. Ben-Fares, "Power-to-Methane: A state-of-the-art review," *Renew. Sustain. Energy Rev.*, vol. 81, no. June 2017, pp. 433–446, Jan. 2018.
[32] W. Wang, S. Wang, X. Ma, and J. Gong, "Recent advances in catalytic hydrogenation of carbon dioxide," *Chem. Soc. Rev.*, vol. 40, no. 7, pp. 3703–3727, 2011.
[33] K. Ghaib, K. Nitz, and F.-Z. Ben-Fares, "Chemical Methanation of CO 2 : A Review," *ChemBioEng Rev.*, vol. 3, no. 6, pp. 266–275, Dec. 2016.

[34] M. Götz *et al.*, "Renewable Power-to-Gas: A technological and economic review," *Renew. Energy*, vol. 85, pp. 1371–1390, Jan. 2016.
[35] S. Rönsch *et al.*, "Review on methanation - From fundamentals to current projects," *Fuel*, vol. 166, pp. 276–296, 2016.
[36] R. T. Zimmermann, J. Bremer, and K. Sundmacher, "Optimal catalyst particle design for flexible fixed-bed CO2 methanation reactors," *Chem. Eng. J.*, vol. 387, no. July 2019, p. 123704, May 2020.
[37] S. Farsi, W. Olbrich, P. Pfeifer, and R. Dittmeyer, "A consecutive methanation scheme for conversion of CO2 – A study on Ni3Fe catalyst in a short-contact time micro packed bed reactor," *Chem. Eng. J.*, vol. 388, no. February, p. 124233, May 2020.
[38] J. Lefebvre, S. Bajohr, and T. Kolb, "Modeling of the transient behavior of a slurry bubble column reactor for CO2 methanation, and comparison with a tube bundle reactor," *Renew. Energy*, vol. 151, pp. 118–136, May 2020.
[39] C. Jia, Y. Dai, Y. Yang, and J. W. Chew, "A fluidized-bed model for NiMgW-catalyzed CO2 methanation," *Particuology*, vol. 49, pp. 55–64, Apr. 2020.
[40] J. Bremer and K. Sundmacher, "Operation range extension via hot-spot control for catalytic CO 2 methanation reactors," *React. Chem. Eng.*, vol. 4, no. 6, pp. 1019–1037, 2019.
[41] B. Kreitz, G. D. Wehinger, and T. Turek, "Dynamic simulation of the CO2 methanation in a micro-structured fixed-bed reactor," *Chem. Eng. Sci.*, vol. 195, pp. 541–552, Feb. 2019.
[42] F. Vidal Vázquez, J. Kihlman, A. Mylvaganam, P. Simell, M.-L. Koskinen-Soivi, and V. Alopaeus, "Modeling of nickel-based hydrotalcite catalyst coated on heat exchanger reactors for CO2 methanation," *Chem. Eng. J.*, vol. 349, no. April, pp. 694–707, Oct. 2018.
[43] M. Gruber *et al.*, "Modeling and Design of a Catalytic Wall Reactor for the Methanation of Carbon Dioxide," *Chemie-Ingenieur-Technik*, vol. 90, no. 5, pp. 615–624, 2018.
[44] K. H. G. Rätze, J. Bremer, L. T. Biegler, and K. Sundmacher, *Physics-Based Surrogate Models for Optimal Control of a CO2 Methanation Reactor*, vol. 40. Elsevier Masson SAS, 2017.
[45] J. Bremer, K. H. G. Rätze, and K. Sundmacher, "CO 2 methanation: Optimal start-up control of a fixed-bed reactor for power-to-gas applications," *AIChE J.*, vol. 63, no. 1, pp. 23–31, Jan. 2017.
[46] N. Engelbrecht, S. Chiuta, R. C. Everson, H. W. J. P. Neomagus, and D. G. Bessarabov, "Experimentation and CFD modelling of a microchannel reactor for carbon dioxide methanation," *Chem. Eng. J.*, vol. 313, pp. 847–857, Apr. 2017.
[47] J. Ducamp, A. Bengaouer, and P. Baurens, "Modelling and experimental validation of a CO 2 methanation annular cooled fixed-bed reactor exchanger," *Can. J. Chem. Eng.*, vol. 95, no. 2, pp. 241–252, Feb. 2017.
[48] D. Sun and D. S. A. Simakov, "Thermal management of a Sabatier reactor for CO2 conversion into CH4: Simulation-based analysis," *J. CO2 Util.*, vol. 21, no. June, pp. 368–382, Oct. 2017.
[49] D. Sun, F. M. Khan, and D. S. A. Simakov, "Heat removal and catalyst deactivation in a Sabatier reactor for chemical fixation of CO 2 : Simulation-based analysis," *Chem. Eng. J.*, vol. 329, pp. 165–177, Dec. 2017.
[50] R. Y. Chein, W. Y. Chen, and C. T. Yu, "Numerical simulation of carbon dioxide methanation reaction for synthetic natural gas production in fixed-bed reactors," *J. Nat. Gas Sci. Eng.*, vol. 29, pp. 243–251, Feb. 2016.
[51] D. Schlereth and O. Hinrichsen, "A fixed-bed reactor modeling study on the methanation of CO2," *Chem. Eng. Res. Des.*, vol. 92, no. 4, pp. 702–712, Apr. 2014.
[52] Y. Liu and O. Hinrichsen, "CFD Simulation of Hydrodynamics and Methanation Reactions in a Fluidized-Bed Reactor for the Production of Synthetic Natural Gas," *Ind. Eng. Chem. Res.*, vol. 53, no. 22, pp. 9348–9356, Jun. 2014.
[53] J. Andersson, "A General-Purpose Software Framework for Dynamic Optimization (Een algemene softwareomgeving voor dynamische optimalisatie)." 2013.
[54] W. Spencer Smith, D. Adam Lazzarato, and J. Carette, "State of the practice for mesh generation

and mesh processing software," *Adv. Eng. Softw.*, vol. 100, pp. 53–71, Oct. 2016.
[55] The CGAL Project, *CGAL User and Reference Manual*, 5.0.2 ed. CGAL Editorial Board, 2020.
[56] P. Cignoni, M. Callieri, M. Corsini, M. Dellepiane, F. Ganovelli, and G. Ranzuglia, "MeshLab: an Open-Source Mesh Processing Tool," in *Eurographics Italian Chapter Conference*, 2008.
[57] H. Si, "TetGen: A quality tetrahedral mesh generator and a 3D Delaunay triangulator," *URL http//tetgen. berlios.*, no. 13, p. vii + 97, 2013.
[58] The OpenFOAM Foundation, "OpenFOAM: User Guide v1219." 2019.
[59] N. Schlömer *et al.*, "nschloe/pygmsh v6.1.1." Zenodo, Apr-2020.
[60] H. Petter Langtangen and A. Logg, *Solving PDEs in Python-The FEniCS Tutorial Volume I*, vol. I. Springer, 2017.
[61] J. J. Camata, V. Silva, P. Valduriez, M. Mattoso, and A. L. G. A. Coutinho, "In situ visualization and data analysis for turbidity currents simulation," *Comput. Geosci.*, vol. 110, no. May 2017, pp. 23–31, 2018.
[62] N. Schlömer *et al.*, "nschloe/meshio v4.0.9," Mar. 2020.
[63] J. Soumagne and J. Biddiscombe, "Computational steering and parallel online monitoring using RMA through the HDF5 DSM virtual file driver," *Procedia Comput. Sci.*, vol. 4, pp. 479–488, 2011.
[64] S. Herbein, S. McDaniel, N. Podhorszki, J. Logan, S. Klasky, and M. Taufer, "Performance characterization of irregular I/O at the extreme scale," *Parallel Comput.*, vol. 51, pp. 17–36, 2016.
[65] M. Musy, G. Dalmasso, and B. Sullivan, "marcomusy/vtkplotter: vtkplotter." Zenodo, Feb-2019.
[66] M. Musy *et al.*, "marcomusy/vedo: 2020.4.1." Zenodo, Oct-2020.
[67] G. F. Froment, K. B. Bischoff, and J. De Wilde, *Chemical reactor analysis and design*, 3rd ed. New York: Wiley, 2011.
[68] A. El Sibai, L. Rihko-Struckmann, and K. Sundmacher, *Synthetic Methane from CO2: Dynamic Optimization of the Sabatier Process for Power-to-Gas Applications*, vol. 37, no. June. Elsevier, 2015.
[69] G. Eigenberger and W. Ruppel, "Catalytic Fixed-Bed Reactors," in *Ullmann's Encyclopedia of Industrial Chemistry*, Weinheim, Germany: Wiley-VCH Verlag GmbH & Co. KGaA, 2012.
[70] VDI, *VDI Heat Atlas*. Berlin, Heidelberg: Springer Berlin Heidelberg, 2010.
[71] B. Kreitz, J. Friedland, R. Güttel, G. D. Wehinger, and T. Turek, "Dynamic Methanation of CO 2 – Effect of Concentration Forcing," *Chemie-Ingenieur-Technik*, vol. 91, no. 5, pp. 576–582, 2019.
[72] F. Koschany, D. Schlereth, and O. Hinrichsen, "On the kinetics of the methanation of carbon dioxide on coprecipitated NiAl(O)<inf>x</inf>," *Appl. Catal. B Environ.*, vol. 181, pp. 504–516, 2016.
[73] J. Gao *et al.*, "A thermodynamic analysis of methanation reactions of carbon oxides for the production of synthetic natural gas," *RSC Adv.*, vol. 2, no. 6, p. 2358, 2012.
[74] D. S. A. Simakov and M. Sheintuch, "Model-based optimization of hydrogen generation by methane steam reforming in autothermal packed-bed membrane reformer," *AIChE J.*, vol. 57, no. 2, pp. 525–541, Feb. 2011.
[75] M. H. Wesenberg and H. F. Svendsen, "Mass and Heat Transfer Limitations in a Heterogeneous Model of a Gas-Heated Steam Reformer," *Ind. Eng. Chem. Res.*, vol. 46, no. 3, pp. 667–676, Jan. 2007

CHAPTER 3: CFD-aided conceptual design of an intensified reactor for the production of synthetic natural gas within the power-to-methane context

This chapter aims to propose a reactor conceptual design to produce SNG in the PtM context following an intensification strategy to overcome the shortcomings of conventional reactors discussed in Chapter 2 (above). The design is based on a heat-exchanger reactor comprising staked-plates with a reaction network of parallel wall-coated channels. The design was constrained by the achievement of near isothermal conditions, low-pressure drops and a product dry-basis quality that would enable the system to be ultimately integrated with the natural gas grid.

CFD-aided conceptual design of an intensified reactor for the production of synthetic natural gas within the power-to-methane context

Santiago Ortiz-Laverde[a], Camilo Rengifo [b], Martha Cobo [a], Manuel Figueredo [a,] *

[a] Energy, Materials and Environment Laboratory, Department of Chemical Engineering, Universidad de La Sabana, Campus Universitario Puente del Común, Km. 7 Autopista Norte, Bogotá, Colombia

[b] Department of Mathematics, Physics and Statistics, Universidad de La Sabana, Campus Universitario Puente del Común, Km. 7 Autopista Norte, Bogotá, Colombia.

* Corresponding author. Email: manuel.figueredo@unisabana.edu.co

3.1 Abstract

The spread of renewable sources within the energy market has boosted the emerging Power-to-Methane (PtM) concept as an attractive strategy for the transport and storage of surplus power into Synthetic Natural Gas (SNG) using several CO_2 sources. The challenges represented by the PtM context have encouraged the development of reaction technologies adequately adapted to its demands. This contribution provides a CFD simulation-aided conceptual design of a heat-exchanger wall-coated reactor for the SNG production using an intensification approach. The design is based on a reactor formed by single-pass stacked-plates comprising a reacting network of multiple parallel channels. In the first stage of design, an individual reacting channel including the catalytic layer thickness is dimensioned to fulfil a minimum SNG quality given by the CO_2 conversion ($\geq$ 95%), maximizing throughput. In the second stage, the stacked-plates manifold geometry and dimensions that best promote a uniform distribution in flow rate are established as a function of the number of reacting channels. In the last step, the results are merged and validated by means of larger scale simulations, in which replication of the single-channel design point is achieved for a full reactor stacked plate. The proposed conceptual design sets a blueprint for future design of intensified reactors and overcomes the shortcomings of conventional reactors used for PtM applications.

Keywords: CFD-aided Design, Power-to-Methane, Process Intensification, Heat-exchanger Wall-coated Reactor

3.2 Introduction

Fossil fuels have propelled the progress and technological evolution of the last two centuries, with a series of environmental implications proven over the last three decades [2]. The current development plans now include sustainable policies based on low- or non-carbon footprint technologies, most based on renewable sources. Even so, there are limitations that prevent these initiatives from competitively outperforming fossil fuels, such as their inability to maintain a supply-base load synchronized with the power demand and their weather-dependent nature (i.e., wind flow and solar irradiation), resulting in undesirable strong temporal fluctuations [3], [4].

The proposal with perhaps major acceptance to overcome the barrier mentioned above is the intermediate chemical storage of surplus energy through the so-called Power-to-Gas (PtG) concept [5]. According to this notion, the electrical energy otherwise wasted is transformed into chemical fuels, in which an electrolysis process to produce hydrogen (H_2) is always the first step. Indeed, H_2 is a clean and valuable energy carrier. However, it has severe technical limitations related to its storage and transport [4], [6]. One proposed solution is to convert H_2 into fuels, such as methane (CH_4), with broader supply chains using the existing infrastructure. This conversion is a long-term form of energy storage and transport known as the Power-to-Methane concept (PtM) [7], [8].

Accordingly, the synthesis of CH_4 from H_2 requires a carbon source, which situates the PtM concept within the Carbon Capture and Utilization (CCU) technologies [9]. The chemical route for the synthesis of CH_4 from CO_2 and H_2, namely Synthetic Natural Gas (SNG), is a catalytic reaction known as methanation or Sabatier reaction (Eq. (3.1)).

$$CO_2 + 4H_2 \Leftrightarrow CH_4 + 2H_2O \ , \qquad (\Delta_R H^{298\ \mathrm{K}} = -164.9\ \mathrm{kJ\ mol^{-1}}). \tag{3.1}$$

PtM has already proven to be a technically realizable technology. The environmental, technical and economic feasibility of PtM applications in combination with various carbon sources (i.e., off-gas, biogas and gasification syngas) has been recorded [4], [5], [10], [11]. An example in the industrial scenario is the Audi e-gas Project in operation since 2013, with a total capacity of 6 MW [12], [13]. The target is always to have a safe and efficient operation while guaranteeing the desired product quality. However, these goals may be somewhat conflicting when dealing with an exothermic system as the Sabatier reaction. This issue is particularly noticeable in fixed bed reactors which have evidenced their deficiency to manage the released heat from the highly exothermic Sabatier reaction, exacerbated by the presence of transfer resistances [14]–[21]. The conducted studies have concluded that it is infeasible to carry out the CO_2 methanation in industrial-scale fixed-bed reactors at high CO_2 conversions (> 90%) and under undiluted conditions without showing a runaway behaviour. The resulting hot-spots formation is undesirable

because of its contribution to catalyst deactivation, yet fixed-bed is the reaction technology most widely used commercially for PtM applications [5], [8], [11], [13].

Furthermore, the implementation of alternative reaction technologies has also been investigated. Microchannel, structured, fluidized bed, heat exchanger and slurry bubble column reactors are the most relevant types of reactors proposed for the PtM concept [22], [23], [32], [24]–[31]. The idea behind some of the mentioned alternatives is to intensify the mass and energy transport processes, which allows, among others, to reduce the temperature gradient. Consequently, the typical formation of hot spots in CO_2 methanation can be avoided, allowing a higher-temperature-level operation while assuring the desired SNG quality. In this matter, microreaction technologies have proven to be superior [33]–[35].

Microreaction technology is the result of a Process Intensification (PI) strategy, as an innovation of the chemical process industry. PI has been transformed into a rapidly growing field of research and industrial development to modify conventional chemical processes into more efficient and safer processes [34]. The intensification is aimed to adjust the characteristic parameters defined by the geometry, always resulting in a surface-to-volume enlarger ratio [36]–[38]. The reduction of transport distances by appropriately shaping the geometry improves heat- and mass-transfer rates. Further, the compaction or miniaturization of a unit operation must be applied to at least one system dimensions [34].

Therefore, the current PI trend consists of designing more efficient devices in terms of enhanced reaction control, process safety, energy consumption, operating expenses and environmental impact [36], [39]–[41]. Moreover, there are advantages when scaling-up units in the PI context over the conventional procedure. The so-called numbering-up is the proposed approach for intensified processes, in which the number of parallel operating units is increased without changing their single dimensions (i.e., reacting channel miniaturized geometry) [42], [43]. Since the redesigning process can be avoided, the latter approach turns out to be faster than the typical pilot-industrial plant scale-up [39]. However, even with numbering-up, the throughput of an intensified process might be insufficient to meet the expected industrial demand. Hence, a central question that often comes up is to what extent should the device be intensified as a commitment to process productivity (?) [34], [39].

Intensified devices are generally considered to be in the micrometric scale when at least one of their dimensions is under 1000 μm. Below this scale, it has been demonstrated that there are no substantial changes in yield, while the opposite is true for dimensions above 1 mm [44]. Nevertheless, reducing the characteristic dimensions down to the millimetre range (1 mm – 1 cm) is sometimes solely sufficient since the surface-to-volume augmented ratio is still in force. Besides, some of the commonly reported downsides of microreaction technologies such as high pressure-

drop, channel blocking, and uneven flow rates can be prevented on a millireactor scale [37]. Hence, in some cases, miniaturization down to the millimetre scale is even a better trade-off than the use of microstructured equipment [34], [39].

Despite the potential benefits of PI in PtM applications, the literature is still limited. Brooks et al. demonstrated the performance of a microchannel heat-exchanger unit with the Sabatier reaction, aimed at outer space operations and assisted by a one-dimensional plug-flow model [45]. Engelbrecht et al. studied relevant steady-state operating conditions in a microchannel reactor with a single-channel modelling approach [23]. Kreitz et al. investigated the fluctuating effect of inlet compositions on the output of a micro-structured fixed-bed reactor through a comprehensive dynamic one-dimensional analysis [26]. Indeed, the latter work was based on a design discussed by Gruber et al. for the Sabatier reaction with the evaluation of few structural parameters [24]. Further, Farsi et al. conducted tests on a micro packed-bed reactor, focusing on catalytic development research by proposing a novel rate model for Ni_3Fe [28]. The main focus of the relatively scarce literature has been on the evaluation of steady-state and dynamic operating conditions based on formerly established micro-structured designs or the development of new catalysts. Therefore, the PI concept may be explored deeply in the PtM applications context.

The proposal of a Computer-Aided Design (CAD) for an intensified methanation reactor is the aim of this paper. The conceptual design is supported by Computational Fluid Dynamics (CFD) simulations of the heterogeneous catalytic reaction and free-fluid domains. Recent examples of this nature for intensified systems but distinct processes can be found elsewhere [46], [47]. The PI concept is applied to the reactor structural evaluation beyond the micrometric scale, looking for better trade-offs in the millimetre range. The design attempts to avoid the hot spots formation, attaining a minimum of SNG quality under relevant PtM operating conditions. To the best of our knowledge, a CFD-aided design of this kind has not been considered so far for PtM applications.

3.3 Methods

3.3.1 Design overview

The dimensioned reaction technology is a heat-exchanger wall-coated system, as depicted in Figure 3-1. The reactor comprises single-pass stacked plates, each holding a network of parallel semi-circular reaction channels coated with a catalytic layer. The plates are arranged interleaved between cooling and reacting flow in a counter-current way. Feed-gas is injected into the inlet manifold of each stacked plate and then goes to the parallel channels where the reaction occurs due to catalytic effects and operating conditions. The syngas is collected in the outlet manifold of each plate and leaves the reactor through a duct.

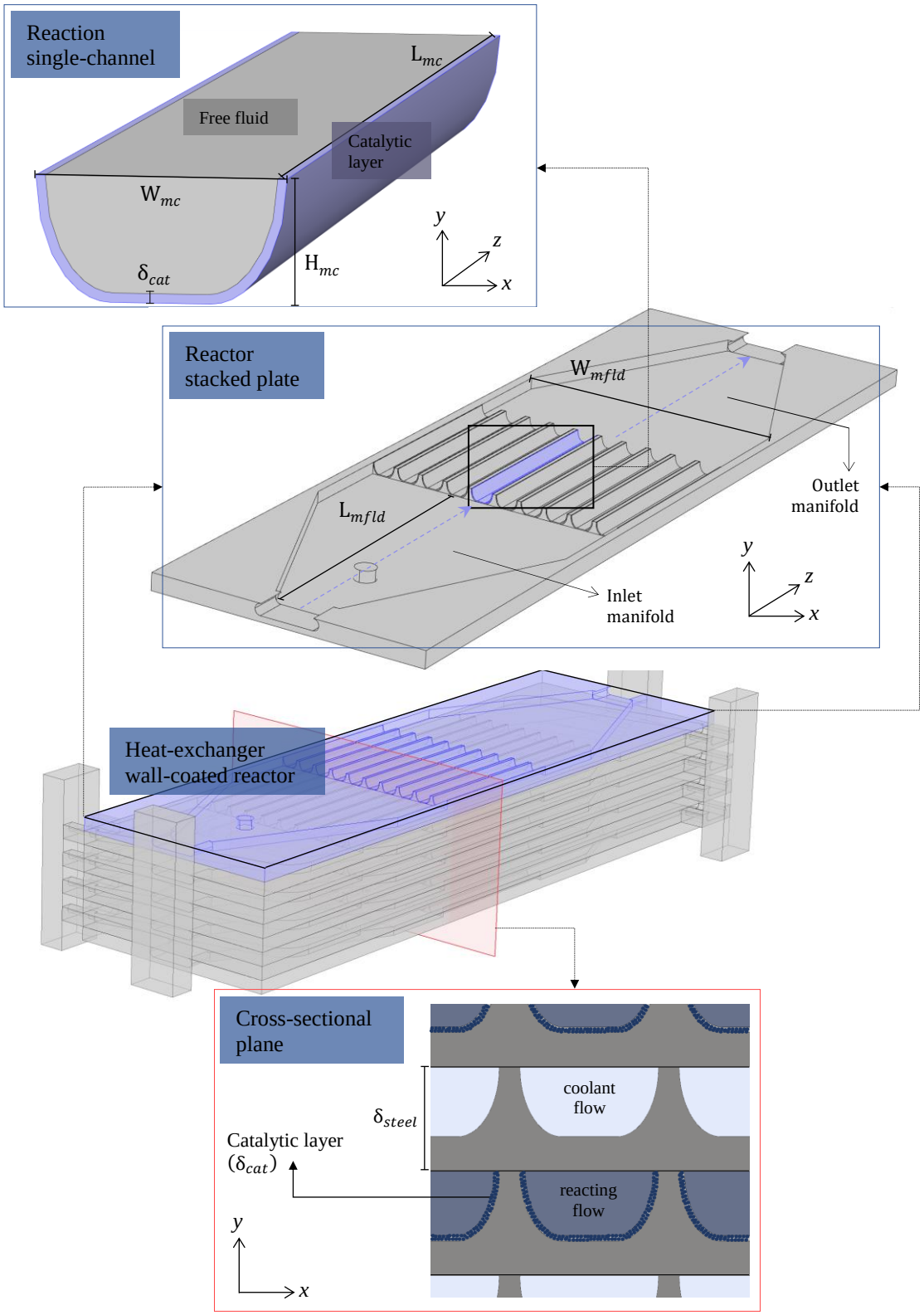

Figure 3-1. Sketch of the heat-exchanger wall-coated reactor.

The design process is carried out in three stages: (1) the three-dimensional (3-D) structural dimensioning of an individual reaction channel, including the catalytic layer thickness; (2) the two-dimensional (2-D) design of the distribution/collection manifolds as a function of the number of reaction channels and according to the design point selected in stage 1; (3) a set of 3-D simulations merging the optimum results of previous design stages, discussing the effect of reaction channel elongation on system performance. The governing criteria along the design process are the quality of the produced SNG, the reactor throughput and the uniformity of flow distribution over the inlet manifold.

In this work, the multiphysics problem of fluid flow, transport of concentrated species, chemical reaction and heat transfer are coupled and solved using the commercial software COMSOL Multiphysics V5.6. The performed simulations established the best structural dimensions within the evaluated micro-to-millimetre scale and under PtM relevant industrial conditions. The developed design may be considered conceptual since it does not include an economic or manufacturing cost assessment. Further details on the phenomenological model and design parametrisation are described in the following sections.

3.3.2 Reactor and kinetic modelling

The design involves three stages, and the mathematical modelling is subjected to different assumptions in each of them, as explained later on. Nevertheless, in this section, the governing equations, boundary conditions and reaction rate model are displayed for the system as a whole. The nomenclature and abbreviations used throughout the paper are listed at the end of Chapter 3 (Section 3.6) for ease of reading.

3.3.2.1 Governing equations, model assumptions, and boundary conditions

Two domains converge mathematically and physically throughout the reactor. There are two coexisting gas and solid phases in one domain, while only the gas phase remains in the other. The former refers to the reaction flow and porous wall-coated layer where the Sabatier reaction occurs, whereas the latter comprises the regions where the gas flows freely without coming into contact with the fixed catalyst. In both domains, the phenomenology is expressed through a three-dimensional Partial Differential Equations (PDEs) system that includes momentum, energy, and mass transport with chemical reaction. The set of mathematical PDEs for each domain is presented separately without ignoring that both must be coupled at the free-fluid and porous media interface. The porous media and free fluid region governing equations are summarized in Table 3-1 and Table 3-2, respectively.

The catalytic wall-coated layer is modelled as a pseudo-homogenous porous media where the catalytic layer morphological properties (porosity and permeability) are assumed constant. The heat and mass dispersion (i.e., back-mixing) within the porous media are incorporated using two

properties, the effective binary diffusion (D_{α}^{eff}) and thermal conductivity (λ^{eff}). The former is computed according to [48], [49] as a temperature- and pressure-dependent function, involving a tortuosity factor correction via Bruggeman correlation based on sphere packing. Regarding the effective thermal conductivity, an average relation is implemented via Eqs. (3.2)-(3.3).

$$\lambda^{eff} = \Theta\lambda_{cat} + (1-\Theta)\lambda_{gas} \tag{3.2}$$

$$\Theta = (1-\varepsilon) \tag{3.3}$$

The thermal conductivity of the gas is taken from [50], while the catalyst conductivity and porosity are assumed constant according to [51] and [26]. See Appendix B (below) for further details.

To forecast the governing momentum transport within the wall-coated catalytic layer, the Brinkman-Forchheimer extended Darcy equation is solved along with mass- and heat- transfer equations. Herein, the permeability is estimated based on the Kozeny-Carman equation as a function of the particle diameter and porosity. The fluid flow is assumed compressible with a Mach number (Ma) above 30 % of sound speed.

Table 3-1. Summary of governing equations for the wall-coated catalytic layer.

Description	Mathematical expression	Eq.
Species continuity equation	$\rho\,(\mathbf{u}\cdot\nabla)w_{\alpha} + \nabla\cdot\mathbf{j}_{\alpha} = (1-\varepsilon)\mathrm{M}_{\alpha}v_{\alpha,\,Sab}\mathrm{R}_{Sab}$, $\mathbf{j}_{\alpha} = -\rho\, D_{\alpha}^{eff}\nabla w_{\alpha}$.	(3.4)
Energy equation	$\rho C_p\mathbf{u}\cdot\nabla T + \nabla\cdot\mathbf{q} = (1-\varepsilon)\left(-\Delta_{\mathrm{R}}H_{\mathrm{Sab}}\right)\mathrm{R}_{Sab}$, $\mathbf{q} = -\lambda^{eff}(\nabla T)$.	(3.5)
Brinkman-Forchheimer extended Darcy equation	$\rho\frac{1}{\varepsilon}(\mathbf{u}\cdot\nabla)\frac{1}{\varepsilon}\mathbf{u} = \nabla\cdot[-p\mathbf{I}+\mathbf{K}] - \frac{\mu}{\mathrm{k}}\mathbf{u}$, $\mathbf{K} = \mu\frac{1}{\varepsilon}(\nabla\mathbf{u} + (\nabla\mathbf{u})^{\mathrm{T}}) - \frac{2}{3}\mu\frac{1}{\varepsilon}(\nabla\cdot\mathbf{u})\mathbf{I}$.	(3.6)
Continuity equation	$\nabla\cdot(\rho\mathbf{u}) = 0$.	(3.7)

Also, the multicomponent gas mixture was assumed to follow an ideal gas behaviour.

$$\rho = \frac{p}{\mathrm{R}\,T}\sum_{\alpha} y_{\alpha}\mathrm{M}_{\alpha} \tag{3.8}$$

$$C_p = \sum_{\alpha}\left(\frac{\rho_{\alpha}}{\rho}C_{p_{\alpha}}\right) \tag{3.9}$$

On the other hand, the free-fluid domain is fully homogeneous, where any gas-phase reactions are negligible. Accordingly, the governing equations given in Table 3-2 describe the mass, energy, and momentum transport phenomena without reacting source terms. Herein the Navier-Stokes momentum equation expressed by Eq. (3.12) is computed along the free and non-reacting fluid region.

Table 3-2. Summary of governing equations for the free fluid region.

Description	Mathematical expression	Eq.
Species continuity equation	$\rho\,(\mathbf{u}\cdot\nabla)w_{\alpha} + \nabla\cdot\mathbf{j}_{\alpha} = 0$, $\mathbf{j}_{\alpha} = -\rho\, D_{\alpha}^{\mathrm{m}}\nabla w_{\alpha}$.	(3.10)
Energy equation	$\rho C_p\mathbf{u}\cdot\nabla T + \nabla\cdot\mathbf{q} = 0$, $\mathbf{q} = -\lambda(\nabla T)$.	(3.11)
Navier-Stokes equation	$\rho(\mathbf{u}\cdot\nabla)\mathbf{u} = \nabla\cdot[-p\mathbf{I} + \mathbf{K}]$, $\mathbf{K} = \mu(\nabla\mathbf{u} + (\nabla\mathbf{u})^{\mathrm{T}}) - \frac{2}{3}\mu(\nabla\cdot\mathbf{u})\mathbf{I}$.	(3.12)
Continuity equation	$\nabla\cdot(\rho\mathbf{u}) = 0$.	(3.13)

The boundary conditions are given in Table 3-3, being characterized as:

i. Fixed temperature and mass concentrations at the inlet given by Dirichlet boundary conditions.
ii. Fully developed flow for temperature and mass concentrations at the outlet boundary with backflow suppression for the velocity.
iii. No-slip (nil velocity) at the reactor walls according to the Knudsen dimensionless number (Kn < 0.001), threshold value below which the continuity statement is valid, and so the employed momentum transport equations.
iv. Convective heat flux at the walls due to heat exchange.

Table 3-3. Summary of boundary conditions for the transport phenomena governing equations.

Description	Mathematical expression	Eq.
Species continuity equation	$w_\alpha = w_{\alpha,\mathrm{f}}$ on $\Gamma_{z=0}$, $-\mathbf{n}\cdot\mathbf{j}_\alpha = 0$ on $\Gamma_{z=L}$, $-\mathbf{n}\cdot\rho D_\alpha^{\mathrm{m}}\nabla w_\alpha = 0$ on Γ_r .	(3.14)
Energy equation	$T = T_{\mathrm{f}}$ on $\Gamma_{z=0}$, $-\mathbf{n}\cdot\mathbf{q} = 0$ on $\Gamma_{z=L}$, $-\mathbf{n}\cdot\mathbf{q} = \mathrm{U_A}(T_{\mathrm{cool}} - T)$ on Γ_r .	(3.15)
Navier-Stokes equation	$\int_{\partial\Omega}\rho(\mathbf{u}\cdot\mathbf{n})\,\mathrm{ds} = \dot{m}$ on $\Gamma_{z=0}$, $[-p\mathbf{I}+\mathbf{K}]\mathbf{n} = -\mathbf{n}\,\hat{p}_{\mathrm{ref}}$, $\hat{p}_{\mathrm{ref}} \le p_{\mathrm{ref}}$ on $\Gamma_{z=L}$. $\mathbf{u} = 0$ on Γ_r ,	(3.16)

Γ_r refer to the channel walls boundary

The term $\mathrm{U_A}$ is the heat transfer coefficient for the wall boundaries. A rigorous calculation of this factor is critical in the accurate forecasting of heat removal from the reacting network towards the coolant plate. The model is based on the fashion suggested elsewhere [16] but adapted for the present work's reactor design scheme, as shown in Figure 3-1. Stainless-steel (German grade SS314) was selected as the most suitable heat-resistance material, given the operating conditions and the fact that it has been used in previous reactor designs with similar characteristics [23], [52]. The properties for the coolant (thermal oil) and the metal region are taken from [53].

The several layers involved in the energy transport process between the reaction and coolant channels are considered to estimate the heat transfer coefficient. This estimation includes the reacting flow (γ_{free}), the wall-coated catalytic layer (γ_w), the metallic wall region (κ_{wall}), and the coolant fluid (γ_{cool}). In the convective heat-transfer model, two types of boundaries are settled for the sake of completeness. The reaction channel upper boundary (without catalytic layer) presents different transport features compared to the catalytic layer in the semi-circular area. In the latter one, the heat-transfer resistances are stronger. Eqs. (3.17 – 3.18) accounts for the heat-transfer

coefficients at the upper and catalytic layer boundaries, respectively. Both the coolant and reacting flows are assumed to be hydrodynamically and thermally in development.

$$\frac{1}{\mathrm{U_A}} = \frac{1}{\gamma_{\mathrm{free}}\left(\frac{\mathrm{H}_{mc}}{2} - \delta_{cat}\right)} + \frac{1}{\gamma_w\left(\frac{\mathrm{H}_{mc}}{2}\right)} + \frac{1}{\kappa_{wall}} + \frac{1}{\gamma_{\mathrm{cool}}\left(\frac{\mathrm{H}_{mc}}{2} + \delta_{wall}\right)} \tag{3.17}$$

$$\frac{1}{\mathrm{U_A}} = \frac{1}{\gamma_{\mathrm{free}}\left(\frac{\mathrm{H}_{mc}}{2}\right)} + \frac{1}{\kappa_{wall}} + \frac{1}{\gamma_{\mathrm{cool}}\left(\frac{\mathrm{H}_{mc}}{2} + \delta_{wall}\right)} \tag{3.18}$$

Further details on the calculation sequence can be found in Appendix B (below).

3.3.2.2 Catalyst diffusion limitations

The reaction rate is not exempt from transport limitations. There are two types of resistances in the wall-coated reactor. The first one is related to the transport from within the free-fluid region towards the catalytic layer, while the second one has to do with the gas flow inside the catalytic layer, where interphase and intra-particle resistances (namely external and internal) can occur. The first type of resistance is accounted for by the mathematical model through the diffusion or dispersion coefficient via Eq. (3.4). Meanwhile, the second is considered through an effectiveness factor that multiplies the intrinsic reaction rate.

$$\mathrm{R}_{Sab} = \eta\, \rho_{cat}\, \mathrm{r}^{\,\mathrm{int}}_{Sab} \tag{3.19}$$

The interphase limitations are generally neglected in the effectiveness factor calculation due to high superficial gas velocities [18], [54]. The latter does not apply to intraparticle mass- and energy-transfer resistances, which are typically considered due to the particle size and reaction exothermicity. Nevertheless, in the current design, the catalytic layer comprises particles ranging from 5 to 50 μm, a scale that does not present limitations to the mass and energy transfer despite the operating conditions (550 K, 8 bar). As discussed later, the predominant resistance is the diffusion from the fluid bulk towards the porous medium as a function of the wall-coated layer thickness.

3.3.2.3 Catalytic rate

The Sabatier reaction may occur together with the endothermic Reverse Water Gas Shift (RWGS) and exothermic CO methanation reactions. Nevertheless, it has been shown that the latter two might be negligible at typical CO_2 methanation conditions due to the low amount of CO produced at temperatures below 750 K [16], [26], [51], [55]. As a result, this study relies on the state-of-the-art kinetic model proposed by Koschany et al. (2016) to describe the CO_2 methanation reaction

rate. This kinetic model was proposed for $NiAl(O)_x$ and evaluated under industrial relevant conditions. The adopted Langmuir-Hinshelwood-Hougen-Watson rate model is expressed by Eqs. (3.24 – 3.25):

$$r_{Sab}^{int} = k(T)\, p_{H_2}^{0.5} p_{CO_2}^{0.5} \left(1 - \frac{p_{CH_4} p_{H_2O}^{2}}{p_{CO_2} p_{H_2}^{4} K_{eq}(T)}\right) \Big/ \text{DEN} \tag{3.24}$$

$$\text{DEN} = 1 + K_{OH}(T)\frac{p_{H_2O}}{p_{H_2}^{0.5}} + K_{H_2}(T) p_{H_2}^{0.5} + K_{mix}(T) p_{CO_2}^{0.5} \tag{3.25}$$

$$k(T) = k_{ref} \exp\left(\frac{E_A}{R}\left(\frac{1}{T_{ref}} - \frac{1}{T}\right)\right) \tag{3.26}$$

$$K_x(T) = K_{x,ref} \exp\left(\frac{\Delta H_x}{R}\left(\frac{1}{T_{ref}} - \frac{1}{T}\right)\right) \tag{3.27}$$

Eqs. (3.26 – 3.27) accounts for the kinetic and adsorption temperature-dependent constants and K_{eq} refers to the equilibrium constant calculated through an empirical correlation according to [51], [56]. The conditions under which the above rate model was parameterised were around 423 K and 723 K, and between 1 and 9 bar (at stoichiometric and non-stoichiometric feeds). The kinetic parameters for Eqs. (3.26 – 3.27) are stated in Table 3-4.

Table 3-4. Parametrization for Koschany et al. (2016) catalytic rate equation (T_{ref} = 555 K).

Kinetic parameter	Value	Units
k_{ref}	3.46e-4	mol/ (bar s g_{cat})
E_A	77.5	kJ/mol
$K_{OH,\,ref}$	0.50	$bar^{-0.5}$
ΔH_{OH}	22.4	kJ/mol
$K_{H_2,\,ref}$	0.44	$bar^{-0.5}$
ΔH_{H_2}	−6.2	kJ/mol
$K_{mix,\,ref}$	0.88	$bar^{-0.5}$
ΔH_{mix}	−10.0	kJ/mol

3.3.3 Stage 1: Reacting channel design

The first stage addresses the design of a single reaction channel, which is assumed to have a semi-circular cross-sectional area and to be of a wall-coated type. In order to design this reactor component, the geometry is parameterised through different entities. The particle size (d_p), catalytic layer thickness (δ_{cat}), steel wall thickness (δ_{steel}), and reaction channel width (W_{mc}) and height (H_{mc}) are used as geometric parameters. A reaction channel length (L) of 70 mm is fixed to establish a baseline comparison amongst the several configurations evaluated. Nevertheless, later

on, the effect of L on the system performance and how it might improve productivity is discussed. A scheme of the simulated reaction channel and its parameterisation is depicted in Figure 3-2. A mathematical relationship between those parameters is established as described below.

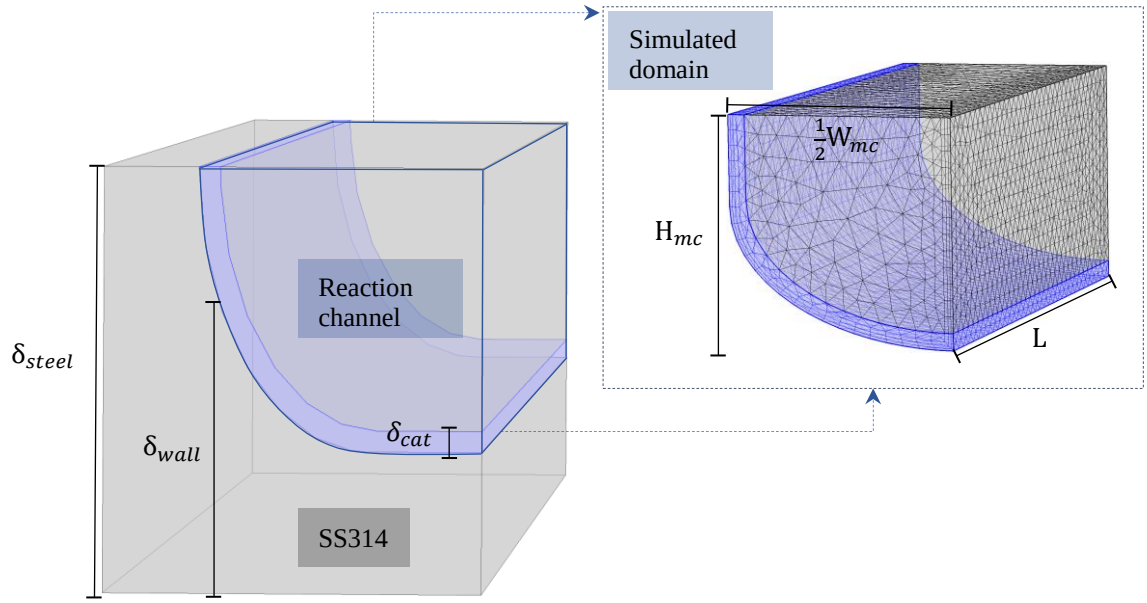

Figure 3-2. Parameterisation of the reaction channel design.

The particle-resolved theory is used to set a relationship between the particle diameter and the catalytic layer thickness. This concept empirically suggests that for packed-bed regions with a low catalytic layer to particle diameter ratio (<15), the non-homogeneous bed morphology has a significant impact on the fluid dynamics (local flow effects), as well as the heat- and mass-transfer uniformity [57], [58]. That is to say, the pseudo-homogeneous assumption for the phenomenological model applied in the catalytic domain from Table 3-1 is no longer valid below a layer-to-particle ratio of 15. Hence, the minimum ratio is used, yet retaining the applicability of the pseudo-homogeneity principle. Further, the catalyst layer thickness can be expressed as a fraction (f_{cat}) of the total channel width, whereas a channel width-to-height ratio of 2 is fixed. Accordingly, the described relationships are expressed via Eqs. (3.28 – 3.30).

$$\delta_{\text{cat}} = 15\, d_p \tag{3.28}$$

$$W_{mc} = 2\, \delta_{cat}/f_{cat} \tag{3.29}$$

$$H_{mc} = \tfrac{1}{2} W_{mc} \tag{3.30}$$

Note that both d_p and f_{cat} are set as independent geometric parameters in the reacting channel design stage. The variation range for both entities is given in Table 3-5. Any parameter change implies an alteration in the geometry, thus affecting the energy and mass transfer resistances. For instance, the heat transfer coefficient at the boundaries is re-estimated as given by Eqs. (3.17 –

3.18). As discussed later, the catalytic layer thickness becomes crucial for system behaviour due to the transport resistances that depend on it.

Table 3-5. Geometrical variables evaluation range.

Parameter	Lower	Upper	Units
d_p	5	50	µm
f_{cat}	0.05	0.3	1

As shown in Figure 3-2, the reaction channel design is supported by 3-D simulations, coupling the whole set of PDEs given in Table 3-1 and Table 3-2 for the free fluid and catalytic domains, respectively. The first design stage can be summarized by the scheme depicted in Figure 3-3.

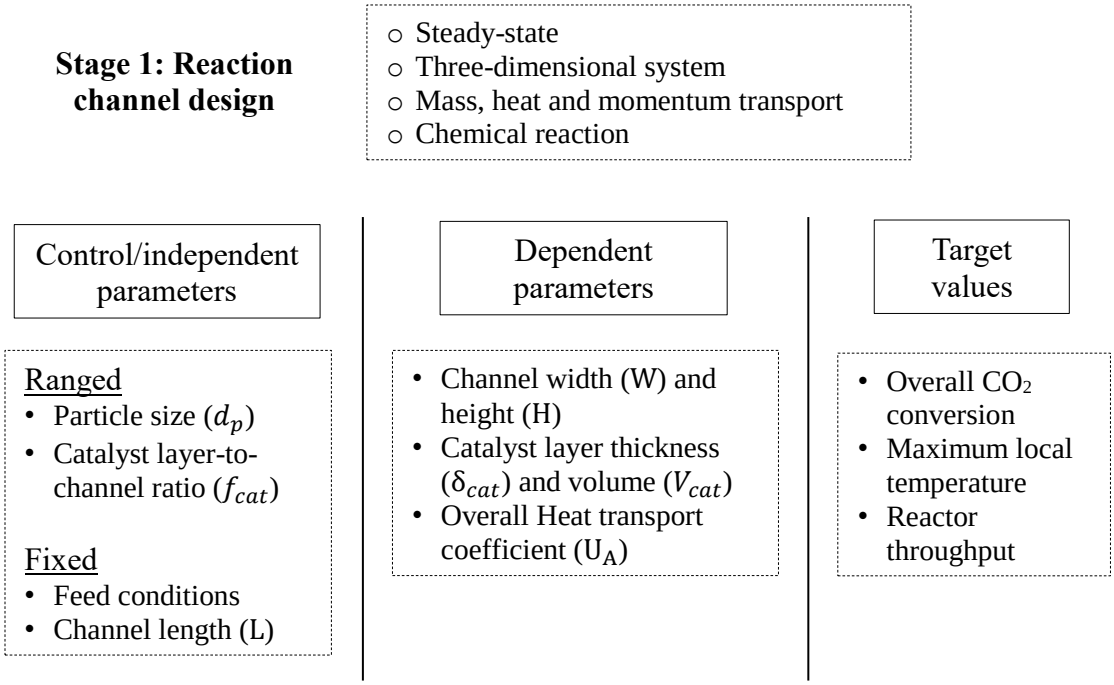

Figure 3-3. Stage 1 scheme: design of reaction channel.

The reactor operating conditions remain constant in all the conducted tests to establish a baseline in which the design parameterisation gives the only variability. These conditions are depicted in

Table 3-6 and are selected for being relevant in PtM industrial applications [1], [16], [26], [59]. Note that the Gas Hourly Space Velocity (GHSV) plays a fundamental role during the design as it is maintained constant. An alteration of the reaction channel geometry may affect the wall-coated layer volume (catalytic load) which at the same time changes the processed gas flow through the

reactor according to the fixed GSHV. The volume of the wall-coated layer may be computed using built-in functions in COMSOL for numerical space integration.

Table 3-6. Operating conditions for reacting channel.

Parameter	Lower	Units
T_f	400	K
P_f	8	bar
GHSV	5000	h^{-1}
y_{H_2}	0.8	–
y_{CO_2}	0.2	–
T_{cool}	550	K

The reaction channel design criteria within the PI concept is aimed at maximising the reactor throughput without ignoring the required gas quality. Therefore, the first reactor component design consists of determining the geometry (parameters) favouring the SNG production in compliance with the established quality threshold (CO_2 conversion above 95 %).

3.3.4 Stage 2: Reactor stacked-plate design

In order to ensure that the design point established in the first stage can be scalable to all the channels that comprise the reacting network, it must be assured that the flow is distributed homogeneously in each of the channels once it enters the plate. Thus, keeping an equal residence time for every reaction channel, while the overall SNG quality requirement is met, and the productivity of one channel is multiplied by the total number of channels in the stacked plate. Two features are encountered to influence the flow distribution once the reagents are fed into each stacked plate: the manifolds geometry and the total number of parallel channels comprising the reaction network (N_{mc}). Each evaluated geometry is tested with a different N_{mc}, ranging from 5 to 25 equal channels, and incorporating the defined design point for a single reaction channel found in the previous design stage (section 3.3.3).

First, a preliminary evaluation to define the best manifold geometric configuration is made between four different possibilities, as shown in Figure 3-4. To analyse a diverse set of geometries, a triangular manifold configuration (Geo. 1), a square one (Geo. 4) and two curvilinear with different angles (Geo. 2, Geo. 3) are proposed, all of which are tested as a function of N_{mc}. The latter two are constructed using the so-called Bezier curves. The triangular-like configuration turns out to be the one with the optimum laminar flow distribution as discussed later on, and in agreement with recorded literature [60].

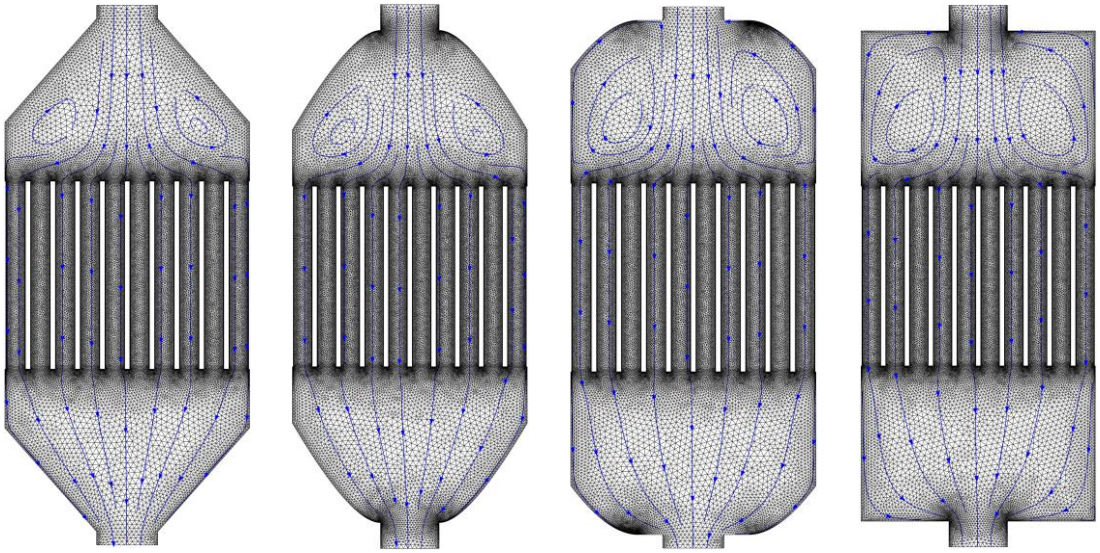

Figure 3-4. Design of the stacked-plate: velocity field for the proposed geometries with an arbitrary number of reaction channels.

Second, two new configurations are examined. In the first one, the fluid is transported freely over the manifold from the stacked plate entrance and into the reaction network. In the second one, there is a midway obstruction aimed at improving the flow uniformity over the staked plate. Figure 3-5 depicts a scheme for the evaluated configurations. Both configurations in Figure 3-5 are parametrised defining a relationship between the manifold length (L_{mfld}) and its width (W_{mfld}), in which the latter would depend on N_{mc}. This manifold length-to-width ratio (f_{mfld}) is expressed by Eq. (3.30).

$$f_{mfld} = L_{mfld}/W_{mfld} \tag{3.30}$$

Table 3-7 lists the intervals in which both N_{mc} and f_{mfld} are changed. Accordingly, 65 simulation runs (N_{mc} = 5, f_{mfld} = 13) are performed for each configuration in the second case study (Figure 3-5). In that sense, a manifolds triangular-like geometry is sized as a function of N_{mc} looking for the best uniform flow distribution.

Table 3-7. Evaluation range for the manifold geometrical parameters.

Parameter	Lower	Upper
N	5	25
f_{mfld}	0.6	4

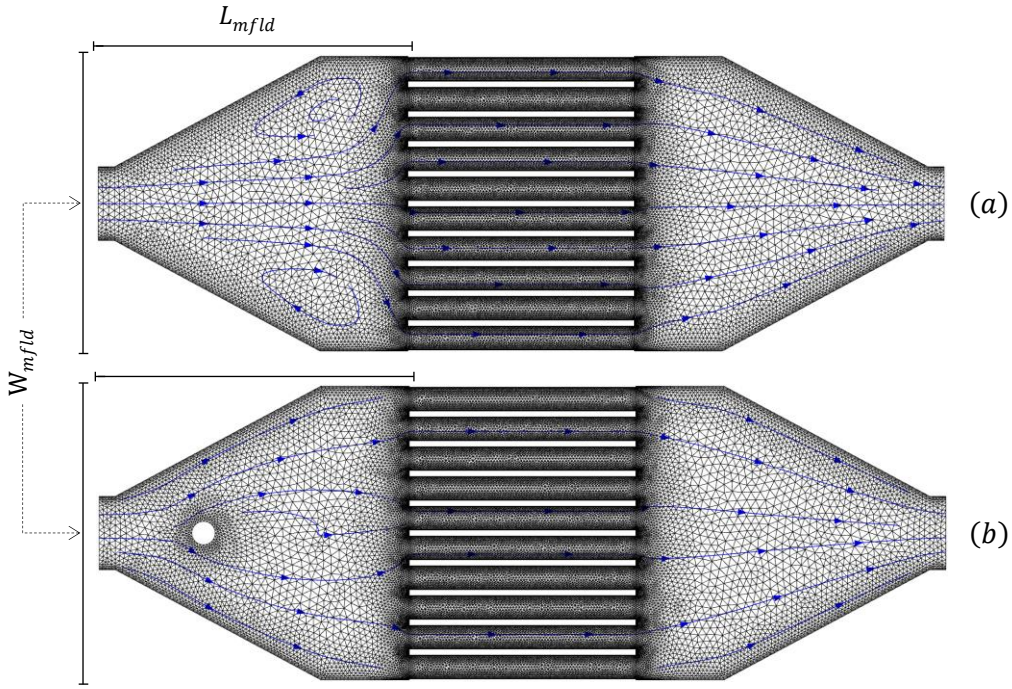

Figure 3-5. Design of the stacked-plate: velocity field scheme for the free (A) and obstructed (B) flow configurations.

In any case, the criteria used to determine the best geometric features is the quality or uniformity of flow distribution, as described by Eq. (3.31). Herein, the flow distribution is mathematically expressed by the relative standard deviation (σ) of the fluid velocity in all the reaction channels. F_j stands for the averaged velocity (magnitude) along the inlet boundary of each channel. Hence, $\bar{F}$ is the averaged F_j for the total number of channels (N_{mc}). In consequence, a larger relative standard deviation implies a lower uniformly distributed flow over the channels.

$$\sigma = \frac{1}{\bar{F}}\sqrt{\frac{\sum_j \left(F_j - \bar{F}\right)^2}{(N_{mc} - 1)}} \tag{3.31}$$

Moreover, the whole stacked plate design is supported by 2-D simulations assuming an isothermal cold flow state (without chemical reaction). In all the tests, a stacked plate is first 3-D designed and then sliced through the plane that is halfway up the channel resulting in the respective 2-D geometry. Only the momentum transport and continuity governing equations for the catalytic and free fluid domains are coupled and solved. Note that in this case, the gradient operator $\vec{\nabla}$ in Table 3-1 and Table 3-2 accounts for the vector $\frac{\partial}{\partial x}\hat{\imath} + \frac{\partial}{\partial z}\hat{\jmath}$. Still, the operating conditions given in

Table ***3-6*** are applied except for feed temperature, in which case, the system is assumed to be at the coolant fluid temperature. The second design stage is schematically summarized in Figure 3-6.

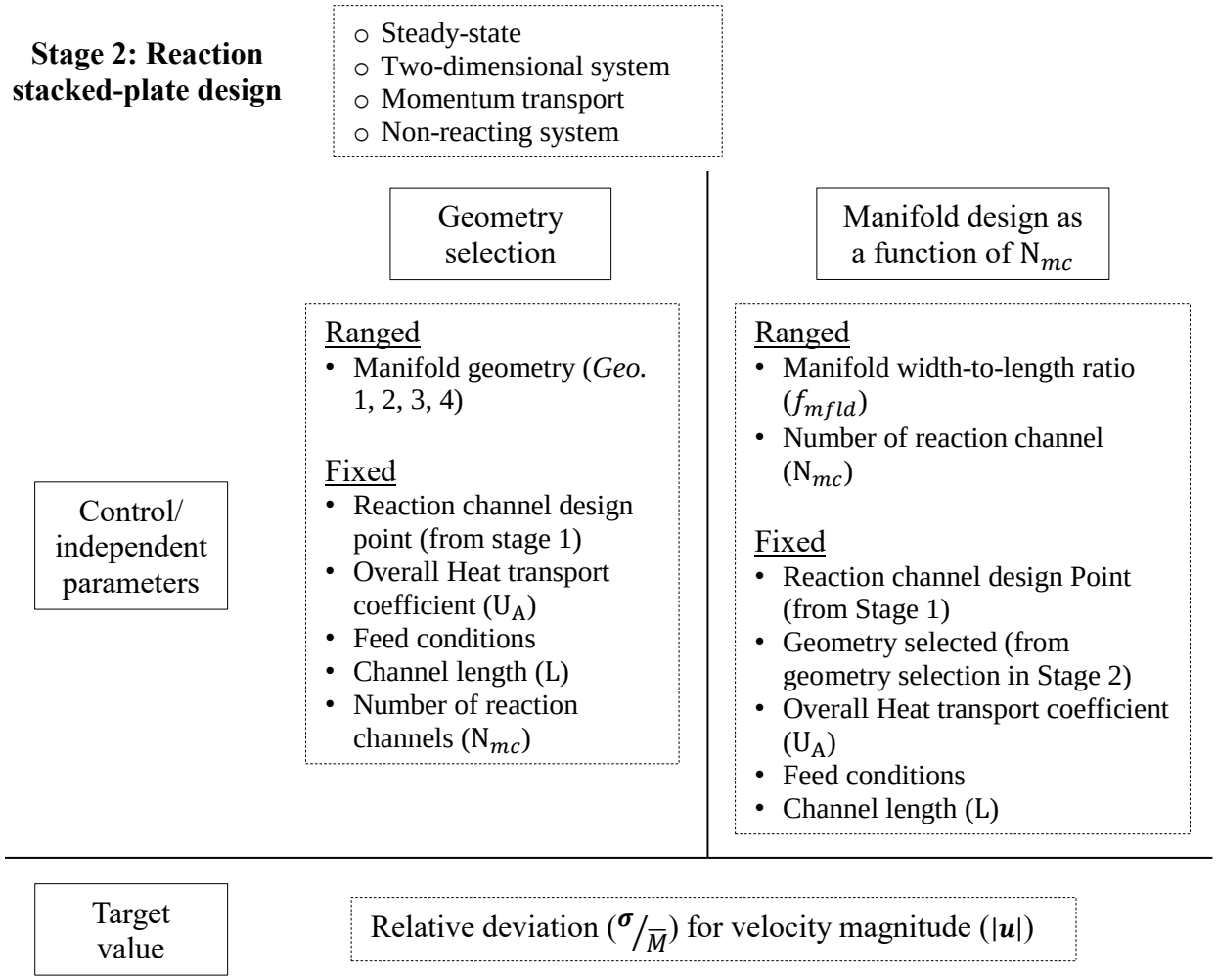

Figure 3-6. Stage 2 scheme: Reactor stacked-plate design.

3.3.5 Stage 3: Three-dimensional stacked plate evaluation

A first set of simulations (section 3.3.3) is carried out to stablish a design point for the reaction channel alone based on yield and quality criteria, and a second set (section 3.3.4) to define the manifold geometrical features that allow the best results in terms of flow uniformity. The stage 3 aims to merge the results found in the former stages through a reduced number of larger scale simulations.

Two case studies are conducted. In the first case the results obtained for a single reaction channel in stage 1 are attempted to be replicated when evaluating a 3-D reactor stacked plate composed of equal parallel channels (see Figure 3-1) and the reasonability in the assumption of 2-D simulations in stage 2 is discussed. N_{mc} is again taken as a variable factor for the 3-D simulations, using the same range defined in stage 2. In the second case, the feasibility of increasing the reactor throughput by merely modifying the reaction channels length (L) is studied. Parameter which has

so far been kept unchanged at 70 mm in all the simulation sets. Unlike the first case study, in the latter N_{mc} is defined to be constant (N_{mc}=10). The third design stage can be summarized by the scheme depicted in Figure 3-7.

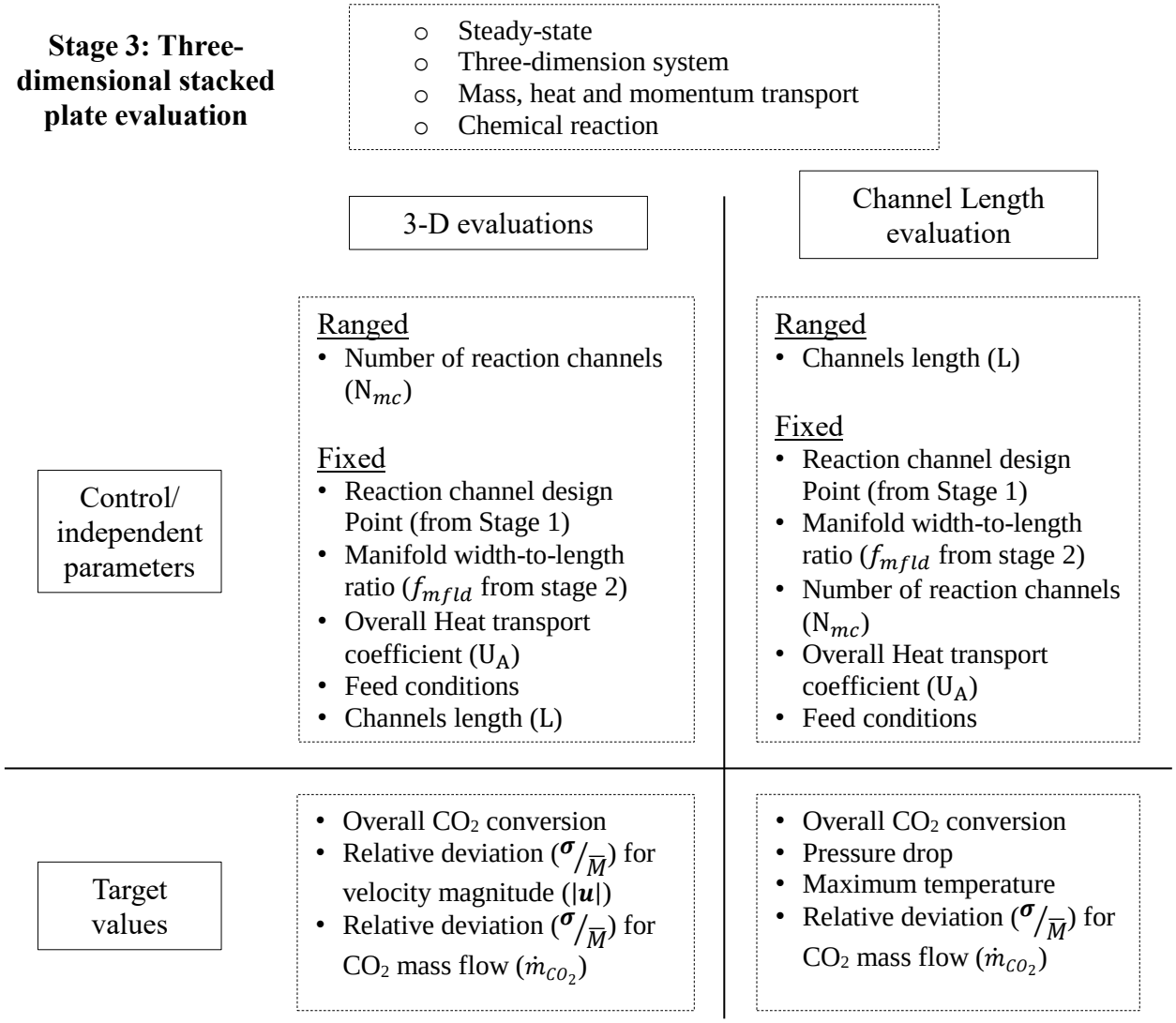

Figure 3-7. Stage 3 scheme: 3-D evaluation of the entire stacked plate.

3.3.6 Dynamic analysis

Finally, after defining the channel and the manifold geometry, a preliminary dynamic analysis of the system was made through a start-up and shut-down simulation. In this case, the variables were oscillated in one direction only and then back to the first point, expecting the system to show hysteresis behaviour. Due to the high computational effort, especially in the data storage, a two-dimensional system was attempted again but involving the whole transport phenomena coupled in the fluid and porous medium.

The disturbance made to the system to simulate the start-up/shut-down behaviour is shown in Figure 3-8. The initial temperature is set to 400 K; nonetheless, after a few milliseconds, the system is disturbed through the input gas and coolant temperature. The reactor is fed with a stoichiometric, undiluted gas mixture of hydrogen and carbon dioxide at the same pressure and GHSV conditions described previously. Likewise, to simulate the shut-down process, after almost 0.04 s, the inlet and coolant temperature are smoothly reduced back to 400 K. The remaining conditions, such as the gas composition, stay unchanged.

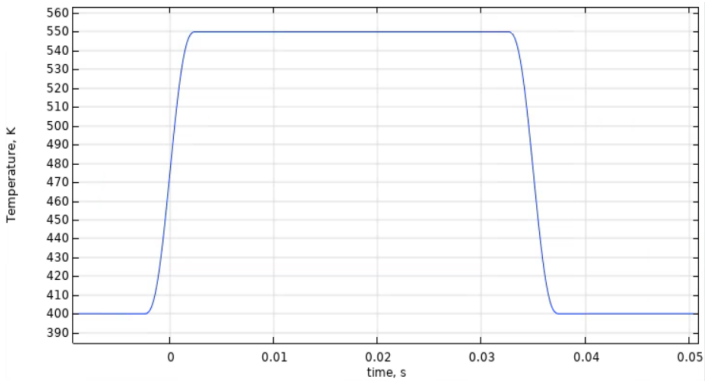

Figure 3-8. On-off temperature disturbance.

3.3.7 Computational aspects

Specifications regarding the computer equipment employed to perform the computations are summarized in Table 3-8, where no GPU was utilized. The computational cost varies depending on the design stage of each component. For instance, the effort is high for the reaction channel design since it is a three-dimensional simulation. Thus, in this case, the simulations were performed by refining the regions near the system boundaries where the catalyst layer is located. The latter because, in some cases, the thickness of the catalyst layer required it.

For the design of the manifold geometry and the network of parallel reaction channels, firstly, it involves a two-dimensional simulation, and secondly, only the velocity and pressure profile are solved through the momentum transport equations. Thus, the mathematical complexity is also reduced. The mesh resolution, in this case, was affected by the number of reaction channels in the simulated stacked-plate. As the number of channels increases, the gas velocity increases according to the GHSV, and convergence is impaired. Therefore, in order to alleviate this issue, fine to extremely fine meshes were employed according to the COMSOL mesh building definition.

Table 3-8. Computational resources.

Operating system	Windows Subsystem for Linux
Processor	Intel(R) Xeon(R) CPU E5-1620 v4 @ 3.50 GHz

CPU cores	4 Cores, 8 Logical Processors
Installed physical RAM	32.0 GB
Hard Disk Drive (HDD)	4TB Hard Drive SATA - 5400 RPM 3.5-inch

3.4 Results

3.4.1 Reacting channel design

The catalyst layer is affected by the particle size (d_p) and the porous layer-to-channel width ratio (f_{cat}) according to the parametrisation previously detailed. Figure 3-9 show the way the wall-coated volume is increased by higher d_p and lower f_{cat}, where the former is ranged from 5 to 50 um and the latter between 5% and 30%. In other terms, changing d_p and f_{cat} alter the channel geometry and its surface-to-volume ratio, resulting in distinct transport rates and resistances. Acknowledging this relationship is crucial to interpret the results in Figure 3-10 on the reaction channel design.

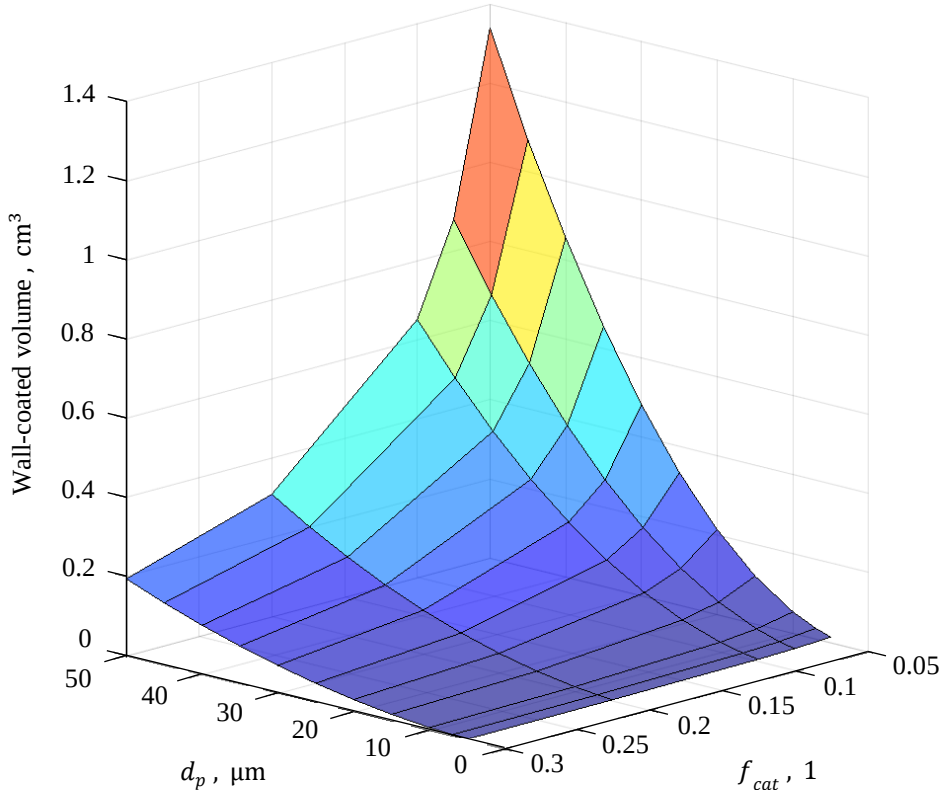

Figure 3-9. Effect of the particle diameter (d_p) and the catalyst layer-to-channel width ratio (f_{cat}) on the wall-coated layer volume.

Figure 3-10(a) shows the effect of the particle size on the channel temperature at several porous layer thickness-to-channel width ratios. The particle size increase implies a larger channel and a lower surface-area-to-volume ratio, pointing to lower heat transfer coefficients and higher resistances. Consequently, an increase in temperature occurs as expected. Note that Figure 3-10(a) displays the maximum temperature reached throughout the entire domain, located at some point over the porous medium. Hence it does not describe the system's temperature level.

The second effect shown in Figure 3-10(a) refers to the porous layer-to-channel width fraction and the way it affects the maximum temperature reached along the channel. A lower fraction means a wider channel and, thus, a lesser surface-to-volume ratio. The latter strengthens the idea that the surface-to-volume ratio is the predominant factor. Consequently, a decrease in this relation leads to stronger transport resistances accounted by the heat transfer coefficient, and a reduced heat removal capability, resulting in energy accumulation and general temperature level increment.

A positive result is the avoidance of hot spots (T > 775 K) in any of the cases, due to a sufficiently effective heat removal. These results agree with those obtained for similar wall-coated systems such as the plate heat exchanger exemplified in [25], but differ from other microstructured reactors such as the one studied by Kreitz et al., where, despite being an intensified reactor under equivalent conditions, hot spots are present [26]. Clearly, this shows the enhanced heat management of a wall-coated system over a micro-packed bed one.

Figure 3-10(b) shows the catalyst particle size effect on the CO_2 conversion, which is estimated using Gauss's theorem expressed via Eq. (3.32).

$$X_{CO_2} = 1 - \left\{ \iint_{z=L} \rho_{CO_2} (u \cdot n)\, dS \Big/ \iint_{z=0} \rho_{CO_2} (u \cdot n)\, dS \right\} \tag{3.32}$$

In rigorous terms, the required gas quality may vary depending on its application and geographic conditions. For instance, if the SNG produced is expected to be used as liquid gas (L-Gas) in Germany, a minimum CO_2 conversion of 98% or higher would be required to assure a methane content above 90% on a dry basis [59]. Conversely, if the product requirements are less strict, lower conversions might be sufficient. Herein, a CO_2 conversion of 95% is taken to be a reference point. Therefore, only the results above this baseline are considered as possible design points.

The increased particle size presented in Figure 3-10(b) implies a decay of the conversion evaluated at the reactor outlet boundary. This trend is again ascribed to the established geometrical relationship shown in Figure 3-9. Larger particle sizes mean thicker catalytic layers, and larger mass transfer resistance. Thus, diffusion from the bulk fluid into the wall-coated layer becomes

predominant, resulting in slower reaction rates. Likewise, the previous temperature analysis on Figure 3-10(a), the f_{cat} strongly affects conversion. In this respect, as the f_{cat} increases from 5% to 30%, there are shorter diffusion paths between the bulk fluid and the catalytic layer, which improves the reaction rate. Note that comparing different values of f_{cat} at the same d_p means contrasting channels with wall-coated layers with equal thickness but distinct catalytic layer-to-channel width proportion.

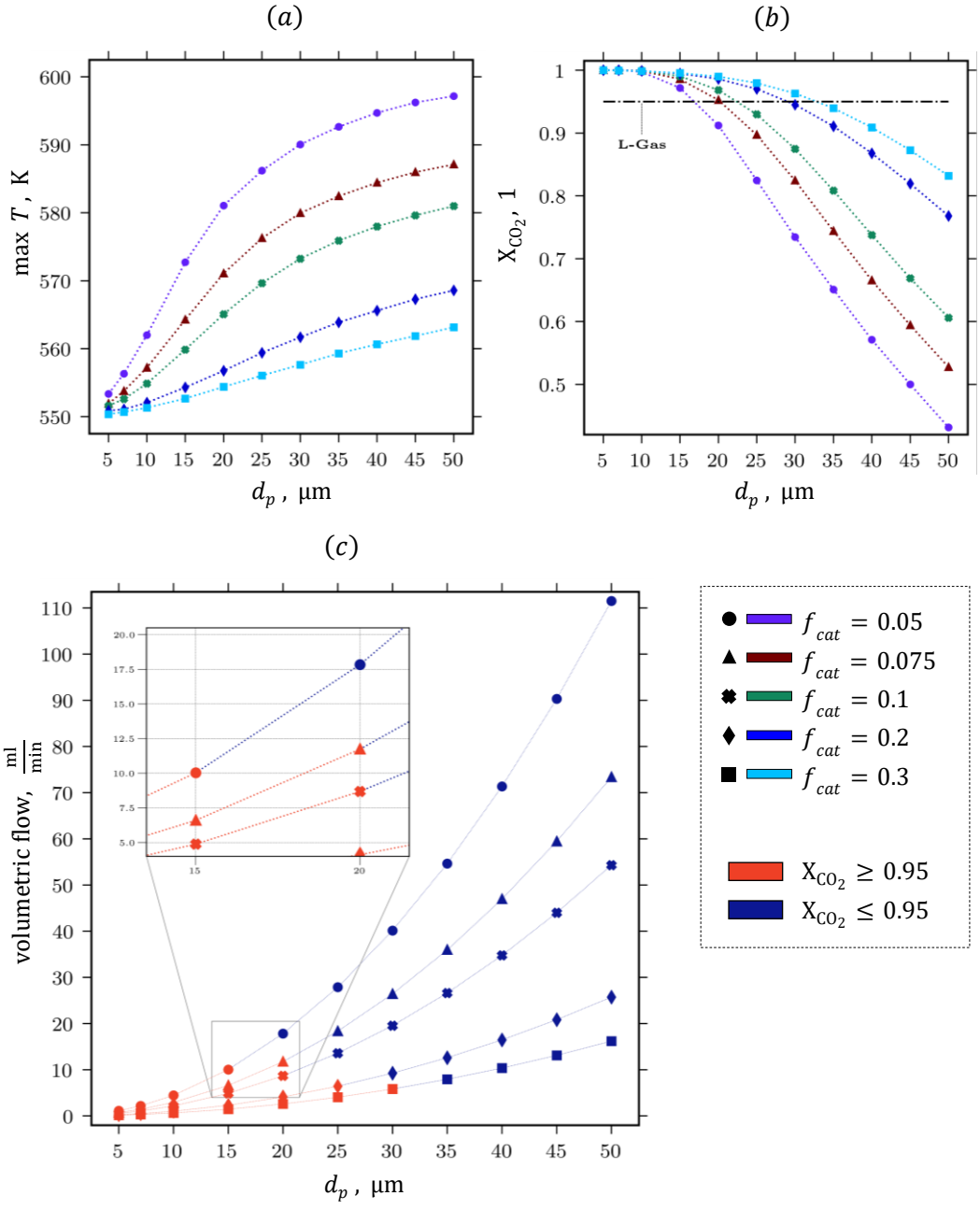

Figure 3-10. Results for the reaction channel design (stage 1). (a) Effect of the particle diameter on the maximum temperature achieved along the milli-channel. (b) Effect of the particle diameter

on CO_2 conversion at the outlet of the milli-channel. (c) Selection of the design point base on the minimum required quality and the maximum possible throughput.

Interestingly, when analysing Figure 3-10(a) and Figure 3-10(b) is to observe that the highest conversions do not coincide with the highest maximum temperatures. Several factors converge and need to be understood simultaneously to explain this phenomenon. The increase of the particle size and the volume-to-surface ratio (given by f_{cat}) triggers a temperature increase (which favours the reaction rate), as well as an increment of the mass transfer resistances, which in any case slows down the reaction rate. Consequently, the fact that there is a drop in CO_2 conversion indicates that mass transfer resistances have a predominantly negative effect even though the system temperature level tends to be higher. In other words, the increase in temperature does not mean a larger reacting volume but a reduced heat removal capacity.

Figure 3-10(c) presents a comparison of the total throughput in all simulated cases. Following the discussion in the previous paragraph, the points highlighted in *blood-red* denote the geometries in which the conversions obtained are above the proposed minimum threshold (X_{CO_2}>0.95). As expected, it is observed that as the particle size increases, so does the amount of processed gas. Indeed, the increase in particle size implies a higher catalyst load and a superior volumetric flow rate of processed gas, given the GHSV (remaining constant at 5000 h^{-1}). Accordingly, the design point is selected, being the geometric conditions that enable processing the highest amount of gas, still fulfilling the minimum quality limit.

Finally, it is possible to establish the design point (structural parameters), resulting in the reaction channel with the best performance within the assessed conditions range. Figure 3-11 shows the simulated reacting channel at the design point. Therefore, the original question about the extent of the process intensification for the methanation reactor is met. The reaction channel geometry with the highest performance fits in the millimetre scale, with a catalytic layer of 300 μm in thickness, packed with catalyst particles of 20 μm in diameter and a total length of 70 mm. The catalytic-layer-to-channel-width fraction is 0.075, indicating that the channel is 8 mm wide and 4 mm high. Further, given those structural parameters and spatial velocity (GHSV = 5000 h^{-1}), the gas processed per channel is about 12 mL/min with an overall conversion of 95 % and maximum local temperature of about 574 K.

The former result stands out as the main outcome of this research, proving the advantages of the dimensioned system. The feasibility of operating at a higher temperature level is demonstrated, which guarantees on the one hand the fulfilment of the settled quality requirements and on the other hand a satisfactory thermal management. A case which, as relevant studies of the PtM concept have shown, could not be carried out in conventional reactors under conditions equivalent to those simulated in this work [14], [16], [18].

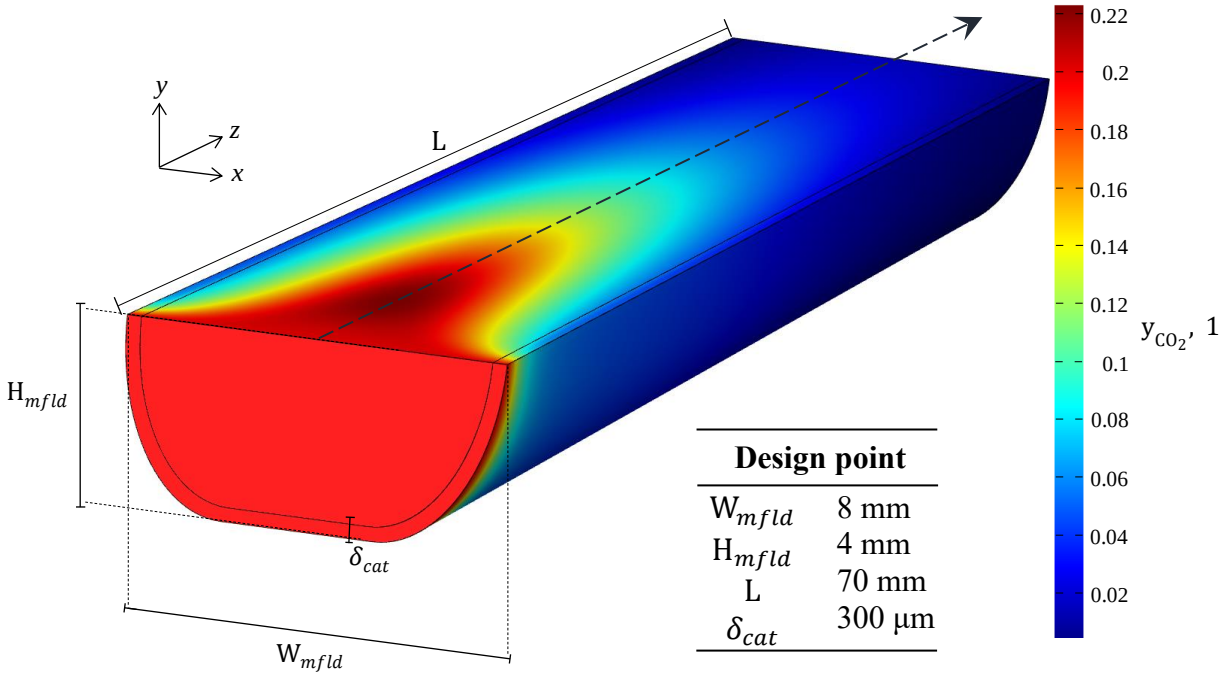

Figure 3-11. Three-dimensional molar fraction scalar field for the CO_2 molar fraction. The geometry of the reacting channel is presented at the design point. Parametrisation: channel width (W_{mfld}), height (W_{mfld}) and length (L), and wall-coated thickness (δ_{cat}).

3.4.2 Stacked-plate design

As mentioned in the methodology (Section 3.3.4), the stacked-plates conceptual design was subdivided into two. First, the evaluation of different manifold and collector geometries. Second, the study of two type of configurations (free- and obstructed-flow) aimed at improving the gas flow uniform distribution over the reaction network. In all the cases, the relative standard deviation was used as a baseline calculation to estimate and compare the flow rate uniformity between different configurations. Hence, a larger relative standard deviation corresponds to a less uniformly distributed flow over the channels.

All the simulation sets for the stacked plate design are 2D, solely considering momentum transport. Indeed, the channel is near isothermal since the gas mixture quickly reaches the coolant temperature due to the high heat-transfer rate resulting from the intensification approach. Since the stacked plate design focuses merely on the system performance across the manifold and up to the channels entrance border to guarantee an even flow distribution. Therefore, there is no homogeneous reaction which means the reacting flow does not react until it contacts the catalytic layer. Without energy release due to reaction, the temperature change is merely attributable to the external heat-transfer. Likewise, there is no change in the gas mixture compositions entering the stacked plate until it reaches the reacting channels. The above to say that the assumption of

suppressing the mass and energy transport equations is valid plus lowers the computational cost and makes it easier to perform a large number of runs.

Concerning the evaluation of four geometries and according to Figure 3-12, *Geo.1* has the lowest deviation regardless of the number of channels, whereas *Geo.4* the highest. Notwithstanding, as the number of channels in the plate augments, any gap between the 4 investigated configurations become negligible. The latter trend is due to the increased gas flow caused by the larger number of channels, according to the constant GHSV. Therefore, it is fair to affirm that as the gas flow increases, it becomes irrelevant the employed manifold geometry in terms of flow rate distribution uniformity. Accordingly, the triangular-like geometry is adopted (so-called *Geo.1*) as the one with the optimum laminar flow distribution among the studied geometries.

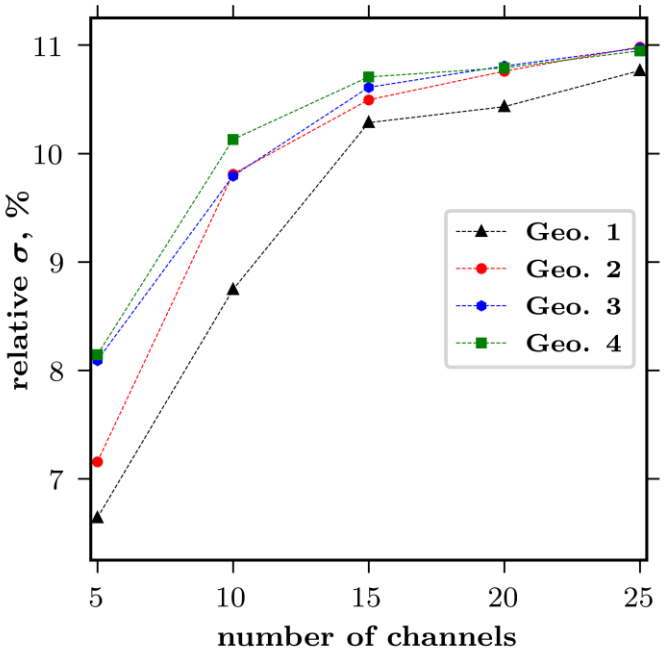

Figure 3-12. Relative standard deviation obtained for four different manifold geometries and milli-channels. Triangular-, square- and curvilinear-like alternatives are considered (*Geo.*1, 2, 3 and 4, respectively).

The next step involves the simulation of the selected geometry (*Geo.1*), evaluating several manifold-length-to-width ratios (f_{mfld}), again as a function of the number of reacting channels. Figure 3-13 shows the effect of several manifold-length-to-width ratios (f_{mfld}) on the stacked plate flow distribution at a precise number of milli-channels and for two cases, a free- (a) and obstructed-flow (b) configuration. The former (Figure 3-13(a)), in which the fed gas flow freely through the manifold and the latter (Figure 3-13(b)), in which the gas was partially obstructed halfway through before entering the reacting channels. The relative standard deviation was used

as a baseline calculation to estimate and compare the flow rate uniformity between different configurations. Hence, a larger relative standard deviation corresponds to a less uniformly distributed flow over the channels.

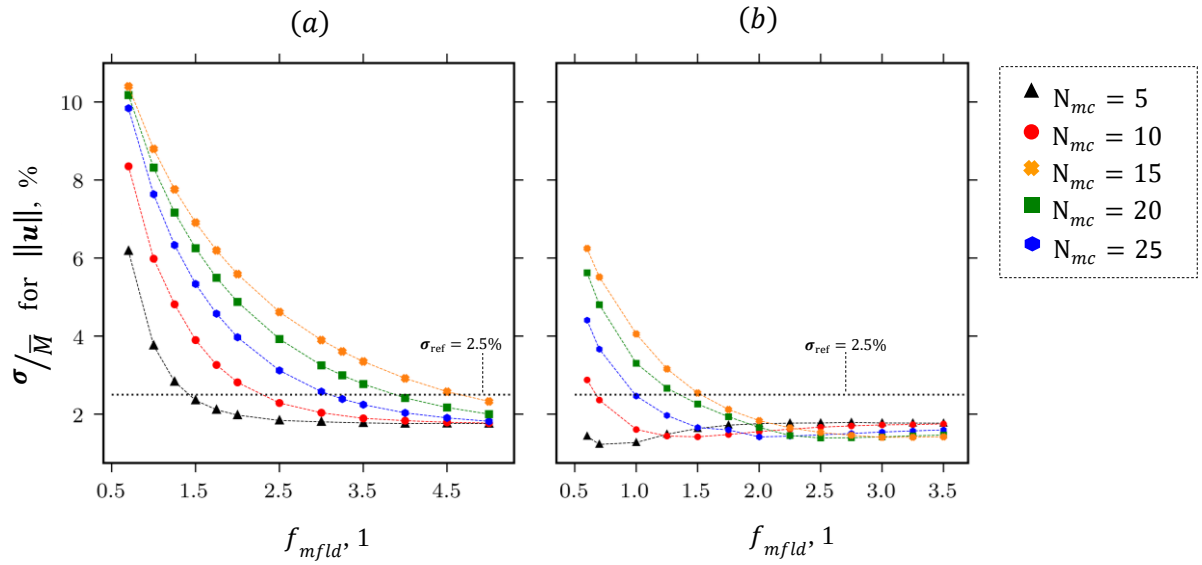

Figure 3-13. Relative standard deviation obtained for a free-flow (a) and an obstructed-flow (b) manifold with different number of milli-channels.

In the free-flow case, an increase in the manifold-length-to-width ratio benefits the flow rate distribution as it becomes uniform. However, this trend becomes negligible as the same parameter increases. In the obstructed-flow case, a substantial improvement in the flow distribution uniformity is evident regardless of the number of channels. A standard deviation line of 2.5% is drawn as a reference point to facilitate the comparison of both cases. This analysis is crucial if the reactor is to be manufactured by minimizing the amount of material utilized. Although a longer manifold favours flow distribution, its effect becomes irrelevant and does not justify the use of additional material beyond a certain degree. In either case, a manifold with a flow obstruction is preferred.

3.4.3 Three-dimensional stacked plate evaluation

In order to merge the first and second design stages as well as to validate the previous results on a larger scale, 3-D simulations of the entire stacked plate are performed. Thus, the dimensions that provide the best results for the single reaction channel in terms of yield and quality (design point) and for the manifolds regarding flow uniformity are selected. Part of the validation is also to discuss the discrepancies that may exist between the results obtained from the 2-D and 3-D simulations concerning the manifold design. In the latter case, both the best configurations (obstructed flow) and those that suggest a poor flow uniform distribution (free flow) are discussed.

Table 3-9 summarises the specifications of each of the simulations that were conducted. In all cases a triangular-like geometry (Geo. 1) was adopted because of its superior results compared to the other geometries (see Supplementary material). Furthermore, whereas for free-flow configurations a constant f_{mfld} of 1 was used resulting in $\sigma/\bar{M}$ above 2.5 % (see Figure 3-11), for obstructed flow configurations different values of f_{mfld} that result in $\sigma/\bar{M}$ below the reference (2.5%) were employed.

For the latter, those configurations do not necessarily lead to the minimum deviation, otherwise it would imply simulating the stacked-plate with higher material usage. Simulations with the maximum number of channels (25) stablished for the previous stages were not incorporated due to the high computational effort this requires when dealing with three dimensions.

Table 3-9. Evaluation range for the manifold geometrical parameters.

N_{mc}	Reaction channel design	Stacked-plate (Geo. 1, free-flow)	Stacked-plate (Geo. 1, obstructed-flow)
5	Design point (see Figure 3-11)	$f_{mfld} = 1.0$	$f_{mfld} = 0.7$
10			$f_{mfld} = 1.0$
15			$f_{mfld} = 1.5$
20			$f_{mfld} = 1.75$

Figure 3-14 depicts composition, velocity and pressure profiles for a 10-milli-channel stacked-plate with flow obstruction, one of the simulated 3-D cases according to Table 3-9. At first glance, a uniform flow distribution is observed along the stacked plate where y_{CO_2} decreases from 20 % (stoichiometric ratio) to 2 % as formerly obtained in the single channel simulation while y_{CH_4} increases to around 30 %.

Besides, as shown in Figure 3-14(c) the velocity profile shows a noticeable drop in magnitude at the plate entrance and in the region close to the blockage. Indeed, there is pressure drop of about 0.5 pa, still much lower than conventional reactor with about 1 bar [15]. The latter can be justified by the fact that the channels are not completely packed as in a fixed bed reactor. Figure 3-14 offers a qualitative analysis of one of the multiple 3-D cases in Table 3-9. Nonetheless, in order to accurately determine whether or not 3-D simulations validate the results obtained in the previous stages, values such as the overall CO_2 conversion and the $\sigma/\bar{M}$ for CO_2 mass flow and gas velocity are derived and compared as shown in Figure 3-15.

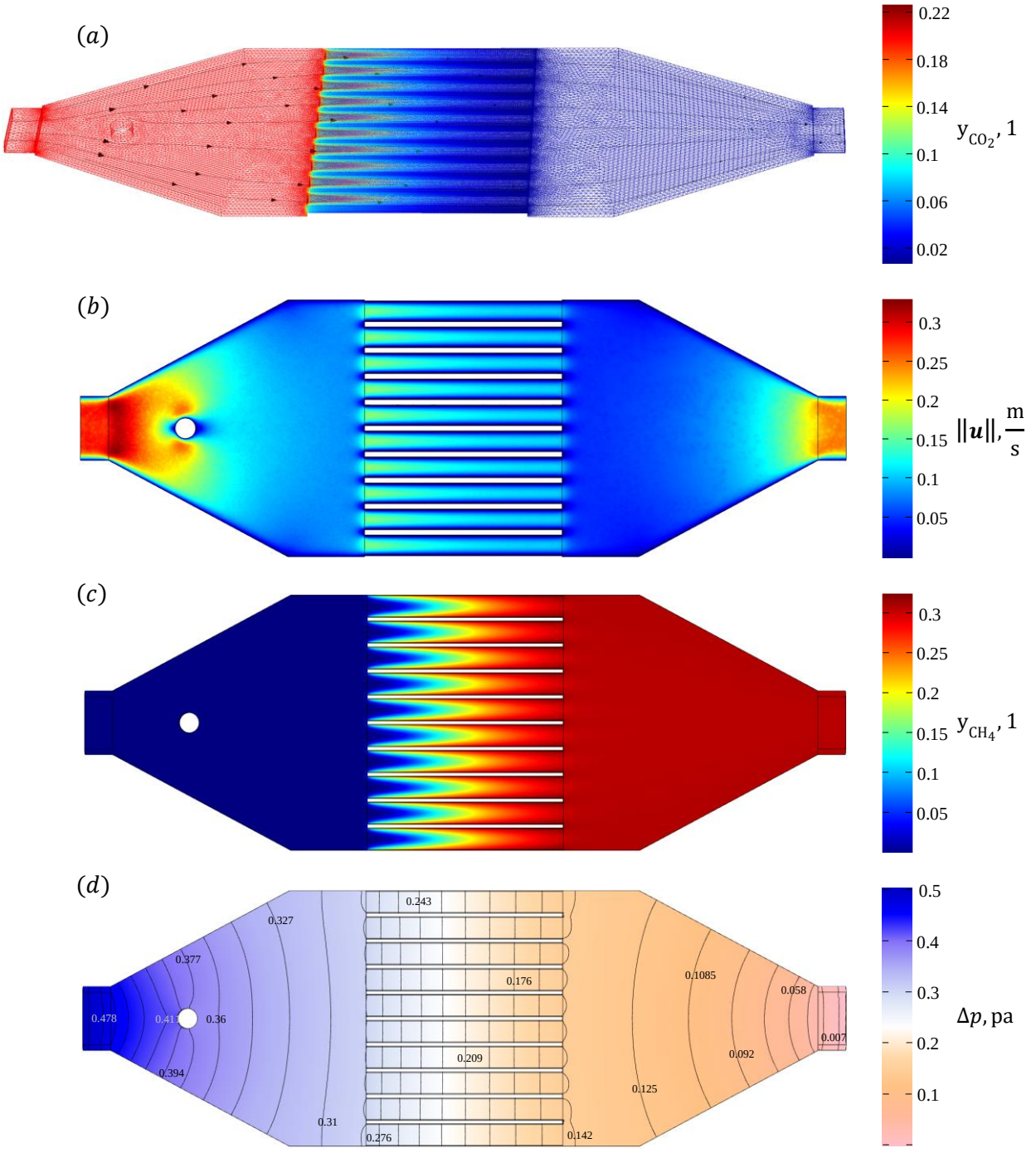

Figure 3-14. Three-dimensional simulation results for a stacked-plate with flow obstruction, comprising 10 reaction milli-channels and a f_{mfld} of 1.0. (a) 3D wireframe perspective of the CO_2 molar fraction profile over the entire stacked-plate. (b) Stacked-plate top view of the velocity magnitude profile. (c) Stacked-plate top view of the CH_4 molar fraction profile. (d) Stacked-plate top view of the pressure drop profile with contour lines.

Figure 3-15(a) compares the overall conversion of the entire stacked-plate for the cases with and without obstruction, indicating that the latter configurations guarantee a minimum conversion for the SNG to be re-injected into the natural gas grid as L-Gas. Indeed, the corresponding conversion attained is equivalent to that obtained for the design point (about 95 % of CO_2 conversion). It is also shown that despite the impoverishment of the uniform flow distribution for the free-flow configurations, the CO_2 conversion is close to the required minimum L-Gas quality.

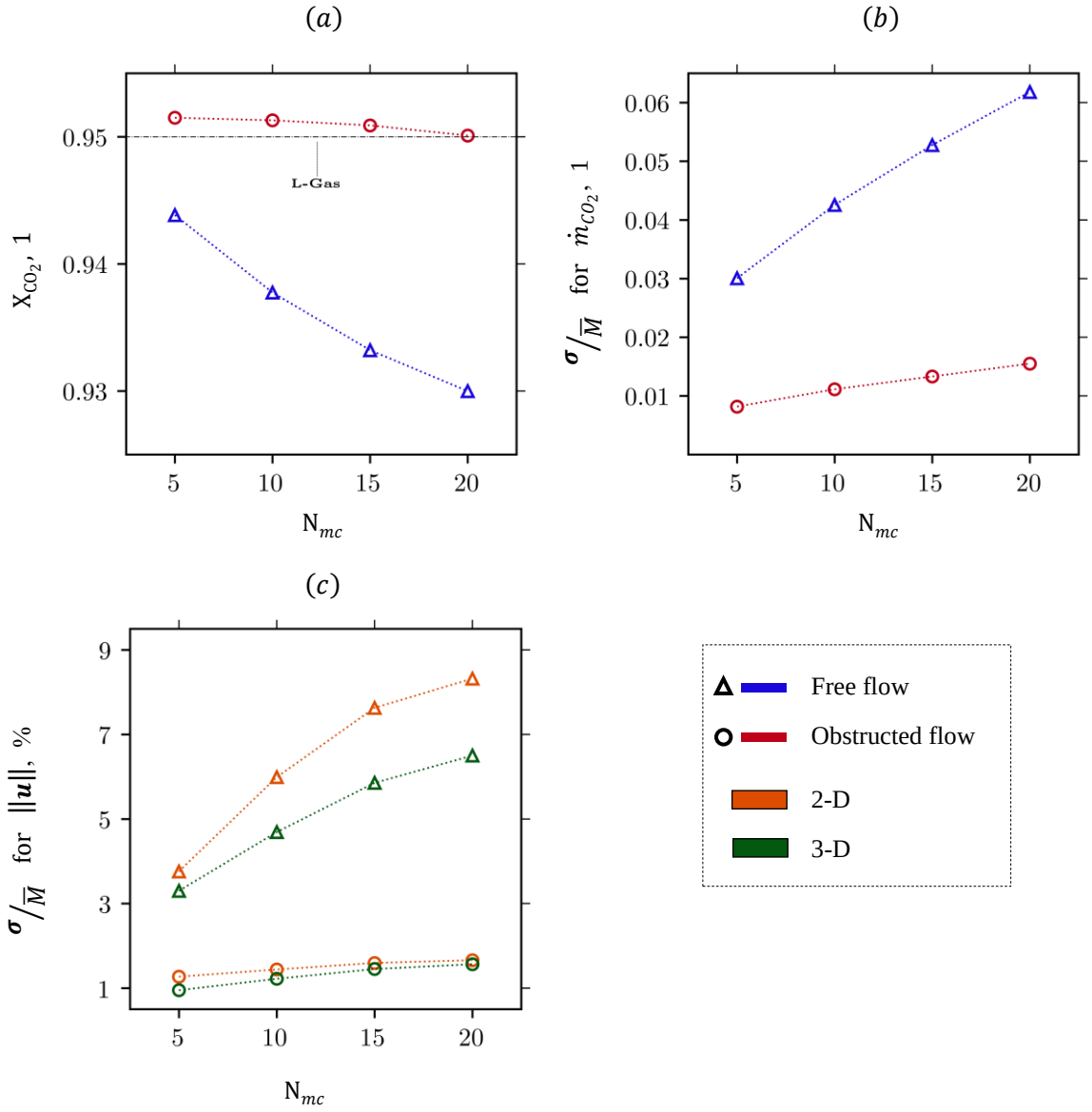

Figure 3-15. Three-dimensional validation of the results yielded in the previous design stages (Sections 3.3.3 and 3.3.4). (a) Overall CO_2 conversion attained for free-flow and obstructed stacked-plates as function of the number of reacting milli-channels. (b) Relative standard deviation for the CO_2 mass flow evaluated at the reaction channels inlet boundary. (c) Comparison

of the relative standard deviation for the velocity obtained in the 3D cases and their equivalent values in the 2D simulation of Section 3.3.4.

Figure 3-15(b) compares the $\sigma/\bar{M}$ for CO_2 mass flow for the obstructed and free-flow configurations. Although the discrepancies are not as obvious as with past simulations, it does show that there is a noticeable effect of the obstruction that ensures better uniformity in the flow distribution and that it is slightly deteriorated as a function of the number of reaction channels. As expected, an increase in the number of channels implies a larger mass flow into the reactor.

Figure 3-15(c) compares the $\sigma/\bar{M}$ for the velocity magnitude for the obstructed and free-flow configurations but bringing in the results of the 2-D simulations of the second stage. There is a clear discrepancy between the 2-D and 3-D results, especially for the free flow configurations. The reason is the friction effects generated by the top and bottom walls of the plate which are not considered in the 2-D approach which instead assume infinite height. These friction effects turn out to be relevant as they further favour a uniform flow distribution. Reducing the system to two dimensions relegates the results to a qualitative prediction and is therefore not recommended when an accurate sizing is the study aim.

In the last case analysed, the length of the reaction channels (L) is varied and the implications for the system are discussed. Increasing L results in a larger mass flow which, as expected, leads to a cumulative heat release explaining the temperature profile in Figure 3-16 (b). At the same time, the increase in temperature represents a slight increase in CO_2 conversion. Note that in this case, the transport resistances are the same regardless of L, since the design point defined in stage 1 applies equally to all channels. Another result is the pressure drop that naturally occurs with longer channels up to 2.25 pa for channels 175 mm long. The main outcome is the feasible increase of reactor throughput by enlarging the reaction channels without substantial negative repercussions, as hot spot formation, low product quality, pressure drop, or poor flow distribution.

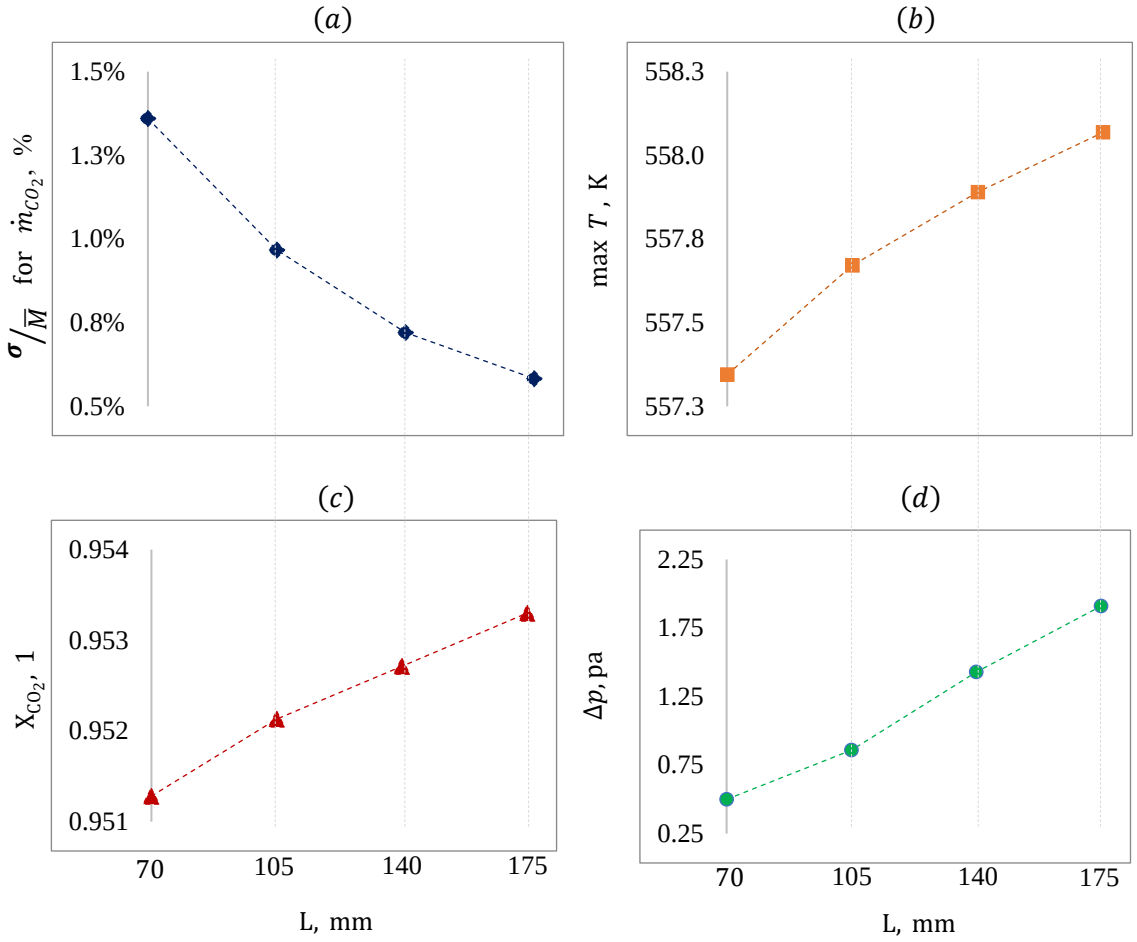

Figure 3-16. Effect of channel length on the mass flow standard deviation (a), maximum local temperature (b), CO_2 conversion (c) and pressure drop (d).

3.4.4 Dynamic analysis

A preliminary test was carried out to observe the previously designed system response within a dynamic environment. It was intended to illustrate a typical PtM catalytic unit case facing intermittency. The sudden start-up and shut-down of the operation were simulated using the inlet and coolant temperatures as interruption variables. Figure 3-17 shows the axial temperature profile (y-axis) over time (x-axis) for a single reaction channel with the dimensions previously established. The analysis is performed in milliseconds due to the short time of gas retention within the channel.

It is possible to analyse that the system suffers a natural heating as the gas temperature at the entrance increases along with the coolant temperature. Despite the rise, there are no hot spots along the axial direction, indicating that the speed of heat removal is sufficiently effective. The system stabilises near the second 0.035, reaching a temperature similar to that of the inlet. However, once

the temperature decreases due to the on-off disturbance at the reactor entrance, the system starts its cooling process. Based on the thermal map shown in Figure 3-17, where the cooling rate is qualitatively identical to the heating rate, it is fair to affirm that the system response does not depend on its history and therefore does not exhibit any hysteresis behaviour. Contrary to what has been reported in past studies in packed bed reactors with wrong-way responses [14]. Finally, a stationary state of extinction is reached after 0.05 s.

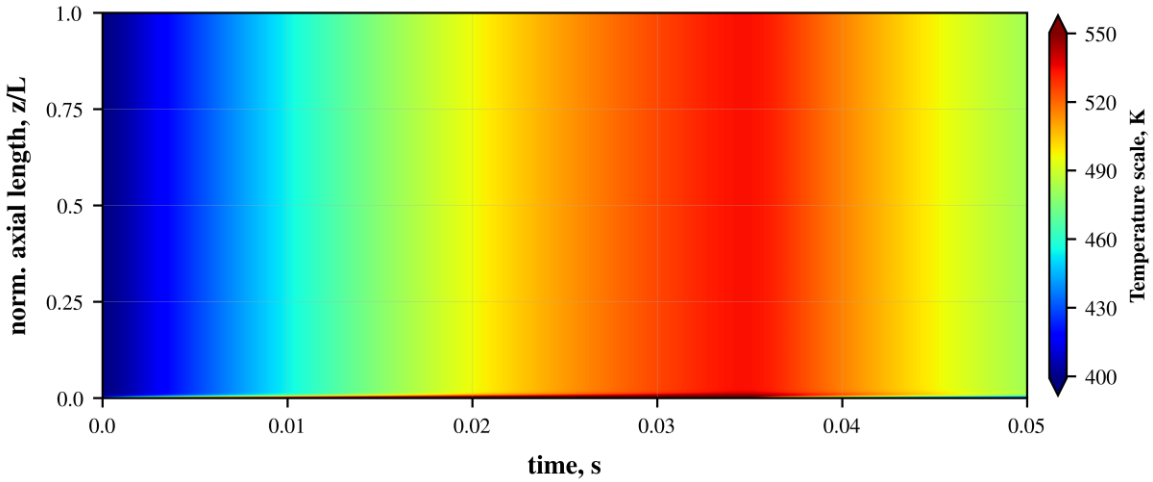

Figure 3-17. Dynamic simulation results, start-up of the reactor.

3.5 Conclusions

In this work, a conceptual design of an intensified reactor to produce synthetic natural gas in the context of PtM was developed. The structural design was subdivided into multiple stages, starting with a single reaction channel, following the stacked-plates and reaction network design. The first was intended to maximise reactor throughput while meeting a product quality requirement given by a CO_2 conversion above 95 %. The second aimed to find the manifold geometric parameters that most benefit a uniform flow distribution, a variable that was quantified based on the flow rate relative standard deviation.

The first stage concluded that the most favourable channel geometry, meaning the one that complies with the minimum quality threshold and the maximum throughput, was a reaction channel in the millimetre scale, with a catalytic layer of 300 μm and catalyst particles with 20 μm in diameter. From the second stage, it was possible to establish that the geometry that best encourages a uniform flow distribution is triangular (*Geo.1*). Furthermore, it was evident that placing a flow obstruction in the manifold has a considerably improved effect on fluid uniformity. The results of the second stage were also presented for stacked-plates with a different number of channels. In the last step, larger scale simulations for the entire 3-D stacked plate were performed

to validate the former results. Although important discrepancies were found when comparing the uniformity of flow distribution of 2-D and 3-D cases, the proposed configurations for different number of channels within the reacting network allowed to guarantee a final SNG quality on which its potential injection into the NG grid can be assessed. Besides, reactions channels length might be used as way of process scale-up strategy since it is shown no substantial negative effect until 175 mm in terms of heat management, SNG quality, pressure drop or flow distribution. Last, a preliminary dynamic analysis was conducted through the simulation of the operation start-up and shut-down. From this last analysis, it can be established that the designed reactor does not present a hysteresis behaviour and therefore, it would respond positively within an intermittent environment that requires a quick on and off.

As future work the proposed design of an intensified reactor for SNG production should be further developed. On the one hand, from a computational point of view, testing the system in a fully dynamic scenario that resembles the fluctuations to which PtM technologies are exposed in the industrial context. On the other hand, to experimentally validate the results of the computer-aided design. Without lab-scale validation, the conceptual design cannot be transformed into a prototype in which the intensification concept enhanced features can be exploited. The continuous improvement of PtM technologies must be pursued to fully integrate renewable energies with the energy grid in the future.

3.6 Nomenclature and abbreviations

Latin letters

x	x cartesian coordinate, [m]
y	y cartesian coordinate, [m]
z	z cartesian coordinate, [m]
t	Time, [s]
p	Pressure, [bar]
T	Temperature, [K]
w	Species mass fraction, [1]
y	Species molar fraction, [1]
C	Concentration, [mol m^{-3}]
u	Fluid velocity vector, [−]
j	Mass flux, [kg m^{-2} s^{-1}]
q	Heat flux, [W m^{-2}]
I	Identity matrix, [−]
n	Normal vector, [−]
R	Molar reaction rate, [mol m_{cat}^{-3} s^{-1}]
r	Mass-based reaction rate, [mol g_{cat}^{-1} s^{-1}]
M	Molar mass, [g mol^{-1}]

Subscripts

α	Chemical species: {H_2O, CO_2, H_2, CH_4}
j	Milli-channel index
mc	Milli-channel(s)
$mfld$	Manifold
Sab	Sabatier reaction
gas	Gas phase (mixture)
cat	Catalyst phase
bed	Fixed-bed domain
$wall$	Wall-coated layer
w	Reactor wall
cool	Coolant
free	Free reacting flow
ref	Reference
f	Feed

Abbreviations

v	Stoichiometrically coefficient, [1]
D	Diffusion coefficient, [m^2 s^{-1}]
k	Material permeability, [N/A^2]
d_p	Particle diameter, [m]
C_p	Specific heat capacity, [J kg^{-1} K^{-1}]
$\dot{m}$	Mass flow, [kg s^{-1}]
U_A	Heat transfer coefficient, [W m^{-2} K^{-1}]
h	Heat transfer coefficients, [W m^{-2} K^{-1}]
a_v	Specific particle surface area, [m^{-1}]
k	Reaction rate constant, [mol $bar^{-1}s^{-1}$ g_{cat}^{-1}]
K_{eq}	Equilibrium constant, [bar^{-2}]
K_x	Adsorption rate constant, [$bar^{-0.5}$]
R	Universal gas constant, [various]
E_A	Activation energy, [kJ mol^{-1}]
X	Chemical conversion, [1]
V	Reactor volume, [m^3]
A	Area, [m^2]
L	Reactor length, [m]
W	Width, [m]
H	Height, [m]
F	Flow rate velocity (magnitude), [m s^{-1}]
N	Number of channels per stacked-plate, [−]
f	Geometric parameter fraction, [1]

Superscripts

m	Mixture
eff	Effective
T	Transpose operator
int	Intrinsic

PtG	Power-to-Gas
PtM	Power-to-Methane
CCU	Carbon Capture and Utilization
SNG	Synthetic Natural Gas
PI	Process Intensification
CAD	Computer-Aided Design
CFD	Computational Fluid Dynamics
PDEs	Partial Differential Equations
LHHW	Langmuir-Hinshelwood-Hougen-Watson
GHSV	Gas Hourly Space Velocity
FEM	Finite Element Method

Greek letters

Ω	Mathematical domain, [−]
$\partial\Omega$	Domain boundaries, [−]
Γ	Boundary part, [−]
ρ	Density, [kg m^{-3}]
λ	Thermal conductivity, [W m^{-1} K^{-1}]
Θ	Void fraction, [1]
μ	Fluid dynamic viscosity, [Pa s]
ε	Catalyst bed porosity, [1]
$\Delta_R H$	Reaction enthalpy, [kJ mol^{-1}]
ΔH_X	Adsorption enthalpy, [kJ mol^{-1}]
γ	Heat transport coefficient, [W m^{-2} K^{-1}]
κ	Heat transport coefficient, [W m^{-1} K^{-1}]
δ	Domain thickness, [m]
η	Effectiveness factor, [1]
σ	Relative standard deviation, [1]

[−] refers to without units and [1] to dimensionless.

3.7 References

[2] T. Stocker, *Climate change 2013: the physical science basis: Working Group I contribution to the Fifth assessment report of the Intergovernmental Panel on Climate Change*. Cambridge university press, 2014.

[3] K. Ghaib, K. Nitz, and F.-Z. Ben-Fares, " Chemical Methanation of CO 2 : A Review ," *ChemBioEng Rev.*, vol. 3, no. 6, pp. 266–275, 2016.

[4] J. Uebbing, L. K. Rihko-Struckmann, and K. Sundmacher, "Exergetic assessment of CO2 methanation processes for the chemical storage of renewable energies," *Appl. Energy*, vol. 233–234, no. October 2018, pp. 271–282, 2019.

[5] M. Götz *et al.*, "Renewable Power-to-Gas: A technological and economic review," *Renew. Energy*, vol. 85, pp. 1371–1390, 2016.
[6] M. Lehner, R. Tichler, H. Steinmüller, and M. Koppe, *Power-to-gas: technology and business models*. Springer, 2014.
[7] R. Anghilante *et al.*, "Innovative power-to-gas plant concepts for upgrading of gasification bio-syngas through steam electrolysis and catalytic methanation," *Energy Convers. Manag.*, vol. 183, no. October 2018, pp. 462–473, 2019.
[8] K. Ghaib and F.-Z. Ben-Fares, "Power-to-Methane: A state-of-the-art review," *Renew. Sustain. Energy Rev.*, vol. 81, no. August 2017, pp. 433–446, Jan. 2018.
[9] R. Chauvy, L. Dubois, P. Lybaert, D. Thomas, and G. De Weireld, "Production of synthetic natural gas from industrial carbon dioxide," *Appl. Energy*, vol. 260, no. November 2019, p. 114249, 2020.
[10] X. Zhang, C. Bauer, C. L. Mutel, and K. Volkart, "Life Cycle Assessment of Power-to-Gas: Approaches, system variations and their environmental implications," *Appl. Energy*, vol. 190, pp. 326–338, 2017.
[11] W. L. Becker, M. Penev, and R. J. Braun, "Production of Synthetic Natural Gas From Carbon Dioxide and Renewably Generated Hydrogen: A Techno-Economic Analysis of a Power-to-Gas Strategy," *J. Energy Resour. Technol.*, vol. 141, no. 2, Feb. 2019.
[12] Strategieplattform Power to Gas, "Audi e-gas Projekt," 2019. [Online]. Available: https://www.powertogas.info/fr/projektkarte/audi-e-gas-projekt/. [Accessed: 09-Nov-2020].
[13] S. Rönsch *et al.*, "Review on methanation - From fundamentals to current projects," *Fuel*, vol. 166, pp. 276–296, 2016.
[14] R. T. Zimmermann, J. Bremer, and K. Sundmacher, "Optimal catalyst particle design for flexible fixed-bed CO2 methanation reactors," *Chem. Eng. J.*, vol. 387, no. July 2019, p. 123704, May 2020.
[14] D. Schlereth and O. Hinrichsen, "A fixed-bed reactor modeling study on the methanation of CO2," *Chem. Eng. Res. Des.*, vol. 92, no. 4, pp. 702–712, Apr. 2014.
[15] J. Bremer, K. H. G. Rätze, and K. Sundmacher, "CO 2 methanation: Optimal start-up control of a fixed-bed reactor for power-to-gas applications," *AIChE J.*, vol. 63, no. 1, pp. 23–31, Jan. 2017.
[16] J. Bremer and K. Sundmacher, "Operation range extension via hot-spot control for catalytic CO 2 methanation reactors," *React. Chem. Eng.*, vol. 4, no. 6, pp. 1019–1037, 2019.
[17] D. Sun and D. S. A. Simakov, "Thermal management of a Sabatier reactor for CO2 conversion into CH4: Simulation-based analysis," *J. CO2 Util.*, vol. 21, no. June, pp. 368–382, Oct. 2017.
[18] D. Sun, F. M. Khan, and D. S. A. Simakov, "Heat removal and catalyst deactivation in a Sabatier reactor for chemical fixation of CO 2 : Simulation-based analysis," *Chem. Eng. J.*, vol. 329, pp. 165–177, Dec. 2017.
[19] S. Ortiz-Laverde, C. Rengifo, M. Cobo, and M. Figueredo, "Proposal of an open-source computational toolbox for solving PDEs in the context of chemical reaction engineering using FEniCS and complementary components," *Heliyon*, vol. 7, no. 1, p. e05772, Jan. 2021.
[20] A. Fache, F. Marias, V. Guerré, and S. Palmade, "Optimization of fixed-bed methanation reactors: Safe and efficient operation under transient and steady-state conditions," *Chem. Eng. Sci.*, vol. 192, pp. 1124–1137, 2018.
[21] W. Zhang, H. Machida, H. Takano, K. Izumiya, and K. Norinaga, "Computational fluid dynamics simulation of CO2 methanation in a shell-and-tube reactor with multi-region conjugate heat transfer," *Chem. Eng. Sci.*, vol. 211, p. 115276, 2020.
[22] Y. Liu and O. Hinrichsen, "CFD Simulation of Hydrodynamics and Methanation Reactions in a Fluidized-Bed Reactor for the Production of Synthetic Natural Gas," *Ind. Eng. Chem. Res.*, vol. 53, no. 22, pp. 9348–9356, Jun. 2014.
[23] N. Engelbrecht, S. Chiuta, R. C. Everson, H. W. J. P. Neomagus, and D. G. Bessarabov, "Experimentation and CFD modelling of a microchannel reactor for carbon dioxide methanation," *Chem. Eng. J.*, vol. 313, pp. 847–857, Apr. 2017.

[24] M. Gruber *et al.*, "Modeling and Design of a Catalytic Wall Reactor for the Methanation of Carbon Dioxide," *Chemie-Ingenieur-Technik*, vol. 90, no. 5, pp. 615–624, 2018.
[25] F. Vidal Vázquez, J. Kihlman, A. Mylvaganam, P. Simell, M.-L. Koskinen-Soivi, and V. Alopaeus, "Modeling of nickel-based hydrotalcite catalyst coated on heat exchanger reactors for CO2 methanation," *Chem. Eng. J.*, vol. 349, no. April, pp. 694–707, Oct. 2018.
[26] B. Kreitz, G. D. Wehinger, and T. Turek, "Dynamic simulation of the CO2 methanation in a micro-structured fixed-bed reactor," *Chem. Eng. Sci.*, vol. 195, pp. 541–552, Feb. 2019.
[27] C. Jia, Y. Dai, Y. Yang, and J. W. Chew, "A fluidized-bed model for NiMgW-catalyzed CO2 methanation," *Particuology*, vol. 49, pp. 55–64, Apr. 2020.
[28] S. Farsi, W. Olbrich, P. Pfeifer, and R. Dittmeyer, "A consecutive methanation scheme for conversion of CO2 – A study on Ni3Fe catalyst in a short-contact time micro packed bed reactor," *Chem. Eng. J.*, vol. 388, no. February, p. 124233, May 2020.
[29] J. Lefebvre, S. Bajohr, and T. Kolb, "Modeling of the transient behavior of a slurry bubble column reactor for CO2 methanation, and comparison with a tube bundle reactor," *Renew. Energy*, vol. 151, pp. 118–136, May 2020.
[30] S. I. Ngo, Y.-I. Lim, D. Lee, K. S. Go, and M. W. Seo, "Flow behaviors, reaction kinetics, and optimal design of fixed- and fluidized-beds for CO2 methanation," *Fuel*, vol. 275, no. March, p. 117886, Sep. 2020.
[31] I. Coronado Martín, "Carbon dioxide methanation for intensified reactors."
[32] J. Li, R. K. Agarwal, L. Zhou, and B. Yang, "Investigation of a bubbling fluidized bed methanation reactor by using CFD-DEM and approximate image processing method," *Chem. Eng. Sci.*, vol. 207, pp. 1107–1120, 2019.
[33] W. Ehrfeld, V. Hessel, and H. Löwe, *Microreactors*. Wiley, 2000.
[34] H. Freund and K. Sundmacher, "Process Intensification, 3. Process Unit Level," in *Ullmann's Encyclopedia of Industrial Chemistry*, Weinheim, Germany: Wiley-VCH Verlag GmbH & Co. KGaA, 2011, pp. 1–24.
[35] A. Adamu, F. Russo-Abegão, and K. Boodhoo, "Process intensification technologies for CO2 capture and conversion – a review," *BMC Chem. Eng.*, vol. 2, no. 1, p. 2, Dec. 2020.
[36] O. Wörz, K. P. Jäckel, T. Richter, and A. Wolf, "Microreactors, a new efficient tool for optimum reactor design," *Chem. Eng. Sci.*, vol. 56, no. 3, pp. 1029–1033, Feb. 2001.
[37] J. Némethné-Sóvágó and M. Benke, "Microreactors: a new concept for chemical synthesis and technological feasibility," *Mater. Sci. Eng.*, vol. 39, no. 2, pp. 89–101, 2014.
[38] K. GOLBIG, A. KURSAWE, M. HOHMANN, S. TAGHAVI-MOGHADAM, and T. SCHWALBE, "Designing Microreactors in Chemical Synthesis – Residence-time Distribution of Microchannel Devices," *Chem. Eng. Commun.*, vol. 192, no. 5, pp. 620–629, Jan. 2005.
[39] F. J. Keil, "Process intensification," *Rev. Chem. Eng.*, vol. 34, no. 2, pp. 135–200, Feb. 2018.
[40] M. N. Kashid and L. Kiwi-Minsker, "Microstructured Reactors for Multiphase Reactions: State of the Art," *Ind. Eng. Chem. Res.*, vol. 48, no. 14, pp. 6465–6485, Jul. 2009.
[41] P. L. Suryawanshi, S. P. Gumfekar, B. A. Bhanvase, S. H. Sonawane, and M. S. Pimplapure, "A review on microreactors: Reactor fabrication, design, and cutting-edge applications," *Chem. Eng. Sci.*, vol. 189, pp. 431–448, Nov. 2018.
[42] T. Koiranen, M. Woldemariam, and A. Salminen, "Reactor Performance and Design Concept in Additively Manufactured Milli-Scale Reactors," *J. Chem. Eng. Process Technol.*, vol. 08, no. 05, 2017.
[43] I. Rossetti and M. Compagnoni, "Chemical reaction engineering, process design and scale-up issues at the frontier of synthesis: Flow chemistry," *Chem. Eng. J.*, vol. 296, pp. 56–70, Jul. 2016.
[44] J. Zhang, K. Wang, A. R. Teixeira, K. F. Jensen, and G. Luo, "Design and Scaling Up of Microchemical Systems: A Review," *Annu. Rev. Chem. Biomol. Eng.*, vol. 8, no. 1, pp. 285–305, Jun. 2017.

[45] K. P. Brooks, J. Hu, H. Zhu, and R. J. Kee, "Methanation of carbon dioxide by hydrogen reduction using the Sabatier process in microchannel reactors," *Chem. Eng. Sci.*, vol. 62, no. 4, pp. 1161–1170, Feb. 2007.

[46] J. Oliveira de Brito Lira, H. G. Riella, N. Padoin, and C. Soares, "An Overview of Photoreactors and Computational Modeling for the Intensification of Photocatalytic Processes in the Gas-Phase: State-of-Art," *J. Environ. Chem. Eng.*, vol. 9, no. 2, p. 105068, 2021.

[47] A. B. Hamzah, T. Fukuda, S. Ookawara, S. Yoshikawa, and H. Matsumoto, "Process intensification of dry reforming of methane by structured catalytic wall-plate microreactor," *Chem. Eng. J.*, vol. 412, no. October 2020, p. 128636, 2021.

[48] R. J. Kee, M. E. Coltrin, and P. Glarborg, "Molecular Transport," in *Chemically Reacting Flow*, Hoboken, NJ, USA: John Wiley & Sons, Inc., 2005, pp. 487–539.

[49] E. N. Fuller, P. D. Schettler, and J. C. Giddings, "A new method for prediction of binary gas-phase diffusion coefficients," *Ind. Eng. Chem.*, vol. 58, no. 5, pp. 18–27, May 1966.

[50] B. E. Poling, J. M. Prausnitz, and J. P. O'Connell, *Properties of Gases and Liquids, Fifth Edition*. New York: McGraw-Hill Education, 2001.

[51] F. Koschany, D. Schlereth, and O. Hinrichsen, "On the kinetics of the methanation of carbon dioxide on coprecipitated NiAl(O)<inf>x</inf>," *Appl. Catal. B Environ.*, vol. 181, pp. 504–516, 2016.

[52] S. Chiuta and D. G. Bessarabov, "Design and operation of an ammonia-fueled microchannel reactor for autothermal hydrogen production," *Catal. Today*, vol. 310, no. January 2017, pp. 187–194, Jul. 2018.

[53] VDI, *VDI Heat Atlas*. Berlin, Heidelberg: Springer Berlin Heidelberg, 2010.

[54] D. S. A. Simakov and M. Sheintuch, "Model-based optimization of hydrogen generation by methane steam reforming in autothermal packed-bed membrane reformer," *AIChE J.*, vol. 57, no. 2, pp. 525–541, Feb. 2011.

[55] J. Gao *et al.*, "A thermodynamic analysis of methanation reactions of carbon oxides for the production of synthetic natural gas," *RSC Adv.*, vol. 2, no. 6, p. 2358, 2012.

[56] L. M. Aparicio, "Transient isotopic studies and microkinetic modeling of methane reforming over nickel catalysts," *J. Catal.*, vol. 165, no. 2, pp. 262–274, 1997.

[57] N. Jurtz, M. Kraume, and G. D. Wehinger, "Advances in fixed-bed reactor modeling using particle-resolved computational fluid dynamics (CFD)," *Rev. Chem. Eng.*, vol. 35, no. 2, pp. 139–190, Feb. 2019.

[58] G. D. Wehinger, F. Klippel, and M. Kraume, "Modeling pore processes for particle-resolved CFD simulations of catalytic fixed-bed reactors," *Comput. Chem. Eng.*, vol. 101, pp. 11–22, Jun. 2017.

[59] T. J. Schildhauer and S. M. A. Biollaz, "Synthetic Natural Gas: From Coal, Dry Biomass, and Power-to-Gas Applications," *Focus Catal.*, vol. 2016, no. 8, p. 7, Aug. 2016.

[60] S. Odiba, M. Olea, S. Hodgson, and A. Adgar, "Computational Fluid Dynamics for Microreactors Used in Catalytic Oxidation of Propane," *Proceeding 2013 COMSOL Bost.*, vol. 2, 2014.

CONCLUDING REMARKS

This manuscript addressed the CO_2 methanation in the carbon capture and utilisation context from the reaction technologies standpoint.

Firstly, the subject of dynamic hot spot formation in fixed bed reactors, used on an industrial scale, was discussed based on a parametric sensitivity study. This analysis made it easier to comprehend the remaining obstacles to be overcome to improve the power-to-methane model's competitiveness in the energy market. Secondly, the conceptual design of a heat-exchanger wall-coated reactor was proposed following a process intensification strategy. Computational fluid dynamics simulations assisted the design. It was possible to define the reacting channel dimensions, offering the best performance in terms of CO_2 conversion and SNG throughput. The effect of multiple geometric parameters of the plate manifold on flow distribution was also analysed. Finally, it was established that the reactor does not present a hysteresis behaviour after a preliminary dynamic test.

All the reported resulted from the numerical analysis of phenomenological transient/stationary models, using the finite element method through commercial and open-source software, such as COMSOL Multiphysics® and the FEniCS Project, respectively.

FUTURE WORK

The use of computational tools based on open-source software allows greater flexibility for numerical and computational implementation. This also provides a more extensive and successful learning curve over the typical black-boxes. Nevertheless, these alternatives must be strengthened to overcome some of their weaknesses concerning computational robustness in distinct scenarios. For instance, the application of FEniCS combined with the complementary python modules should be extended to problems in which distinct domain and phenomenological equations need to be coupled and solved.

Moreover, the proposed design of an intensified reactor for SNG production should be further developed. On the one hand, from a computational point of view, testing the system in a fully dynamic scenario that resembles the fluctuations to which PtM technologies are exposed in the industrial context. On the other hand, to experimentally validate the results of the computer-aided design. Without lab-scale validation, the conceptual design cannot be transformed into a prototype in which the intensification concept enhanced features can be exploited. The continuous improvement of PtM technologies must be pursued to fully integrate renewable energies with the energy grid in the future.

APPENDIX A: Supplementary Material for: Proposal of an open-source computational toolbox for solving PDEs in the context of chemical reaction engineering using FEniCS and complementary components

A.1 Supplementary material – Case study 1

The reader is encouraged to solve the first case study as a way of training in the application of the described computational toolbox. Accordingly, the supplementary material for this case study is intended to detail the information that was not placed in the main document, and that is required to replicate the discussed results.

A.1.1 Parameters and physical properties

The o-xylene oxidation to phthalic anhydride (Eq. (A.1)) can be considered irreversible with an excess of oxygen and which reaction rate is calculated via Eq. (A.2):

$$C_8H_{10} + 3O_2 \rightarrow C_8H_4O_3 + 3H_2O, \tag{A.1}$$

$$r_{oxy} = \exp\left(\alpha - \frac{\beta}{T}\right) C_a C_b \frac{(\mathrm{R}T)^2}{\varsigma}. \tag{A.2}$$

α and β are kinetic parameters, and ς is a unit conversion factor. These and other parameters, such as coolant/reacting flow physical properties, reactor dimensions, and operating conditions, are stated in Table A-1. Note that the subscripts a and b refer to the reagents o–xylene and oxygen, respectively.

Table A-1. Parameters for case study 1 (adapted from [1]).

Parameter	Value	Parameter	Value
p_{a_f}	0.011[bar]	D^{eff}	0.01 [$m^2\ s^{-1}$]
p_{b_f}	0.211[bar]	λ^{eff}	0.6 [$W\ m^{-1}\ K^{-1}$]
T_f	625 [K]	$\boldsymbol{\vartheta}$	(0.0, ~0.88) [$m\ s^{-1}$]
R	0.0127 [m]	ρ_{gas}	1.293 [$kg\ m^{-3}$]
L	3 [m]	$C_{p_{gas}}$	992 [$J\ kg^{-1}\ K^{-1}$]
V	~ 3x10^{-3} [m^3]	ρ_b	1300 [$kg\ m^{-3}$]
$\Delta_R H_{oxy}$	− 1284488 [$J\ mol^{-1}$]	$T_{cool,f}$	625 [K]
α	19.837 [1]	F_{cool}	0.1 [$kg\ s^{-1}$]
β	13636 [K]	ρ_{cool}	1000 [$kg\ m^{-3}$]
ς	3.60x10^{10} [$mol\ J^{-1}\ m^3\ s^{-1}$]	$C_{p_{cool}}$	4200 [$J\ kg^{-1}\ K^{-1}$]
ε	0.35 [1]	U_w	96 [$W\ m^{-2}\ K^{-1}$]

[1] refers to dimensionless.

A.1.2 Variational formulation

The variational problem for the mathematical model used in the first case study is detailed in Table A-2. Unlike the second case study, this model considers Danckwert's boundary conditions for the composition and temperature at the entrance of the reactor. Since these are Robin-type, they must be included in the formulation, and just as with the other case, the rest of boundary conditions (Dirichlet and natural Neuman) are vanishes in the formulation but fitted to the corresponding $\partial\Omega$ through FEniCS abstractions in the python program. The reader is encouraged to examine the FEniCS and ACM source codes committed to a public repository on GitHub (here).

Table A-2. Variational formulation for governing Eqs. (2.4)-(2.5) tied down to boundary conditions described by Eqs. (2.7)-(2.8).

Description	Mathematical expression	Eq.
V.F. for the species mass transport equation	$\mathrm{F}_i^{n+1}(C_i;\, v_i) = \int_\Omega \left(\frac{C_i^{n+1} - C_i^{n}}{\Delta t}\right) v_i \, dx + \left(\boldsymbol{\vartheta} \cdot \vec{\nabla} C_i\right)^{n+1} v_i \, dx$ $- \int_\Omega \left(v_{i,\,oxy}\, \rho_b\, r_{oxy}\right)^{n+1} v_i \, dx + \int_\Omega \left(\varepsilon\, D^{eff}\, \left(\vec{\nabla} C_i \cdot \vec{\nabla} v_i\right)\right)^{n+1} dx$ $+ \oint_{\partial\Omega} \vartheta_z \left(C_i - C_{i,f}\right) v_i \, ds$	(A.3)
V.F. for the energy transport equation	$\mathrm{F}_T^{n+1}(T;\, v_T) = \int_\Omega \left(\rho\, \mathrm{C_p}\right)_{gas} \left(\frac{T^{n+1} - T^{n}}{\Delta t}\right) v_T \, dx + \int_\Omega \left(\boldsymbol{\vartheta} \cdot \vec{\nabla} T\right)^{n+1} v_T \, dx$ $+ \int_\Omega \rho_b \left(\Delta_R H_{oxy}\, r_{oxy}\right)^{n+1} v_T \, dx + \int_\Omega \left(\lambda^{eff} \left(\vec{\nabla} T \cdot \vec{\nabla} v_T\right)\right)^{n+1} dx$ $+ \oint_{\partial\Omega} \left(\rho\, \mathrm{C_p}\right)_{gas} \vartheta_z \left(T - T_f\right) v_T \, ds_f \; - \oint_{\partial\Omega} U_w \left(T_{cool} \; - \; T\right) v_T \, ds_w$	(A.4)
Global V.F. statement	$\mathrm{F}^{n+1}(C_i;\, T;\, v) = \sum_i \mathrm{F}_i^{n+1}(C_i;\, v_i) + \mathrm{F}_T^{n+1}(T;\, v_T) \quad in \quad \Omega$	(A.5)

V.F. refers to Variational Formulation

A.1.3 2-D interpolation graphs

The fine triangular mesh generated by Gmsh-pygmsh and used for the FEniCS calculations was turned into a square mesh of the same dimensions as the ACM one (made of quadrilateral elements). This conversion enables to operate equivalent nodes from both meshes, for instance through Eq. (22) giving place to an absolute error as comparison criterion. Thus, a grid formed by quadrilateral elements was intersected with the triangular mesh, and the nodes were averaged within each square element. This approach is accurate if the averaged values within each element reflect a low coefficient of variation (CV), as indeed is represented in Figure A-1 with no CV above 1 %.

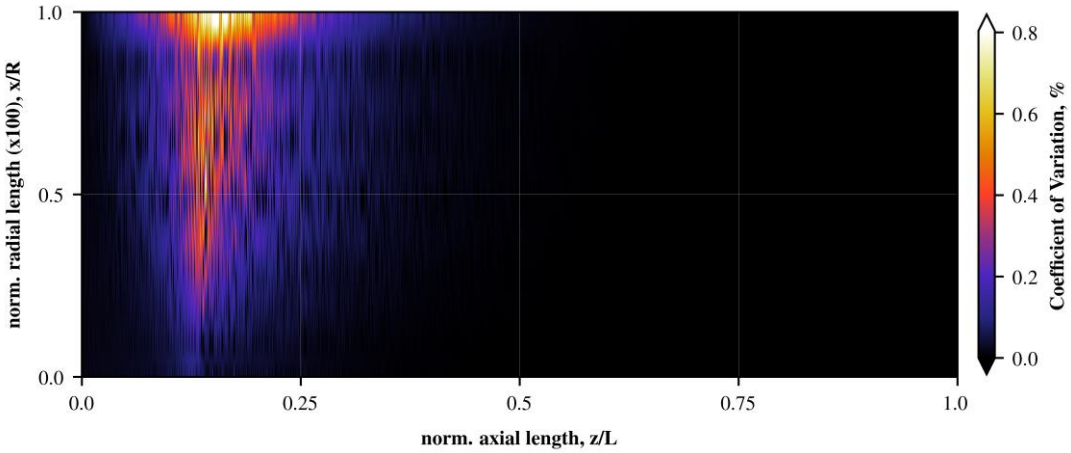

Figure A-1. 2-D profile for the coefficient of variation of averaged values per quadrilateral element.

Moreover, the resulted packed-bed thermal maps from both FEniCS and ACM computations are also presented as supplementary material and shown in Figure A-2 and Figure A-3, respectively.

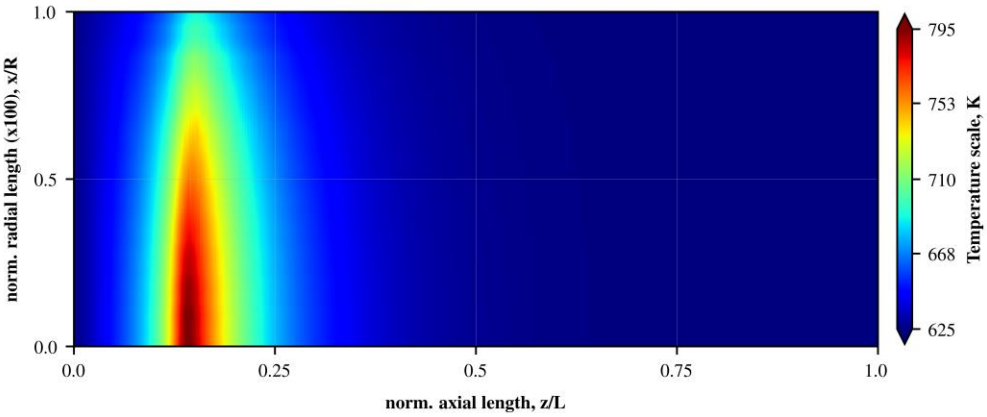

Figure A-2. Temperature profile of the packed-bed obtained by FEniCS.

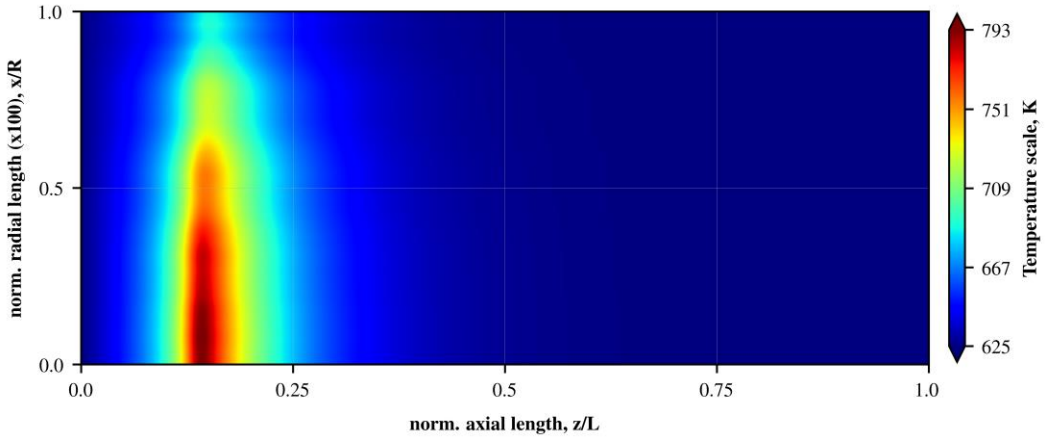

Figure A-3. Temperature profile of the packed-bed obtained by ACM.

A.2 Supplementary material – Case study 2

This section provides complementary information for the second study case on SNG production through CO_2 methanation.

Table A-3. Dimensions used for the fixed-bed reactor (single tube), constant operating conditions in simulation and catalyst ($NiAl(O)_x$) properties.

Parameter	Value
R	0.01 [m]
L	5 [m]
ε	0.4
T_f	400 [K]
U_w	450
λ_{cat}	0.15 [W m^{-1} K^{-1}]
$C_{p_{cat}}$	1107 [J Kg^{-1} K^{-1}]
ρ_{cat}	2300 [Kg m^{-3}]
d_p	0.002 [m]
ς	1000 ρ_{cat} [g m^{-3}]

A.2.1 Reaction rate equations and parameters

The conditions under which the employed rate model was parameterized were temperatures of 453−613 K, and pressures between 1 and 15 bar (at stoichiometric and non-stoichiometric feeds). Table A-4 resumes kinetic, adsorption, and equilibrium temperature-dependent constants. The equilibrium expression is an empirical correlation [2], but could be alternatively calculated by the Shomate equation [3], based on the species enthalpies, entropies and data provided by NIST Chemistry WebBook.

Table A-4. Temperature-dependent expression for rate model base on $NiAl(O)_x$ (see Koschany et al. (2016)).

Temperature-dependent constants	Mathematical expression	Eq.
Kinetic	$k_x(T) = k_{x,Tref}\, exp\left(\frac{E_A}{R}\left(\frac{1}{T_{ref}} - \frac{1}{T}\right)\right)$	(A.6)
Adsorption	$K_x(T) = K_{x,Tref}\, exp\left(\frac{\Delta H_x}{R}\left(\frac{1}{T_{ref}} - \frac{1}{T}\right)\right)$	(A.7)
Equilibrium	$K_{eq}(T) = 137\, T^{-3.998} exp\left(\frac{158.7\ kJ\ mol^{-1}}{R\,T}\right)$	(A.8)

Table A-5 lists the corresponding parametrization for equations in Table A-4.

Table A-5. Parametrization for Koschany et al. (2016) catalytic rate equation (T_{ref} = 555 K).

Kinetic parameter	Value
$k_{0,Tref}$	3.46e-4 [mol (bar s g_{cat})$^{-1}$]
E_A	77.5 [kJ mol^{-1}]
$K_{OH,Tref}$	0.50 [bar$^{-0.5}$]
ΔH_{OH}	22.4 [kJ mol^{-1}]
$K_{H_2,Tref}$	0.44 [bar$^{-0.5}$]
ΔH_{H_2}	− 6.2 [kJ mol^{-1}]
$K_{mix,Tref}$	0.88 [bar$^{-0.5}$]
ΔH_{mix}	− 10.0 [kJ mol^{-1}]

A.2.2 Dispersion effective coefficients

An approach proposed by Tsotsas and Schlünder (1988) was used to calculate the effective mass dispersion coefficient for each specie (D_i^{eff}) via Eq. (A.9), [4]. The mixture averaged diffusion coefficients (D_i^{m}) are calculated in Eq. (A.10) according to Kee et. al. (2004) [5], and the binary diffusion coefficients through the theoretical-empirical expression introduced by Fuller et al. (1966) via Eq. (A.11), [6].

$$D_i^{eff} = \left(1 - \sqrt{1-\varepsilon}\right) D_i^{m} + \frac{\mathrm{d_p}\,\vartheta_z}{8} \tag{A.9}$$

$$D_i^{m} = \frac{C_{gas} - C_i}{\sum_{k \neq i} \frac{C_k}{D_{i,k}}} \tag{A.10}$$

$$D_{i,k} = \frac{10^{-7} T^{1.75} \sqrt{10^3 \left({}^1/_{M_i} + {}^1/_{M_K}\right)}}{\left({}^p/_{1.01325}\right)\left[\sqrt[3]{\omega_i} + \sqrt[3]{\omega_k}\right]^2} \tag{A.11}$$

For the calculation of the effective heat dispersion coefficient, a model published by Bauer and Schlunder (1978a, 1978b) was employed [7], [8]. This approach combines the influence of the axial convective transport, radiation, and actual conduction, as follows:

$$\lambda^{eff} = \lambda_{convection} + \lambda_{conduction,\,radiation} \tag{A.12}$$

$$\lambda_{convection} = \frac{\rho_{gas}\,\vartheta_z\,\mathrm{C_p}_{gas}\,1.15\,\mathrm{d_p}}{8\left[2 - \left(1 - {}^{\mathrm{d_p}}/_{\mathrm{R}}\right)^2\right]} \tag{A.13}$$

$$\lambda_{conduction,\,radiation} = \left(1 - \sqrt{1-\varepsilon}\right)\left(\lambda_{gas} + \varepsilon\,\lambda_{radiation}\right) + \lambda_{\mathrm{rs}}\sqrt{1-\varepsilon} \tag{A.14}$$

$$\lambda_{radiation} = 2.27 \cdot 10^{-7} \frac{e_{cat}}{2 - e_{cat}}\, T^3\, \mathrm{d_p} \tag{A.15}$$

Further details on the computation of the parameter λ_{rs} and the gas mixture conductivity (λ_{gas}) may be found in [9] and [10]. The emissivity of the catalyst pellets (e_{cat}) was assumed to be 0.4.

A.2.3 Complementary figures

The following (Figure A-4 to Figure A-6) are complementary plots for the parametric sensitivity analysis discussed in the manuscript. An increase in the H_2:CO_2 molar ratio enhances the thermal conductivity of the gas mixture as well as its specific heat capacity, see Figure A-4. At first sight, it should raise the effective conductivity of the system judging by Eqs. (A.13)-(A.14). Nevertheless, the effective conductivity drops, as shown in Figure A-5. This decline is due to a more significant influence of the gas mixture density, which has a directly proportional effect on the contribution by convective transport, as stated in Eq. (A.13).

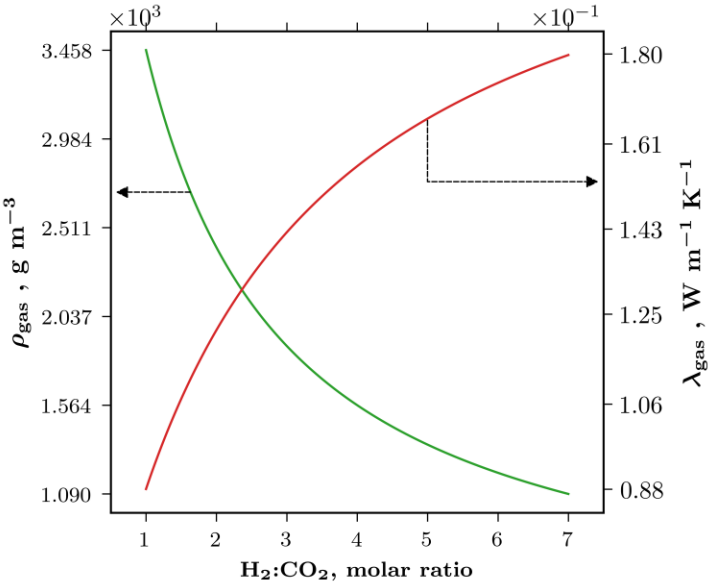

Figure A-4. Density and conductivity of the gas mixture as a function of the feed molar ratio (at 400 K and 5 bar).

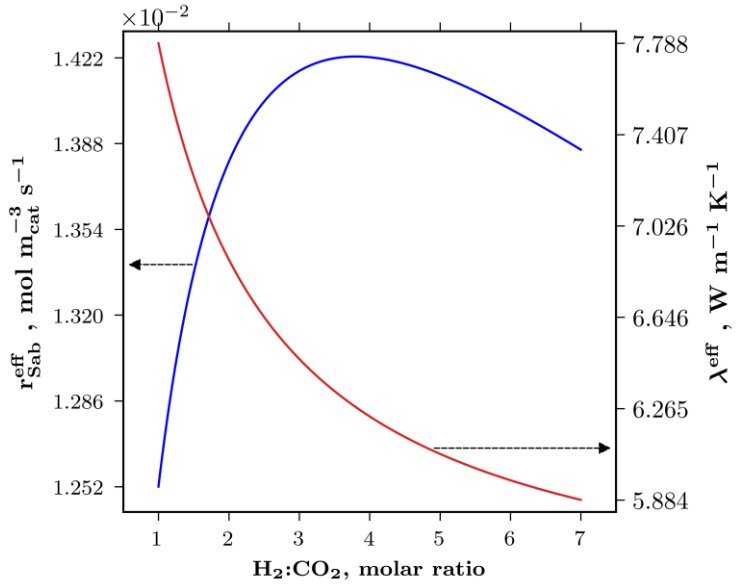

Figure A-5. Effective reaction rate and conductivity as a function of the feed molar ratio (at 400 K and 5 bar).

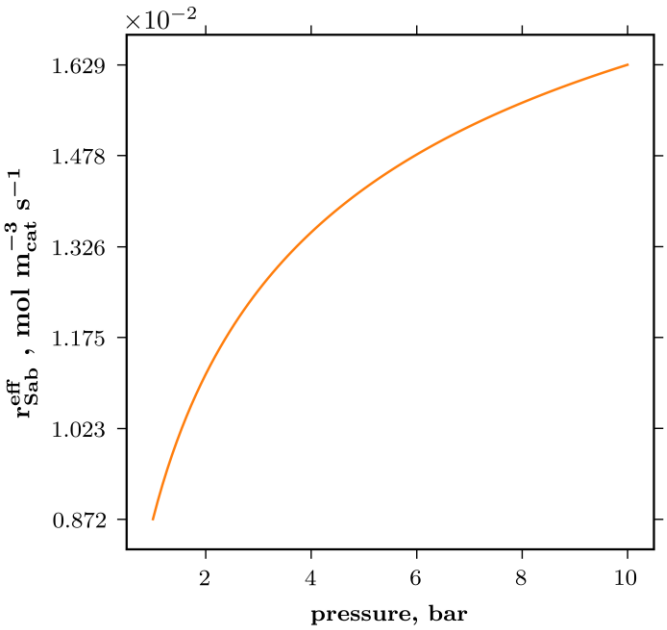

Figure A-6. Effective reaction rate as a function of pressure (at 400 K and H_2/CO_2 molar ratio of 4)

APPENDIX B: Supplementary Material for: CFD-aided conceptual design of an intensified reactor for the production of synthetic natural gas within the power-to-methane context

B.1 Wall-coated layer, catalyst and coolant properties

The parameters used in the mathematical model regarding the catalyst and coolant transport properties plus, the porosity for the case of the catalytic layer are given in the Table B-1.

Table B-1. Summary of catalyst, coolant and wall-coated properties.

Parameter	Value	Unit
λ_{cat}	3.6	W m^{-1} K^{-1}
ρ_{cat}	2350	kg m^{-3}
ε	0.5	
λ_{ss}	18	W m^{-1} K^{-1}
ρ_{cool}	858	kg m^{-3}
$C_{p,\,cool}$	2520	J kg^{-1} K^{-1}
λ_{cool}	0.096	W m^{-1} K^{-1}
μ_{cool}	0.43E–3	Pa s

B.2 Heat transfer coefficients calculation

Below is the procedure for the calculation of the respective heat transfer coefficients affiliated to the multiplicity of regions involved in the reactor. Specific particle surface area, and mass and heat-transfer coefficients are calculated by the correlations of Wakao and coworkers [11]. Heat capacities, heat conductivities and viscosities of the pure components are calculated as given in the VDI-Heat Atlas [12]. The latter are also averaged according to the Wilke mixing rule. The catalyst and coolant properties are summarized in Table B-1.

$$a_v = 6\frac{1-\varepsilon}{d_p} \tag{B.1}$$

$$k_{CO_2} = \frac{D^{\mathrm{m}}_{\mathrm{CO_2}}}{d_p}\left[2 + 1.1\left(\frac{\mu_{gas}}{\rho_{gas} D^{\mathrm{m}}_{\mathrm{CO_2}}}\right)^{1/3}\left(\frac{\mathrm{F_f}\,\rho_{gas}\,d_p}{\mu_{gas}}\right)^{0.6}\right] \tag{B.2}$$

$$h = \frac{\lambda_{gas}}{d_p}\left[2 + 1.1\left(\frac{C_{p,\,gas}\,\mu_{gas}}{\lambda_{gas}}\right)^{1/3}\left(\frac{\mathrm{F_f}\,\rho_{gas}\,d_p}{\mu_{gas}}\right)^{0.6}\right] \tag{B.3}$$

α_w-Model: Calculation of the heat transfer coefficient at the catalytic layer.

$$Pr = \frac{C_{p,\,gas}\,\mu_{gas}}{\lambda_{gas}}, \qquad Re = \frac{\rho_{gas}\,\mathrm{F}\,d_p}{\mu_{gas}} \tag{B.4}$$

$$\frac{\lambda_{bed}}{\lambda_{gas}} = 1 + \sqrt{1-\varepsilon}(\kappa_c - 1) \tag{B.5}$$

$$\kappa_p = \frac{\lambda_{cat}}{\lambda_{gas}}, \quad B = 1.25\left(\frac{1-\varepsilon}{\varepsilon}\right)^{10/9}, \quad N = 1 - \frac{B}{\kappa_p} \tag{B.6}$$

$$\kappa_c = \frac{2}{N}\left(\frac{B}{N^2}\frac{\kappa_p - 1}{\kappa_p}\ln\left(\frac{\kappa_p}{B}\right) - \frac{B+1}{2} - \frac{B-1}{N}\right) \tag{B.7}$$

$$Nu = \left(1.3 + \frac{5\,d_p}{\delta_{cat}}\right)\frac{\lambda_{bed}}{\lambda_{gas}} + 0.19Re^{0.75}Pr^{0.33} \tag{B.8}$$

$$\gamma_w = \frac{Nu\,\lambda_{gas}}{d_p} \tag{B.9}$$

γ_{fluid}-model: Calculation of the heat transfer coefficient for the coolant or reacting free flow.

$$\boldsymbol{\varphi} = \text{cool/free} \tag{B.10}$$

$$d_{h,\,\text{cool}} = 2\,\text{H}_{mc} \quad d_{h,\,\text{free}} = 2\,(\text{H}_{mc} - \delta_{cat}) \tag{B.11}$$

$$\gamma_{\boldsymbol{\varphi}} = \frac{Nu_m\,\lambda_{gas,\boldsymbol{\varphi}}}{d_{h,\boldsymbol{\varphi}}}, \quad Pr = \frac{C_{p,gas,\boldsymbol{\varphi}}\,\mu_{gas,\boldsymbol{\varphi}}}{\lambda_{gas,\boldsymbol{\varphi}}}, \quad Re = \frac{\rho_{gas,\boldsymbol{\varphi}}\,\text{F}_{gas,\boldsymbol{\varphi}}\,d_{h,\boldsymbol{\varphi}}}{\mu_{gas,\boldsymbol{\varphi}}} \tag{B.12}$$

The Nusselt number is estimated for the coolant fluid, assuming fully hydrodynamic and thermal developed conditions, given by Eq. (B.15). Furthermore, The Nusselt number is estimated for the reacting free flow assuming a laminar hydrodynamic and thermal development flow, given by Eq. (B.16).

$$Nu_1 = 7.541 \tag{B.13}$$

$$Nu_2 = 1.841\sqrt[3]{\frac{Re\,\text{Pr}\,d_{h,\boldsymbol{\varphi}}}{L}} \tag{B.14}$$

$$Nu_m = \left({Nu_1}^3 + {Nu_2}^3\right)^{1/3} \tag{B.15}$$

$$Nu_m = 7.55 + \frac{0.024\left(\frac{Re\,\text{Pr}\,d_{h,\boldsymbol{\varphi}}}{L}\right)^{1.14}}{1 + 0.0358\left(\frac{Re\,\text{Pr}\,d_{h,\boldsymbol{\varphi}}}{L}\right)^{0.64}Pr^{0.17}} \tag{B.16}$$

κ_{wall}-model: Calculation of the heat transfer coefficient at the reactor wall (ss = stainless steel).

$$\kappa_{wall} = \left(\frac{1}{\lambda_{ss}}ln\left(\frac{\frac{\text{H}_{mc}}{2} + \delta_{wall}}{\frac{\text{H}_{mc}}{2}}\right)\right)^{-1} \tag{B.17}$$

B.3 Catalyst diffusion limitations

The predominant resistance is the diffusion from the fluid bulk towards the porous medium as a function of the wall-coated layer thickness and is expressed through the dispersion coefficient in Table 3-1. However, there might be intraparticle transport resistances that depends mainly on the particle size as described by the well-known Weisz-Prater, Anderson, and Mears criteria, summarised in Table B-2.

Table B-2. Criteria for intraparticle transport resistances.

Description	Mathematical expression	Eq.
Intraparticle mass transport — Weisz-Prater criterion	$\frac{\mathrm{r}^{\mathrm{eff}}\ {d_p}^2}{4\ \mathrm{C}_{\mathrm{CO_2}}\ D_{\mathrm{CO_2}}^{\mathrm{eff}}} < 1$	(B.18)
Intraparticle heat transport — Anderson criterion	$\frac{\mathrm{r}^{\mathrm{eff}}\ \lvert\Delta_R H\rvert\ {d_p}^2}{4\ \lambda^{\mathrm{eff}}\ T} < \frac{0.75\ \mathrm{R}\ T}{E_A}$	(B.19)
External mass transport — Mears criterion	$\frac{\mathrm{r}^{\mathrm{eff}}}{h_{\mathrm{CO_2}}\ \mathrm{C}_{\mathrm{CO_2}}\ a_v} < 0.05$	(B.20)
External heat transport — Mears criterion	$\frac{\mathrm{r}^{\mathrm{eff}}\ \lvert\Delta_R H\rvert}{h\ T\ a_v} < \frac{0.05\ \mathrm{R}\ T}{E_A}$	(B.21)

The particle size was evaluated from 5 to 50 μm, a range in which, as shown in Figure B-1 and Figure B-2, there are no significant mass and heat transport resistances. Therefore, the intraparticle constraints can be negligible.

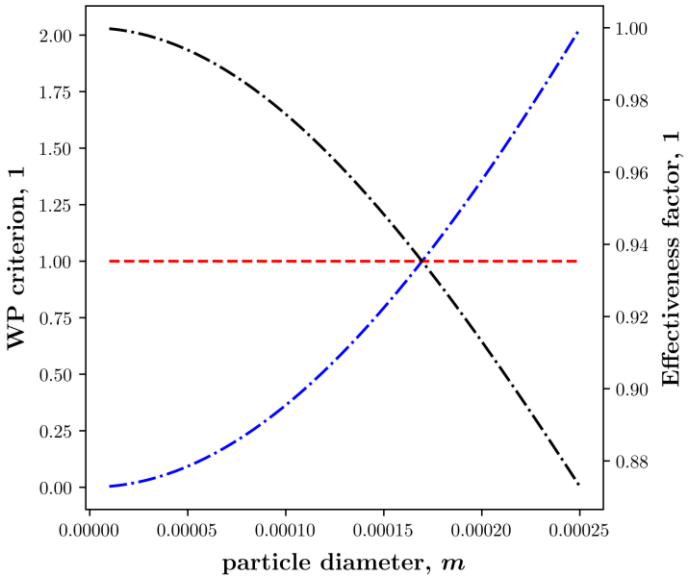

Figure B-1. Mass-transport resistances as function of the particle diameter.

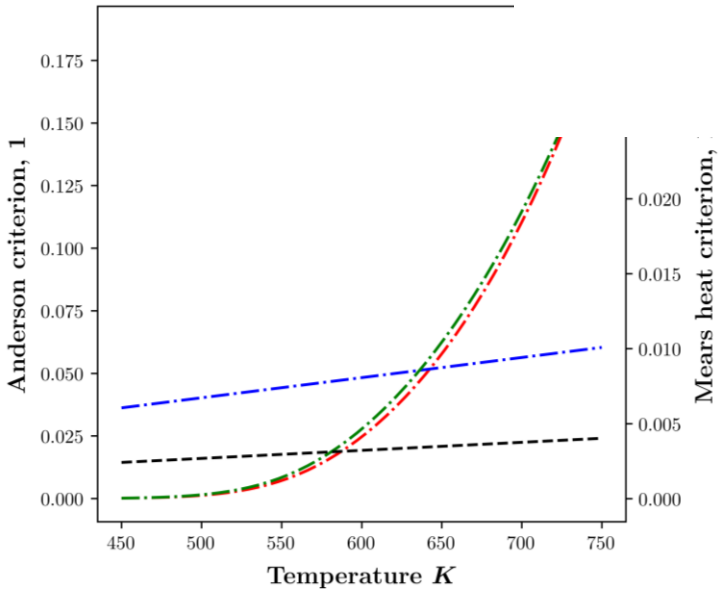

Figure B-2. Heat-transport resistances as function of the particle diameter.

References – Appendix

[1] M. Oh and C. C. Pantelides, "A modelling and simulation language for combined lumped and distributed parameter systems," *Comput. Chem. Eng.*, vol. 20, no. 6–7, pp. 611–633, Jun. 1996.

[2] L. M. Aparicio, "Transient isotopic studies and microkinetic modeling of methane reforming over nickel catalysts," *J. Catal.*, vol. 165, no. 2, pp. 262–274, 1997.

[3] F. Koschany, D. Schlereth, and O. Hinrichsen, "On the kinetics of the methanation of carbon dioxide on coprecipitated NiAl(O)<inf>x</inf>," *Appl. Catal. B Environ.*, vol. 181, pp. 504–516, 2016.

[4] E. Tsotsas and E. U. Schlünder, "On axial dispersion in packed beds with fluid flow," *Chem. Eng. Process. Process Intensif.*, vol. 24, no. 1, pp. 15–31, 1988.

[5] R. J. Kee, M. E. Coltrin, and P. Glarborg, "Molecular Transport," in *Chemically Reacting Flow*, Hoboken, NJ, USA: John Wiley & Sons, Inc., 2005, pp. 487–539.

[6] E. N. Fuller, P. D. Schettler, and J. C. Giddings, "A new method for prediction of binary gas-phase diffusion coefficients," *Ind. Eng. Chem.*, vol. 58, no. 5, pp. 18–27, May 1966.

[7] R. Bauer and E. U. Schlunder, "Effective radial thermal conductivity of packing in gas flow. Part I. convective transport coefficient," *Int. Chem. Eng.*, vol. 18, no. 2, pp. 181–188, 1978.

[8] R. Bauer and E. U. Schlunder, "Effective radial thermal-conductivity of packings in gas-flow. Part II. Thermal-conductivity of packing fraction without gas-flow," *Int. Chem. Eng.*, vol. 18, no. 2, pp. 189–204, 1978.

[9] E. Esche, "Optimal Operation of a Membrane Reactor Network," 2011.

[10] J. Bremer, K. H. G. Rätze, and K. Sundmacher, "CO 2 methanation: Optimal start-up control of a fixed-bed reactor for power-to-gas applications," *AIChE J.*, vol. 63, no. 1, pp. 23–31, Jan. 2017.

[11] N. Wakao and T. Funazkri, "Effect of fluid dispersion coefficients on particle-to-fluid mass transfer coefficients in packed beds," *Chem. Eng. Sci.*, vol. 33, no. 10, pp. 1375–1384, 1978.

[12] VDI, *VDI Heat Atlas*. Berlin, Heidelberg: Springer Berlin Heidelberg, 2010.